UNIVERSITY OF LIVERPOOL

An Experimental Study of Particle Sizing in Static Condition and in Shear Flow by Diffusing-wave Spectroscopy

Thesis submitted in accordance with the requirements of the University of Liverpool for the degree of Doctor in Philosophy

by

Huan Huang (BEng, MRes)

20 September 2012

Abstract

This thesis focuses on the micro/nanoparticle size measurement by using Diffusing-wave Spectroscopy, investigating the laser power and concentration effect on the measurement and researching the measuring method for particles in shear flow. A DWS-CCD backscattering experiment set-up was used in this project. By using this set-up, in all about 2000 experiments were performed during the project, including system testing, laser power influence study, concentration effect study and shear flow study.

In the beginning, a detailed analysis of the particle sizing for particles in static condition was carried out by summarising the principles and procedures. The results revealed that the experimental set-up in this work was reliable and repeatable. A calibration process was still required for the CCD's frame rate and resolution, the light absorption and the CCD's position in the set-up. After determining some important parameters, the research was extended to laser power and concentration influence study. The autocorrelation functions were produced under different laser power and for different concentration of particle solution. Analysis confirmed the influences, and the results were expressed in formulas to describe specific effects for laser power and solution concentration. Based on the formulas, new equations $R=\frac{16\gamma^2 n^2 \pi K_B T}{S^2\lambda^2\eta_0}\times\frac{(1-1.83\phi)}{(1+2.5\phi)}$ and $R=\frac{224\gamma^2 n^2 \pi K_B T}{S^2\lambda^2\eta_0}\times\frac{\phi^{0.531}}{(1+2.5\phi)}$ for particle sizing were derived for different concentration ranges. After that, particle's motion and light scattering in shear flow were investigated. It was concluded that three regions could be used to describe the particle's movement under shear force; in different regions, the autocorrelation functions were different due to the variation of the characteristic time scales. The Brownian motion and shear strain dominated particle's movement under specific flow velocities. Therefore, for particles subjected to high flow velocities, a new particle sizing formula $R=\left[\frac{3\gamma k_0\Gamma}{64\sqrt{5}S\rho_N\pi\langle 1-\cos\theta\rangle}\right]^{1/6}\times\left(\frac{\lambda}{\pi n}\right)^{2/3}\times\left(\frac{m^2+1}{m^2-1}\right)^{1/3}$ was produced to distinguish the general formula which was only valid for particles under Brownian motion.

Contributions made by this research are applying DWS application to micro/nanoparticle sizing in different conditions. In static condition, the laser power and concentration influence were described in formulas; new equations were produced for particle sizing for different

concentration range. In shear flow, the thresholds of Brownian motion domination and shear flow domination were found; a new particle sizing equation was derived for particles only controlled by shear force.

Acknowledgement

First of all, I would like to thank the University of Liverpool and the ORSAS committee for funding my PhD study in these years.

Second, I want to express my deep gratitude to my supervisor, Professor Doayi Chen and Dr Xiaoxian Zhang. They have offered me the opportunity to study here and gave me valuable guidelines and advice during the research. I am very lucky to have Dr Zhang as my supervisor in the final year who spent a lot of time on reading my thesis and gave me comments and suggestions.

I am also grateful to my colleagues and all of the staff in Civil Engineering, for their selfless help and support through my study in Liverpool.

I sincerely thank Mrs Denise Bain whom I always request help from. Most of the material I used in my experiment was ordered by her. I am also thankful to the technicians in School of Engineering, Mr Martin Jones, Mr Derek Neary and Mr Clive Whittam. They made some of the experimental apparatus and helped me on my laboratory work.

Finally, I would like to thank my parents, my husband and the other family members. They always encourage me to chasing my dream. I would not be able to finish this study without their love and support.

Publications

1, D. Y. Chen and H. Huang, Interaction of Flows and Particles at Sub-micrometer Scales, *Environmental Fluid Mechanics Memorial Volume in honour of Professor Gerhard H. Jirka* , Karlsruhe, Germany. June 2011.

2, H. Huang, D. Y. Chen and J. G. Chao, Effects of Laser Power and Suspension Concentrations on the Reliability of DWS Particle Sizing, *Review of Scientific Instruments*, 2012 (Under Review)

Contents

List of Figures

List of Tables

List of Abbreviations and Symbols

Abbreviations

CCD	Charge-coupled device
CHDF	capillary hydrodynamic fractionation
DLS	dynamic light scattering
DWS	diffusing-wave spectroscopy
EPSRC	Engineering and Physical Sciences Research Council
NTU	Nephelometric Turbidity Units
PIV	Particle image velocimetry
PMT	photomultiplier
PS	Polystyrene
TEM	transmission electron microscope
TiO_2	Titanium Dioxide

Symbols

Greek Letters

τ	Decay time	s
τ_0	The characteristic diffusion time	s
π	The ratio of a circle's circumference to its diameter	-
γ	Diffusion constant	-
θ	Scattering angel	Degree
σ	The total scattering cross-section	m^2
λ	Wavelength of light	m
β	The coherence factor	-
ϕ	Volume fraction	-
η_0	Viscosity of water	Pa **s**
η_s	Viscosity of the solution	Pa **s**
τ_B	The characteristic time scale representing Brownian motion	s
τ_S	The shear relaxation time	s
ρ	Fluid density	kg/m^3
μ	Dynamic viscosity of the fluid	kg/m **s**
ν	Speed of light	m/s
Γ	Shear rate	s^{-1}
ρ_N	Number density of particle	-

Latin Letters

a	Width of the cross-section of the flow cell	m
b	Depth of the cross-section of the sample cell	m
D_0	The diffusion coefficient of spherical particles	m^2/s
D_{eff}	The effective diffusion coefficient	m^2/s
d	Particle's diameter	m
E	The total scattered field	lm **s**
E_0	The scattered field received by the detector	lm **s**
$G_1(t)$	The electric field autocorrelation function	-
$G_2(t)$	The light intensity autocorrelation function	-
$g_1(t)$	The normalized electric field autocorrelation function	-
$g_2(t)$	The normalized intensity autocorrelation function	-
$H(q)$	The function to express the effect of the hydrodynamic interactions	-
I	The scattered light intensity	cd
I_P	The light intensity of *p*th pixel	cd
J_{out}	The flux of photon	lm
K_B	Boltzmann constant	J/K
k_0	The wave number	-
l	The scattering mean free path	m
l_a	The absorption length of the medium	m
l^*	The transport mean free path	m
L	Thickness of sample cell	mm
m	The ratio of the refractive index of the particle to that of the medium	-
n	The refractive index	-
P_e	Peclet number	-
$P(s)$	the distribution of photon path of length s	-
q	Wave factor	-
Q	The flow rate	ml/m
R	Particle radius	m
R_e	Reynolds number	-
r_i	Position of the *i*th particle	-
r_{in}	The light incident point on sample cell	-
r_{out}	The light escaping point from sample cell	-
$\left\langle \Delta r(\tau)^2 \right\rangle$	Particle's displacement	m

s	Photon's path length	m
S	The slope of autocorrelation function logarithm plotting against time square	-
$S(q)$	The static-structure factor	-
T	The absolute temperature	K
t	Time	s
U	energy density of light	lm **s**/m^3
V_{max}	The maximum velocity in the centre of the flow channel	m/s
$X(t)$	The average contribution of a scatter to the dephasing of a light path	-
z_0	The point photons start to propagate diffusively	-

Chapter 1
Introduction

1.1 Background

Nanotechnology is the scientific research which has been developed recently, however, it has been intensively involved in human's life nowadays. It is a rapidly evolving area with knowledge related to study the matters at the molecular level, and it is purposeful of controlling, manipulating or handling these particles at these very small scales[1].

A particle is a small subject that has a specific dimension in geometry and has uniform properties as a unit. Particles can be classified according to their sizes. Generally, particle with a diameter of 1-1000 micrometer are categorized as microparticle; 0.1-1 micrometer as sub-microparticle. If the diameter is in the range from 1 to 100 nanometer, the particle is grouped in the category of nanoparticle. This is one classification that has been accepted by most scientists and researchers[2-4].

Particles with diameter ranging from 1 nanometer to 1000 micrometer are frequently encountered in industries and in our domestic life. They could be in the forms of solid, solution, foam, aerosol, gel or colloid. They exist extensively in a wide range of materials, such as latex, polymer, ceramic, metal and carbon, and have important applications in biology, chemistry, physics and medicine. The particles in micro- and nano-scale have such a significant application in science and technology, and hence they have been widely regarded as one of the most important scientific discoveries of modern science.

Nanoparticle was found and called "ultrafine particles" in the beginning. In the1970s, the study of the concept "ultrafine particles" was conducted by Granqvist et al.[5] in US. This appeared to be the first thoroughly fundamental study of nanoparticle, extending our knowledge from micro-scale to nano-scale. The study is remarkable and considered as a pioneer work of nano-research. In addition to the research in US, a project named "ERATO"

was also performed in Japan from 1980 to 1986. It was a nanoparticle project reported by Hayashi et al.[6]. In the1990s, “ultrafine particles”, was replaced by the new name “nanoparticle”, and since then nanoparticle has been a widely accepted name by most researchers[7].

Compared to large particles, nanoparticles have significantly different features, dependent on their size. They are different from the bulk material which is made up of small objects[8]. They are an effective bridge between bulk material and molecular structures, and display various characteristics in optical, electrical, magnetic and thermal properties[9]. Most unique properties of micro/nanoparticle are due to their increased surface area and the altered surface structure, making them more active in certain circumstance. For example, the high surface-area-to-volume ratio of micro/nanoparticles leads to a high absorption and diffusion. Due to these features, Titanium Dioxide nanoparticle works as an effective photo-catalyst[10], and Zinc Dioxide performs excellently to block UV radiation[11]. Furthermore, these features provide advantages which are shown as stiffness, resistance and reinforcement for some material. For instance, ceramic made up of nanocomposites and nanocrystalline has high level of tenacity, and is corrosion-resistant; the mechanical properties have been dramatically enhanced[12].

Over the past 20 years, the research of micro/nanoparticles has made great progress, and a new technology, nanotechnology, has been developed.

Nanotechnology cross the boundaries and entails the knowledge of diverse science and technology, such as physics, molecular mechanics, chemistry, biology and so on[13, 14]. It manipulates matters in micro- or nano-scale dimension and researches the design, construction and application of material, device and system which is made up of micro/nanoparticles[15]. These material and device are mainly used in medicine, electronics, aerospace, environment, energy, biotechnology and agriculture. The widespread applications of this technology have been performed and evaluated, either in private and industrial fields. These applications offer better, cleaner, cheaper, faster and smarter products and production process for industries and humans[13]. Therefore, the nanotechnology research has a significant influence on the society.

Nanotechnology has a wide application in biology, medical science, physics, chemistry and engineering. For example, to avoid food spoiling or decaying in food packaging, one can add silicate nanoparticles to plastic film to prevent gasses (such as oxygen) or moisture entering the package[16]; and in coating industry, zinc oxide nanoparticles can be sprayed on cotton surface to block up UV irritation, for anti-bacteria purpose[17]; in textile industry, silver nanoparticles can be embedded in the fabric to kill bacteria to keep cloth fresh[18]. In biomedicine, protein carrying medicine can be coated with iron oxide nanoparticles, and these particles are then injected into blood vessel and travel with blood cells. When they reach the lesion position, the medicine is released directly and rapidly to the target. This can reduce the side effects of the medicine on patient's organs in blood circulation system (such as liver, kidney and spleen) and increase the bioavailability of drugs in comparison with other traditional delivery methods[19].

Nanotechnology has also been applied in environmental engineering to eliminate the toxic and hazardous substances in water and air[20]. For example, using titanium dioxide as a photo-catalyst is one of the most promising methods to deal with refractory organic contaminants in water and wastewater[21], in which titanium dioxide, in powder with nano-scale particles, is released to the contaminated water. When it absorbs UV radiation from sunlight or illuminated light source, the electron will be stimulated, creating the negative-electron and positive-hole pair that has strong oxidizability. Under oxidation, most organic pollutants and inorganic pollutants can be decomposed to water and carbon dioxide[22]. Since catalysts do not involve in the chemical and biochemical reactions, the nanoparticles are not consumed. Increased researches have proved that photo-catalysis works well with hydrocarbons, aromatic compounds, dyes, surfactants, pesticides, petroleum and cyanides, and during decolorization and detoxication, pollutants are mineralized to inorganic molecules[23, 24].

The key in photo-catalysis is to find appropriate ways to accommodate the particles in polluted water. Depending on the water to be treated, the particles can be either suspended in solution mixed with contaminants, or fixed on a solid substrate to create reactors. The simplest reactor widely used is batch reactor in which the mixed solution goes through quartz tube, irradiated directly by light source[25]. In the batch reactors, titanium dioxide is just a catalyst to maintain the photo-catalysed reaction and is not been consumed. Therefore an economic and environment friendly recycling process of the particles is necessary.

Commonly, they need post-treatment for recycle purpose, such as filtration, centrifugation and flocculation[26]. In these procedures, the particle size is a key element which influence and control the operation.

1.2 The Size of Micro/nanoparticle

Particle size is a key parameter of micro/nanoparticles that determines the particular properties of the bulk material. Tremendous research on particle dimension, size distribution and their dynamic properties in flowing water has been done in various fields, including food industry, chemical industry, pharmaceutical industry[27, 28]. For example, in producing drugs in solid or suspension forms, especially insoluble drugs, the particle size and size distribution could considerably influence the bioavailability of the medicine[29]. As a result, the measuring of particle size and size distribution is compulsory in medicine pulverization. Polymer synthesis, including emulsion and dispersion process, is also particle-size sensitive, especially when preparing polymer latexes[30]. In colloid chemistry, particles encounter weakly aggregation, therefore understanding the flow behaviour of particles is important[31].

In environmental engineering, the study of particle size is often required in the research of suspended solid sedimentation, turbidity measurement, contaminants degradation [32-34]. In coastal zone, the suspended matters are mixture of multiple particles, and they aggregate and break up under flocculation and erosion. The particle size is one index that reveals the dynamics of aggregation and sedimentation [35]. In research of photo-catalysis in recent 20 years, numerous issues have been addressed[20], including problems in fundamental study of photo-catalysis and photo-catalytic reactor, and in investigations of the characteristics and activities of catalyst particles in solution. For contaminants degradation, Tratnyek et al.[36] showed that particle size had effect on intrinsic activity of Fe^0 particles, thereby influenced the kinetics of contaminant degradation. When using TiO_2 as catalyst, Andronic et al.[37] found that the particle size changes due to crystallization of TiO_2.

The sizes of micro/nanoparticles and the associated size distribution can be determined by various techniques, such as dynamic light scattering(DLS), capillary hydrodynamic fractionation (CHDF) and transmission electron microscope(TEM)[30, 38, 39]. In the last twenty years, diffusing-wave spectroscopy (DWS) has been developed for measuring particles sizing in concentrated suspension[40]. DWS is an optical method which takes the

advantages of light to detect the dynamic properties. It measures the time autocorrelation of light signal which is multiply scattered in a turbid medium and then obtain the particle size information[41]. Apparently, most DWS studies have used a fixed light power to illuminate the solution and obtained the scattered light signal to measure the particle size in suspensions with various concentrations. The process of particle sizing is affected by different laser powers and solution concentrations. First suggested by Chiu and Zare[42], biased diffusion and optical trapping forces lead to power dependence of particle sizing process. Kuyper et al. agreed that and confirmed the dependence in their research[43]. Navabpour et al. have reported the influence of concentration on particle sizing analysis[44]. Schefflod also said that in the past his research has been restricted in sufficiently dilute solution in which particle's motion was predominate by Brownian motion. Actually at higher densities, the deviations of the measured correlation exist therefore the determination of particle size becomes more difficult[40]. Previous research proved that DWS is a reliable for multiple scattering systems when the system is sufficient dilute. However, the studies on the impact of laser power and particle concentration are rare.

Furthermore, due to the nature of DWS, most of the researches were carried out in stagnant mediums in which the particles only execute Brownian motion. Theoretical studies have showed the influence of Brownian motion and shear flow on the measured correlation functions, but experimental studies in dynamic systems, especially in laminar shear flow, which is more practical, is lack. In fact, one potential application of DWS in flow medium is for performing noninvasive measurement of the flow velocity. For example, Wu et al presented a technique using DWS in strongly multiple scattering medium for measuring velocity gradients for laminar shear flow[45]. Skipetrove et al. set up a model DWS experiment to study the particles in a flow of aqueous suspension which had similar parameters to some types of biological tissues; they believed that the technique had the potential for application in medical diagnostics, and their results had a extremely important impact on medical instrumentation[46].

Therefore, the research of laser power and concentration effects to the process of particle sizing and an experimental study of DWS in flow are necessary.

1.3 Research objectives

The objectives of this research are to study the measurement of micro/nanoparticle size in multiple scattering systems, to investigate the laser power influence on the process of particle sizing and research the measurement accuracy for concentrated suspension. This study aims to gain a visible insight of DWS methods to understand the light effect, suspension concentration effect. Considering my background is environmental engineering, apart from concentrated suspensions, particle sizing is also investigated in very low concentration suspension. This study will help other researchers to develop a new device based on turbidimeter which not only provides readings of solution turbidity and also provides the size values of suspended particles.

In addition, experimental studies are also expanded to particle sizing in laminar shear flow. This study aims to quantitatively develop the relationship between the measured correlation functions and the flow velocities, to investigate the interaction between particles under the influence of Brownian motion and shear flow. Under the effect of Brownian motion and/or shear flow, the autocorrelation functions have different decay modes which result in different particle sizing formulas. Therefore, by knowing the onset of effect, the knowledge of particles dynamic properties in flow medium will be obtained, and corresponding size measurement can be carried out.

Overall, the research aims to provide some theoretical support to the instrumentation of particle size analysis, to help technicians to develop the on-line or in situ equipment for flow velocity and particle's dynamic properties detection.

1.4 The Approach

In order to obtain a better understanding of DWS and achieve the above objectives, an experimental research has been carried out in the PhD study. A series of laboratory work have been completed in Littlewoods Laboratory, University of Liverpool. A large amount of data was collected from experiment, and then the data was properly saved. After that, the data was processed by programme, and seriously analyzed. Some reasonable results were generated from the analysis, and finally these results were reported in conference or presented in journal papers.

The approach is presented in details as following:

- In the beginning, literature reading was carried out to gain an insight of methodology of particle sizing by DLS and DWS.
- In order to obtain the direct impression of micro/nanoparticles, the particle observation was taken place under optical microscope.
- Preparing for the experimental, the high CCD system was rent from EPSRC instrument pool, and the latex beads suspensions were ordered from Sigma-Aldrich and Duke Scientific.
- A back scattering CCD-DWS experiment was set up in laboratory. An Argon Ion laser was employed as light source. A high speed CCD camera was applied to capture particle images. The particle suspensions were prepared, and the sample cells with observing windows were manufactured.
- The experiment set-up was verified and calibrated by standard latex particle solutions. The boundary conditions were defined, including resolution and frame rates of CCD camera, light absorption and CCD's position.
- In static status, the laser power tests and concentration tests were performed by setting various conditions (laser power outputs and volume fractions) according the research plan. Also, the experiments of particle sizing by DWS in very low concentration suspension were completed. Data was derived and collected. Processing and analysis were carried on in the same time with experiments.
- Experiments were performed in laminar shear flow. A large number of flow tests under different flow velocities in different sample cells were undertaken in the same experiment set-up. Data was continuously generated and collected from the lab. Properly processing was done, as well as analysis.
- The analysis was continued after the experiments. By assistant of some useful software, such as C++ programme, Matlab, Excel, Origin, the final results were produced and precisely presented in the form of table, graphs and texts. The results were presented in conference, and papers were submitted to journals.

1.5 Outline of the Thesis

This thesis includes eight chapters and the outline of each subsequent chapter is organized as follows:

- Chapter 1 is an introduction of the background of the project and literature review.

- Chapter 2 gives the description of particle sizing methods. It elaborates the principle of DLS and DWS and presents the history and development of these methods. It also demonstrates the methodology of DWS in experimental research.
- Chapter 3 describes the DWS experimental set-up and the arrangement in Littlewoods Laboratory, including the installation of optical device, the material preparation and the operation of equipments. In addition, it discusses the issues about the equipment selections and experimental geometries.
- Chapter 4 presents the process of DWS method verification. Particle size measurement is also described in this chapter. Furthermore, it talks about the boundary conditions determination and calibration, including the camera's frame rate and resolution, light absorption and the location of camera.
- Chapter 5 gives the summary of previous studies of laser power effect. Then it describes the laser power tests in this work. It reports the data analysis result of the tests. After that, discussion is made to present that the laser power may mislead particle sizing under a specific level. A conclusion is also given at the end of this chapter.
- Chapter 6 first summarizes previous work by other researchers, then gives the suspension concentration effect tests in this work. After the tests, results are presented to describe the influence in details. Also, two formulas are given for particle sizing under different concentration ranges. Apart from these, experiment has been performed on very low concentration suspension. In the final part, the same as Chapter 5, the experimental result discussion and conclusion are demonstrated.
- Chapter 7 is similar on structure to Chapter 5 and Chapter 6. It reports the experiment and results from flow tests which are conducted with flow fluid. The research studies the interaction between particles in flow and discusses the domination of Brownian motion or shear strain. The results are presented and a new formula is given for particle size measurement for particles controlled by shear force.
- Chapter 8 gives a summary of the thesis. It concludes that the present research work and discusses the issues existing in the current research. Additionally, the potential applications of the research results in environmental engineering are described. At the end, the future work which can be completed to optimize DWS is presented.

Chapter 2

Development of Particle Sizing Technology

2.1 Introduction

Measuring particle size is a great interest in many fields, including chemical industry, food industry, pharmaceutical industry, mining industry and environmental engineering. The particle sizing process is involved in any stage of the production. The properties of particles of particular materials are influenced by their shape, size, size distribution, surface area and stability[47, 48]. Hence, particle size is an important parameter indicating the quality of the material. For example, in pharmaceutical industry, the size of the particles of active ingredients is strictly managed to control the content uniformity[49], the dissolution rate[50] and the absorption rate of medicine[51]. In some procedures, such as milling and granulation that aim to reduce the particle size, the operation of size monitoring is required to obtain a desired particle size[52]. While, in crystallization, the particle size growth is also monitored during the process[53]. Measuring and controlling the particle size can help maintain the consistency of products, improve the quality of products, enhance the value of products and maximize the commercial profitability. Therefore, the measurement of particle size is a necessary procedure.

Particle size measurement is complex to determine particle's size range, size distribution and the mean average size. There are a number of choices to meet the needs in industry and research. For example, microscopic image analysis, laser diffraction, dynamic light scattering, acoustic spectroscopy, capillary hydrodynamic fractionation and so on. These methods have been well established[30, 54, 55], and some of them have been developed in commercial use[56, 57]. In this chapter, an overview of particle sizing method is presented to describe the historical development of the technology. In particular, dynamic light scattering (DLS) and diffusion wave spectroscopy (DWS) are presented in details to describe the progress of the photo correlation spectroscopy technique.

2.2 Particle Size Definition

Particle size is a parameter that describes the dimension of the particle; the particle can be solid, liquid or gaseous. The shape of the particle varies. For spherical particle, the size characterization is simple. If the particle is non-spherical, the description of particle dimension might need several parameters: its length, breadth, thickness and description of the overall shape[58]. Besides, an imaginary sphere can also be used, replacing the real particle to get an equivalent dimension[59]. The imaginary sphere can be a sphere having the same volume, weight or surface area with the given particle. Hence, the equivalent dimension of a particle could be either weight-based size, volume-based size or area-based size. For irregular particles, the characterization of particle size must include the equivalent diameter and particle shape. The commonly used particle diameters are the Feret's diameter, the Martin's diameter, the projected area diameter, the maximum horizontal intercept[60]. As shown in Figure 2.1.

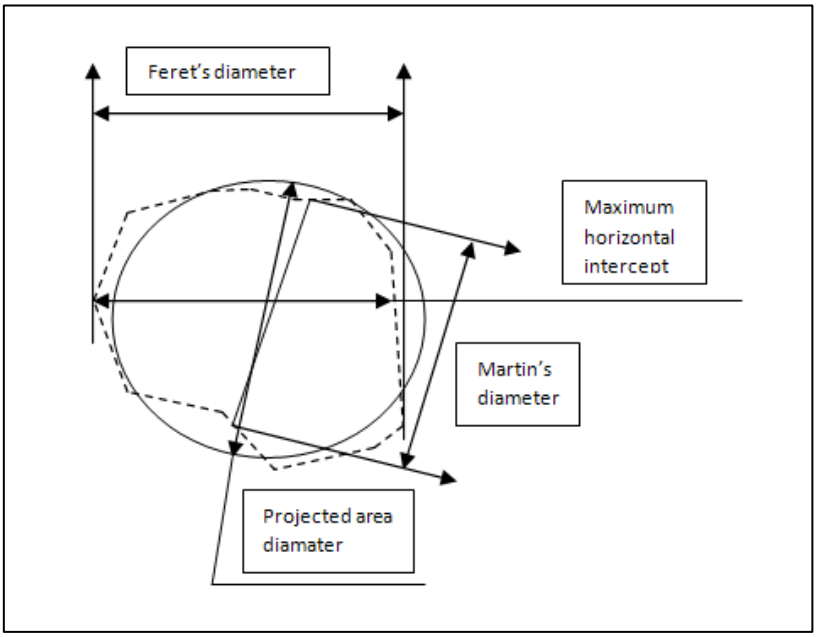

Figure 2.1 Statistical diameters used for irregular particle size characterization.

Walton has made a summary as following[61], the Feret's diameter is defined as the perpendicular distance between the pairs of parallel tangents that touch opposite sides of the profile; the Martin's diameter gives length of line which bisects the particle into two equal parts; the projected area diameter is the diameter of a circle with equivalent area as the particle's projected area. Ideally, the projected area diameter is regarded as a good

measurement of particle size; however, Feret's and Martin's diameter are more practical to conduct with the assistant of an eyepiece scale or filar micrometer. They are widely used, but an average value over all possible orientations should be give to minimize variation due to the random orientation[61]. Besides, the maximum horizontal intercept which means the largest length of the horizontal intercept of the particle profile also should be determined as an average value over the orientations[60]. In practical application, a combination of methods is required to provide more precise quantity of the size[58].

In fact, the diameter mentioned above is the average particle size for particles defined by particle sizing methods which are based on microscopy images. There are other methods which provide some different definition. For example, the volume equivalent particle size, the hydrodynamic particle size. The hydrodynamic particle size is often employed to describe the radius of a hypothetical hard sphere that has the same diffusion coefficient as the particle under examination; it is derived from the Stokes-Einstein equation by using light diffusing measurement[62]. It is easy to define the size of a single particle, but difficult for the ensemble of particles due to the diversity. Hence, the hydrodynamic particle size often is measured and employed to describe the mean average particle size which will be discussed in the following.

2.3 Particle Sizing Technology

When the particle size gets smaller into micrometer, determining its size becomes increasingly difficult. However, the problem has been sort out by the improved technology. A wide range of techniques are involved for accurately particle sizing research. Commonly, the optical microscopy, laser diffraction, digital image analysis and dynamic light scattering are used. When measuring the particle size, there is no method that suits all particle samples. The best way to obtain a good result is choosing a proper method according to the particle's properties.

Optical microscopy is the only method that provides direct observation of particles[63]. It can measure the particle size and shape simultaneously. It determines the Feret's diameter, the Martin's diameter, the projected area diameter or others. Hence, it is particular useful for measuring irregular particles. In this method, the particles under sufficient illumination are visibly observed, through the magnification, particle size information can be obtained by

reading the stage micrometer and the ocular micrometer. Or, particle's images are analyzed on the basis of coordinates, and the size is then estimated by counting the number of pixels[64]. This method is direct and simple for operation. However, it is an accurate way only if a representative enough number of particles are counted[30]. The minimum analysed particle number is the key point of this technique. According to Vigneau et al.[63], an average number of at least 1500 particles or more is suggested. Furthermore, the particles cannot be altered during the preparation of the mounting process. Therefore, the sample preparation is a job which needs time and patience. Besides, the resolution of the optical system highly controls the accuracy of the measurement[65]. All of these limit the extensive application of optical microscopy for size measurement. It is often regarded as a method just for calibration.

Laser diffraction is a well established technique for particle size measurement. It generates a volume equivalent particle diameter, and it is commonly used to measure size of particles (0.1-3000μm) in liquids, suspensions, emulsions and powders [66]. In this method, a particle is illuminated by a parallel light. With a lens placed in the light path between particle and detector, a diffraction pattern of rings which has diameter inversely proportional to the particle diameter is formed on the focal plane [67]. It can be seen in Figure 2.2 that large particle scatters light at small angles, and small particle scatters light at large angles. By analysing the radial intensity profile for the scattering pattern, the particle size can be obtained by using the Mie theory or Frauenhofer approximation[66]. Laser diffraction is a rapid and reproducible way to measure a broad particle size range. However, by using Mie theory, the optical parameters, such as refractive index, light absorption and imaginary component, must be known[68]. These parameters control the accuracy of the result. Whereas, the knowledge of light absorption is often estimated; it is not accurately obtained. Therefore, it may lead to incorrect result for samples with irregular particles or mixed particles.

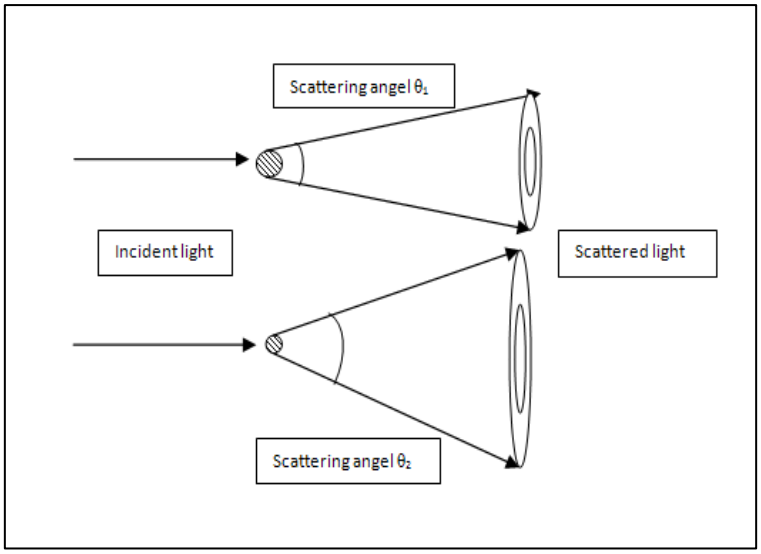

Figure 2.2 Diagrammatic description of light diffraction denoting that the particle size information is contained in the scattered light signal.

Particle image velocimetry (PIV) is a method based on the analysis of digital images of small seeding particles which is used to track flow[69]. In the beginning of the development, it was applied in velocity field measurement. Later, Chen et al.[70] used this digital image analysis method to study bubble size. In the work of Cheng et al.[71], it was developed to determine the geometrical properties of small particles. In their study, the particles suspension was illuminated by laser and strobe light to produce the light-scattering images and diffusive back-lighting images which were full of particle spots. These images were captured by high speed camera and processed by PC. In the picture, each particle spot occupied a particular projected area with a number of pixels. If the relationship between pixel and real length was known, then the particle size could be determined. Digital image analysis dose not withdraw particles from the media, no matter the sample is monodisperse or polydisperse; it is a solution with no intrusion. In addition, it can provide particle shape information, not only particle size. It is a simple and inexpensive method for particle dimension measurement [72]. Therefore, this method can be easily incorporated into basic aggregation modelling frame work[71]. It is always jointly used with laser diffraction to gain a deeper understanding of the particles.

Besides the techniques above, there are many particle sizing methods which are often used, for example, transmission electron microscopy, capillary hydrodynamic fractionation, differential sedimentation, dynamic light scattering and so on. In the paper published by

Elizalde et al.[30], it is concluded that if only the average particle size is sought with no importance of the whole particle distribution, DLS might be the best option.

2.4 Dynamic Light Scattering

2.4.1 Classic Dynamic Light Scattering

Dynamic light scattering (DLS, also known as photo correlation spectroscopy or quasi-elastic light scattering) is a powerful light scattering technique in micro- and nano-technology. It is a well-established spectroscopic method for studying single-particle (for dilute solutions) and collective particles dynamics in a variety of systems[73], such as solution, gel, foam and aerosol. It can measure the hydrodynamic particle size in a wide range. The technique is based on the fact that laser beam passes through solution or colloidal system can result in scattering of light by suspension particles. The scattered light fluctuating with a characteristic time scale provides valuable information about the size of the particles in this system[74].

In the classic DLS experiment (see Figure 2.3), a dilute particle solution is illuminated by a laser beam. Then, the laser light is scattered by the particles. At the side face, a detector is set to collect the scattered light from the solution. The principle of DLS was as following[75]: first, particles have a particular set of position in the scattering volume. The different position and the different distance between particle and the detector result in different scattered waves; second, the light source has different incident phases when they approach particles positions. Therefore, the relative phases of scattered wavelets are diverse. At time t, the detector receives a electric field of $E(t)$ that is the superposition of all scattered wavelets. When time elapses to τ, the new slightly shifted electric filed yield due to Brownian motion of the particles is updated to $E(t+\tau)$. Setting the autocorrelation function of the electric field $g_1(\tau)$, the normalized form of the intensity autocorrelation function $g_2(\tau)$ can be expressed in a relationship with $g_1(\tau)$. From the specific scattered light intensity autocorrelation function $g_2(\tau)$, a average particle diameter can be estimated[76]. In the work of Koppel[77], the particle size could be estimated by the cumulant method. This method was represented as that the first-order electric field autocorrelation function can be generalized to a sum or distribution of exponentials, and the distribution of the decay rate can be characterized by

calculation of its moments or cumulants. This method has statistical accuracy and can be incorporated with other data analysis.

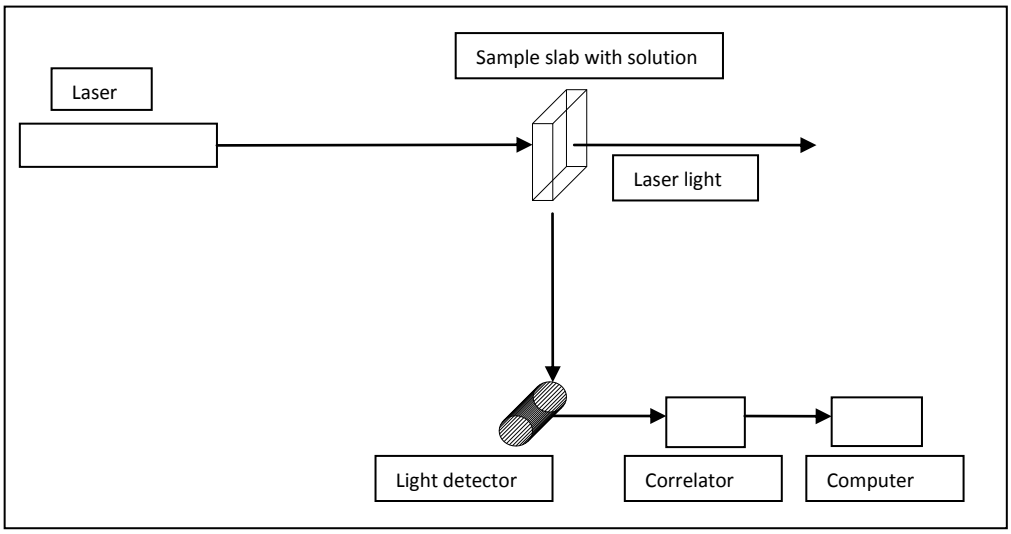

Figure 2.3 A classic DLS experiment setup

DLS works in static and monodisperse system which means the absence of multiple scatterings. In this system, each photon has been assumed to be scattered by particle exactly once before it is detected. Therefore, DLS cannot provide an insight into particle's dynamic properties in multiple scattering events. According to Zakharove et al.[78], in a high-order scattering system with a light transmission lower than 95%, a few things could be altered compared to low-order scattering system. First, the intensity autocorrelation function starts to decay quickly, which does not act as DLS theory. Second, due to the superposition of several scattering events, the scattering angel and wave number cannot be interpreted accurately. Therefore, DLS is limited in investigation of low particle concentration suspension, in which only single scatterings take place. For the multiple scattering medium existing in a variety of systems, in which particles produce strong scattered intensities, new technique has been developed based on DLS to meet the requirement of research and industry.

2.4.2 Improved Dynamic Light Scattering for Concentrated System

In order to solve the problem that DLS is unable to work in highly turbid system, the cross-correlation approach has been developed[79, 80]. This method has been validated by two simultaneous DLS experiments which are performed on the identical scattering volume to obtain the same cross-correlating signals, sharing the same scattering vector in different geometries and suppressing the multiple scattering [81]. The correlated intensity fluctuation

on both detectors is generated only by single scattered light, while the uncorrelated fluctuations produced by multiple scattered light only contribute to the background[81]. The improved method has been proved to be successful and it has been reported in more versatile ways in the published papers presenting two-colour DLS and three-dimensional DLS[81, 82].

In the dual-colour cross-correlation experiment of Schatzel et al.[83], two colour coded beams were used, and two of the possible four paths were selected. In their design, the identical scattering volume and scattering vector were chosen for both colour. The light fluctuation was isolated due to a large range of scattering angles. The isolation played an important role in extracting static structure data. While, different from two-colour DLS in which the incident and scattered beams all lie in the same plane, in three-dimensional DLS, two incident beams with the same colour are slightly above and slightly below the scattering plane, and the detectors are correspondingly placed above and below the plane[84]. In the special geometry, the incident beam, which enters the sample above the plane, and the scattered beam, which is below the plane, build up a light path, defining the same scattering vector. Another path is generated similarly but inversely. Figure 2.4 shows the scattering geometries for normal single beam light scattering, dual-colour DLS and three-dimensional DLS, respectively. k_1 and k_{12} represent the incident light propagation vector. k_2 and k_{22} represent the scattered light propagation vector. θ indicates the scattering angle, and q means the scattering vector with $q = k_2 - k_1$.

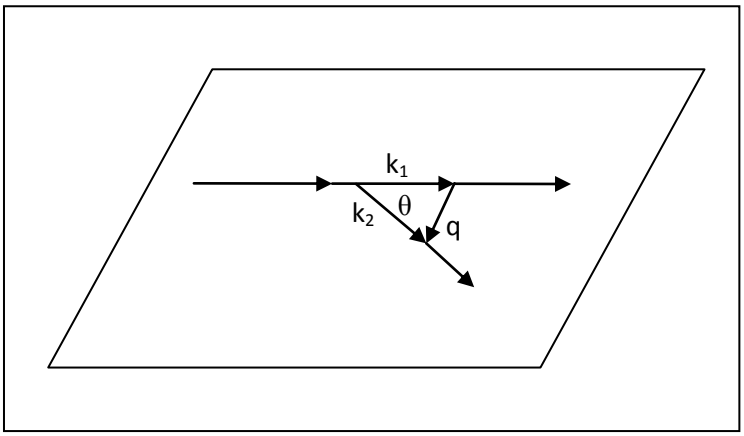

(a)

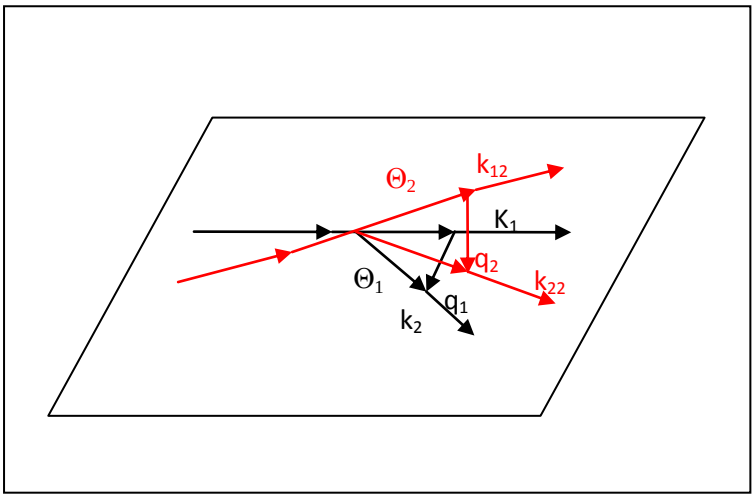

(b)

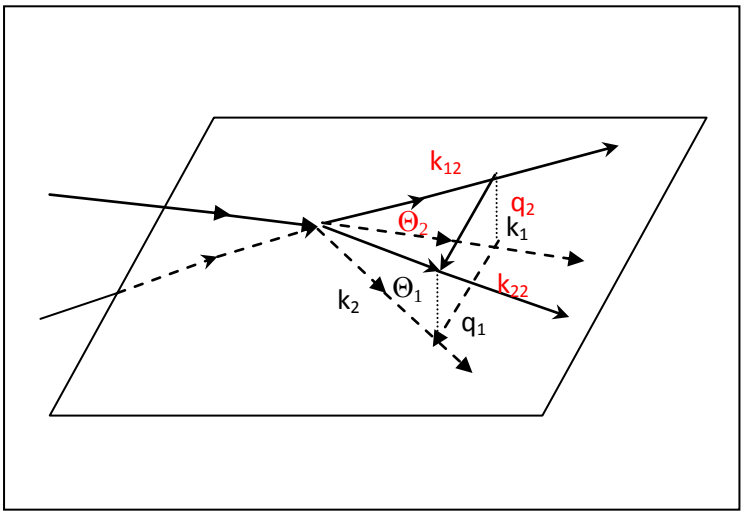

(c)

Figure 2.4 The scattering geometries for normal one-beam light scattering (a), two-colour DLS (b) and three-dimensional DLS (c).

The cross-correlation method is an improvement of dynamic light scattering to overcome the shortage of normal DLS that it cannot be applied in turbid system. The cross-correlation method is robust, repeatable and feasible, but still has a few disadvantages, and one of them is difficulty in setting up of device and geometry. Also, the detectors should start to record light signal simultaneously when the system is operated, otherwise the correlated intensity fluctuation will not be correctly related. Apparently, the cross-correlation method is not convenient for routine application. As a result, another optical technique, diffusion-wave spectroscopy, was developed.

2.5 Diffusing-wave Spectroscopy

2.5.1 Derivation of Diffusing-wave Spectroscopy

Dynamic light scattering requires the scattering particles to be maintained at a low concentration to ensure that light photons are only scattered once when they pass through the sample. However, for complex fluids in both research and industry, this might not be the case. To overcome such shortage of DLS, diffusing-wave spectroscopy (DWS) is developed to apply the light scattering technique to strongly scattered medium in which the light photon is scattered several times before it is collected by the detector.

DWS was developed in the late 1980s [85, 86]. Its principle is similar to the conventional DLS, both using light signal detector to collect light intensity data and temporal fluctuation of the single speckle spot of the scattered light; both of their temporal autocorrelation functions reflect the dynamics of the scattering medium, therefore characterizing the particles properties[87]. However, DWS is not equal to traditional DLS. DWS is more powerful because it enhances the analytic ability of DLS to concentrated suspension without dilute or index-match; it can provide information about the local dynamic particle dispersion without any restrictions on particle's concentration and the solution's turbidity due to the unique assumption that the propagation of light through a highly scattering medium is considered as a diffusing process[87].

2.5.2 Principle of DWS

2.5.2.1 Two Assumptions in DWS theory

Before presenting the theory of DWS, two fundamental assumptions are given first. According to the description of Weitz. et al.[87], in conventional DLS, the information about

the dynamic properties of medium can be reflected from correlation function which is characteristic by decay time. The decay time is related to a length scale of particle's motion. On this length scale, the path length of the scattered light has changed by one wavelength. Then, this change leads to a 2π phase shift of the detected light and an alternation of light intensity. To obtain the dynamic information from the characteristic decay time, the knowledge of length scale which is defined as the inverse of wave vector $q^{-1}$is required. In dilute medium, the wave vector is easy to know, but in multiple scattering it is unknown because the particle is scattered more than once. Hence, DLS is strictly limited for the application in turbid system. However, DWS entails two fundamental approximations, and based on the fundamental approximations, DWS can resolve the problem, and it can be applied in regimes with a large number of scatterings.

Weitz et al. [87] has represented the two statistical assumptions as following. First, light is assumed to propagate the medium with photons executing random walk after numerous scattering events. Any interference effect is ignored during light transportation through the medium because the scattering light is not strong enough to approach the localization of light. With these random scattering, light intensity diffuses. Due to this propagating assumption, the path distribution function taken by photons can be calculated with statistical approximation. Second, because of the large number of scatterings, the individual behaviour of photon is not important any more. In turn, the scattering events are approximated as a contribution of an average scattering. Based on the average scattering event assumption combined with diffusion approximation, the number of scattering event contributing to each path length can be determined. In this way, DWS is invalidated by the approach of the calculation of correlation function.

2.5.2.2 DWS Theory

The theory was given in details by Maret G.[85], Pine et al.[88], Stephen [89], Weitz et al.[87]. Light propagation is assumed in DWS which means that photons take different paths during their diffusion process. When photons are traversing the medium, there is a possibility for each given path that photon follows. Each path has a long distance involving numbers of scattering events before photons escape from the medium. Each scattering event is approximated by a single average scattering. Therefore, the contribution of individual path to the correlation function can be expressed as sum of the average scatterings. This step is

simplified from the summation of all individual scatterings. During the process in which total path length changes by one wavelength, each path has an individual contributing length that can be defined as decay rate. The contribution of different paths with various lengths decays at different rates. As such, the electric field autocorrelation function can be written as[88]

$$G_1(\tau) = \int_0^\infty P(s)\exp\left[-(2\tau/\tau_0)(s/l^*)\right]ds \tag{2.1}$$

where τ is the decay time which describe the autocorrelation function decays with the time constant, $P(s)$ is the distribution of photon path of length s in the sample. τ_0 is defined as characteristic diffusion time as

$$\tau_0 = 1/D_0 k_0^2 \tag{2.2}$$

where D_0 is defined as the diffusion coefficient of spherical particles; $k_0 = 2\pi n/\lambda$, n is the refractive index and λ is the wavelength of light in the medium. In fact, in DWS, there are two different diffusions. One is the diffusion of the scatters, and the other is the diffusion of the photons. Different to D_0, the diffusion coefficient for photons during light propagation is D_1 which is defined as

$$D_1 = vl^*/3 \tag{2.3}$$

where v is the speed of light in the medium and l^* is the transport mean free path in the medium. The transport mean free path l^*, characterizing the scattering medium, is the length that a photon must travel before its direction is completely randomized. Corresponding to l^*, l is defined as the scattering mean free path, the length that a photon must travel before it is scattered a single time. It is given

$$l = \frac{1}{\rho_N \sigma} \tag{2.4}$$

and

$$l^* = \frac{l}{\langle 1-\cos\theta \rangle} \tag{2.5}$$

where ρ_N is the number density of particle, σ is the total scattering cross-section, θ is the scattering angel, $\langle\ \rangle$ indicates an ensemble average over many scattering events. Since photon will be scattered many time before it executes random walk, the transport mean free path is always larger than the scattering mean free path, that is $l^* > l$. Equation (2.1) represents the fact that a diffusion path of length s consists of s/l^* steps of random walk, and

for each step, $G_1(\tau)$ decays in $\exp(-2\tau/\tau_0)$ on average. Hence $G_1(\tau)$ contains a wide distribution of decay time that depends on the number of scattering events. Therefore, a long path decays fast with a short decay time, vice versa.

The key point to calculate $G_1(\tau)$ is to work out the path length distribution $P(s)$. To work out $G_1(\tau)$, the following procedures are considered. In a typical optical arrangement for DWS (see Figure 2.5), a light source is incident over an area of the sample slab with the thickness of L filled of particle suspension. Photons entering the sample cell at the point r_{in} encounter the particle, then light is scattered. After numerous scattering, photons execute a random walk until they escape from the sample slab at point r_{out}. They run away from the medium, and they are collected by the detector. In this process, the light is delayed between the initial pulse and the finally detection. Before all of the photons left the sample, the light intensity experiences a maximum value and then drop down to zero at the end.

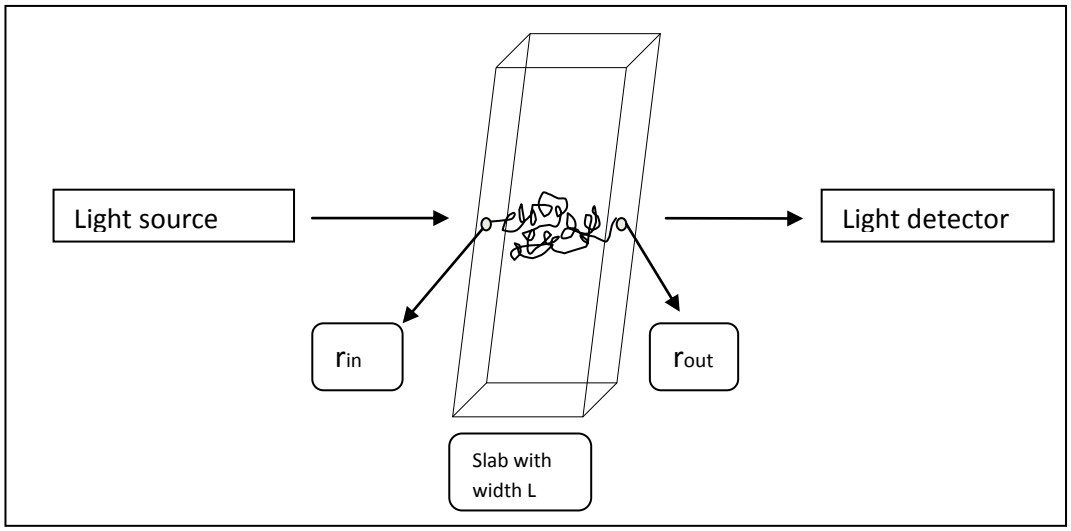

Figure 2.5 Photon enters the sample slab and executes random walk until leaving the slab.

The length distribution $P(s)$ related to the photons that travel a distance $s = vt$ is proportional to the flux of photons $J_{out}(r_{out}, t)$ that reach at the point r_{out}. That is[87]

$$P(s) \propto \left| J_{out}(r,t) \right|_{out} = \frac{vU}{2} \Big|_{r_{out}} \tag{2.6}$$

where U is the energy density of light, i.e., number of photons per unit volume. Furthermore, Weitz et al. has observed that $G_1(\tau)$ is a Laplace transform of $P(s)$, thus the solution is simplified as follows[87]

$$G_1(\tau) = \frac{\overline{U}(r,\tau)\big|_{r_{out}}}{\overline{U}(r,0)\big|_{r_{out}}} \tag{2.7}$$

where $\overline{U}$ is the Laplace transform of the energy density of light. It can be found that when $\tau = 0$, $G_1(\tau) = 1$.

2.5.3 The Autocorrelation Function in Two Different Geometries

Using the diffusion assumption to describe the light propagation in strongly scattered medium largely simplifies the analysis of DWS measurement. Photons are scattered for multiple times, and then undergo a large number of intermediate scattering events. As a result, the scattering vector is not as much relevant to correlation function as that in DLS. Consequently, the importance of the scattering angle between incident and detected light in DLS has been reduced for DWS. Therefore, the experimental geometry for DWS can be diversified with various scattering angels. Besides the basic experimental geometry, transmission, the backscattering geometry has been developed by researchers [85, 88, 90].

Transmission experiment geometry is an experiment set-up in which the light source is incident into sample slab from an extended plane source, and then it is detected from the opposite side of the sample slab. Photons traverse the suspension and experience multiple scatterings during this process. Pine et al. have expressed the electric field autocorrelation function in transmission as[88]

$$G_1(\tau) = \frac{L}{\gamma l^*} \frac{\sinh\left[\gamma\left(6\tau/\tau_0\right)^{1/2}\right]}{\sinh\left[\left(L/l^*\right)\left(6\tau/\tau_0\right)^{1/2}\right]} \tag{2.8}$$

where γ is the diffusion constant, L is the thickness of sample cell. When the decay time is much smaller than the characteristic diffusion time, that is $\tau \ll \tau_0$, Equation (2.8) can be re-written to[88]

$$G_1(\tau) \approx \frac{\left(L/l^*\right)\left(6\tau/\tau_0\right)^{1/2}}{\sinh\left[\left(L/l^*\right)\left(6\tau/\tau_0\right)^{1/2}\right]} \tag{2.9}$$

Backscattering is another commonly used geometry. In this geometry, the laser beam enters from one face of the sample. After the photons are fully scattered, the light intensity signal is collected by the detector that is placed at the same side of the incident light, but with an angel formed between the incident light and detected light. The electric field autocorrelation function collected at any points in the same side can be expressed as[88]

$$G_1(\tau) = \frac{1}{1-\gamma l^*/L} \frac{\sinh\left[\left(L/l^*\right)\left(6\tau/\tau_0\right)^{1/2}\left(1-\gamma l^*/L\right)\right]}{\sinh\left[\left(L/l^*\right)\left(6\tau/\tau_0\right)^{1/2}\right]} \tag{2.10}$$

2.6 Summary

The particle's dimension can be characterized using Feret's diameter, Martin's diameter, the projected area diameter, the maximum horizontal intercept, the perimeter diameter or other equivalent diameters dependent on the application of the particle. Dynamic light scattering is a well established method used commercially. It is able to measure the mean particle size (hydrodynamic particle size) and particle size distribution. The principle of DLS is to detect the light that, when going through a medium, will fluctuate with a characteristic time scale. The characteristic decay time provides valuable information about the dynamic medium, including particle size. Therefore, particle size can be derived from the measured correlation function. However, DLS is not robust enough to research the highly scattering medium due to the unknown scattering vector. It is limited in strictly single scattering system with a low particle concentration.

Based on classic DLS, several improved methods have been developed. In addition to two-colour DLS and three-dimensional DLS, diffusing-wave spectroscopy (DWS) is also developed for multiple scattering systems, even opaque solutions with very high particle concentration. DWS assumes that the photons movement is a diffusion process. When light traverse the medium, it propagates from the entering points. After the propagation, it is then detected by a signal detector. In this process, photons are scattered numerous times before they execute a random walk. As a result of multiple scattering, the importance of scattering vector is not as much relevant to correlation function as that in DLS. Therefore, the transmission and backscattering experimental geometries are both developed in DWS measurement.

Chapter 3

Experimental Set-up and Arrangement

3.1 Introduction

A variety of methods are available to measure the dimension of an individual particle and the average size of collective particles [30, 55]. Depending on the techniques, different experimental methods have been developed for particle size measurement. DWS is a method developed from conventional DLS, therefore, their set-up and arrangement are similar. They are same in that a small sample slab filled with particle suspension is illuminated by a laser beam. The light photons are fully scattered in the sample medium, and then the intensity of the signal is collected by a detector. After that, the light signal is processed and displayed visually. Finally, the data is recorded by a computer and processed by program. Essentially, the system consists of a particle sample, a laser beam, a detector, a processor and a computer. It can be grouped in optical system and sample cell system. However, in order to meet specific requirements in applications, the set-up could vary in experimental geometry, equipment selection, and apparatus arrangement.

For traditional DWS, two different geometries (transmission and backscattering) can be used to increase its flexibility and practicality. Besides the geometries, choosing a proper device in DWS measurement is also important, especially the light signal detector. The Photomultiplier (PMT) tube was commonly used due to its high sensitivity, but the Charge-couple Device (CCD) camera has been becoming increasingly popular because of its ability to monitor a large number of speckles. The multi-speckle approach makes that the light signal's ensemble average can be achieved, hence the data processing time can be reduced substantially.

Since the objective of this research is to study particles in complex fluid in various conditions, a CCD DWS backscattering experiment was set-up.

3.2 Overview of DWS Experimental Set-up

DWS is an improved method of DLS, which extended the ability of light scattering method to highly scattering system. As such DWS shares a number of features of the conventional DLS, particularly in the arrangement of optical system and the way of light signal data collection. However, there are some differences between the two methods. Figure 3.1(a) shows the basic experimental set-up of the classic DLS, in which a laser beam is incident into a small volume particle solution. Then, the light photons diffuse with several random walks till they escape from the solution and exit from the sample around the slab. The detector is applied to receive the photons, and to measure the fluctuation of light intensity. After the light fluctuation is processed by digital correlator, the data is ultimately output to a PC to be analysed. Figure 3.1(b) shows a typical DWS experimental set-up with transmission geometry. A coherent laser light is incident on the left face of a sample cell filled with particle solution. When the laser beam travels through the sample, photons are scattered by particles and then move along random paths in the solution. After a large number of scatterings, the photons escape from the suspension and are then collected by the detector located on the opposite side of the laser source. The optical waves received from different light paths reflect the fluctuation of light intensity. The intensity fluctuation is processed by a digital correlator to produce the autocorrelation function which is then exported to a computer.

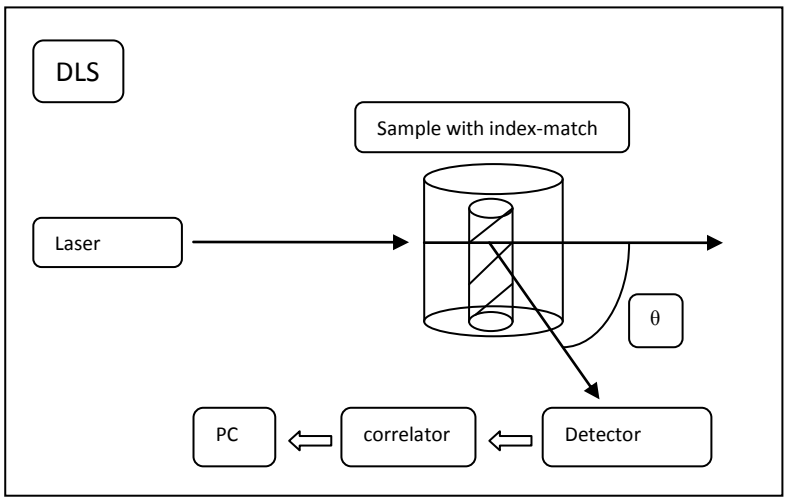

(a)

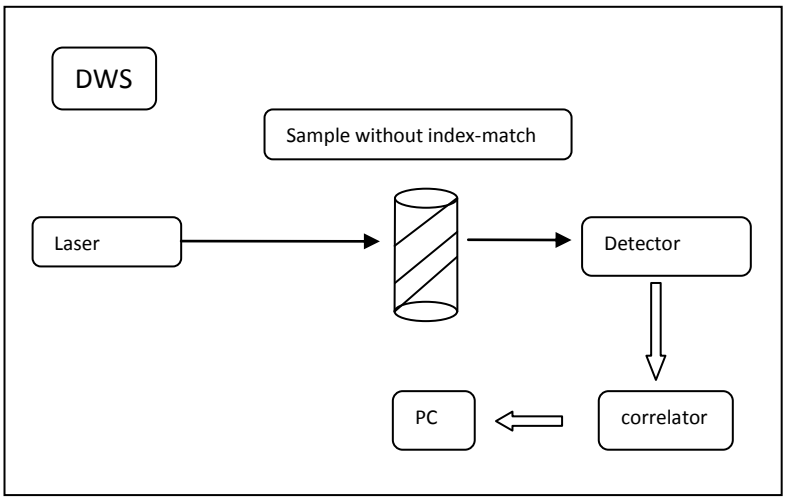

(b)

Figure 3.1 The diagram of Experimental set-up and arrangement for DLS (a) and DWS (b).

It can be seen from the above that DWS set-up is different from DLS. The main differences are that DLS requires index-match which is matching the refractive index of both particle and solution to improve the optical object detection[91]; the light intensity fluctuation is sensitive to the angle of detector away from the axis, θ, as shown in Figure 3.1.

The basic DWS can be enhanced by adding apparatus. For example, Scheffold[40] developed a device as shown in Figure 3.2, which works for both geometries. Hence the light can be detected in both transmission and backscattering. A water reservoir is used to control temperature; in the mean time, it also works as an index matching solution for the sample cell mounted inside. Two polarizers are applied, one with λ/2 retardation plate aiming to retain a continuous variation of the incident light intensity from the laser, and the other working in backscattering allowing the detection of polarized or depolarized lights. The beam-expander controls the width of the laser beam, making it significantly larger than the thickness of the sample.

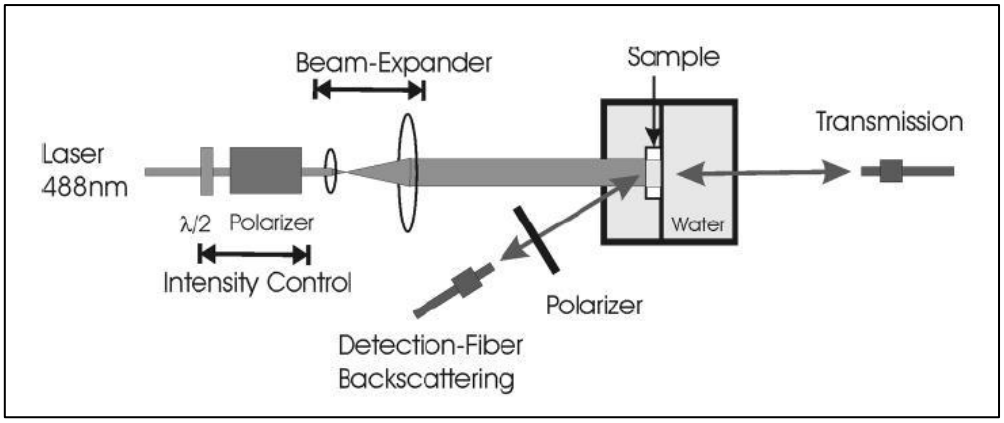

Figure 3.2 Diffusing-wave spectroscopy set-up which works for both transmission and back-scattering geometries[40].

Apart from polarizer, optical fibres can also be used in DWS. Keuren et al.[92] used the single-mode fibre for concentrated latex dispersion. The single-mode optical fibre is an optical fibre which only carries a single ray of light or a single mode of light. It was used to reduce the effect of autocorrelation function of multiple scattered lights from concentrated dispersions. Similar set-up is used in the experiment of Rojas-Ochoa et al.[93] which investigated the small-angel neutron scattering from concentrated colloidal suspension using a single mode fibre.

3.3 Transmission and Backscattering Geometries

The wave vector is important in conventional DLS. Adjusting the angel between the incident and the detected light can modify the value of the wave vector. In contrast, the angel of the detector in DWS is not critical due to the diffusion assumption. The light experiences a large number of scattering, and leaves the sample with identical intensity in all the directions[87]. Therefore, the experimental geometry is grouped in transmission and backscattering as shown in Figure 3.3.

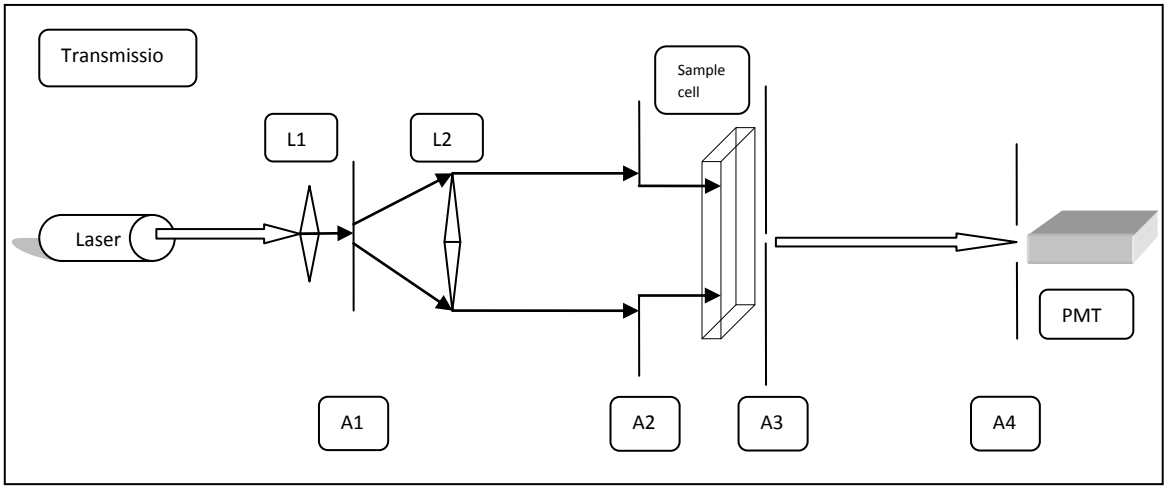

(a)

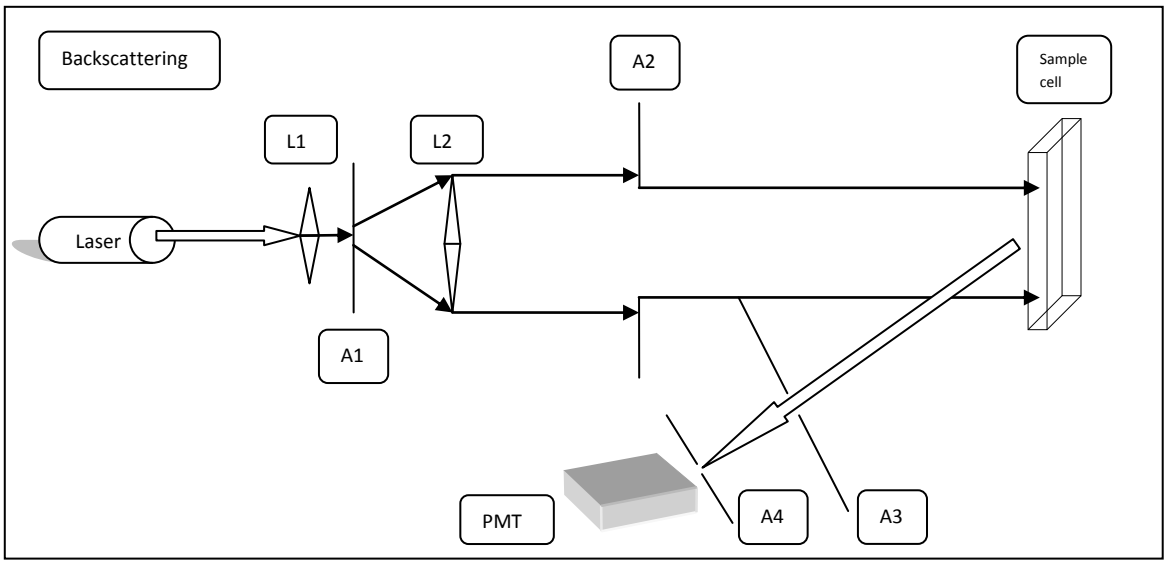

(b)

Figure 3.3 The schematic representation for DWS experimental set-up, transmission geometry(a) and backscattering geometry(b).

In transmission geometry, the laser beam is expanded by lens L1, and is then collimated by lens L2. After laser penetrates the sample cell S, a speckle is detected by a photomultiplier (PMT). Weitz et al.[87] showed that the aperture A1 works as a spatial filter, and A2 selects the central part of the laser beam which has a constant intensity. To avoid multiple speckles being detected, apertures A3 and A4 are placed between the sample cell and PMT. Finally, the light intensity received by PMT is output to a digital correlator. The backscattering is similar to the transmission. Apertures A1, A2, A3 and A4 have identical functions as those in the transmission. The only difference is the location of the detector which is located on the same side of the light source in backscattering.

In transmission DWS, the incident and detected lights are on opposite side. Therefore, all of the path lengths are longer than the transport mean free path l^*. This geometry complies with the light propagation assumption well. In backscattering, light is incident and detected on the same side of the sample. As a result, the diffusion approximation should be carefully used because a large number of length scales are comparable with l^*. However, backscattering has a number of advantages[87]. First, it is more convenient because it only needs access to the sample from only one side. As such, this geometry is widely used in on-line monitoring where the space is limited. Furthermore, transmission requires to know the transport mean free path l^* when interpreting the autocorrelation function, but this independent knowledge is not necessary to be obtained in the backscattering. Additionally, the autocorrelation function decays faster in transmission geometry. Wu et al.[45] argued that what cause this in transmission is due to that only long path that decays rapidly contributes to the autocorrelation function, and, in contract, short paths that decay slowly contributes to the autocorrelation function in backscattering. Because the longer and faster decay optical light paths are more attenuated by light absorption[94], the autocorrelation function of transmission will be more affected compared to that of backscattering geometry.

As light leaves the sample with a uniform intensity in all the directions, the angel between the incident light and detected light is not critical to DWS. However, the experimental geometry is important due to different path lengths obtained in the transmission and the backscattering. Hereby, both of the thickness of the sample and the spot size of the laser beam will influence the autocorrelation function. The thickness of the sample affects the distribution of path length and the light speckle on the sample face influences the decay time of the autocorrelation function. Kaplan et al. concluded that DWS worked best for sample cell with $L/l^* > 10$[95]. In the transmission, either point light source or expanded plane light source can be used, whereas in backscattering only expanded laser beam is suggested to illuminate the area of the incident face which is much wider than l^* [87].

3.4 PMT and CCD

Photomultiplier (PMT) is a high sensitive detector which works in a wide range of electrical spectrum including visible, ultraviolet and near-infrared light. It multiplies the light signal by the process of electron emission. Even the intensity flux is very small; the light signal can

also be collected. Figure 3.4 shows the image of the PMT which was used in our DWS research.

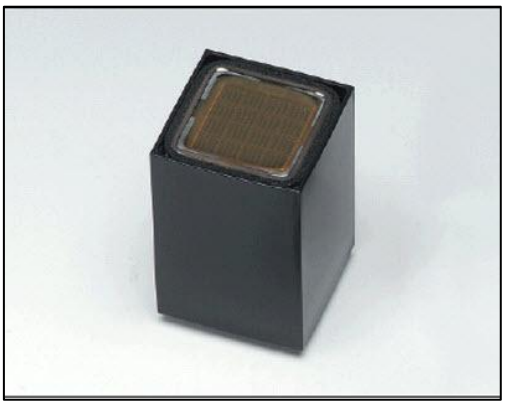

Figure 3.4 H8711 multianode photomultiplier tube made by Hamamatsu[96].

In conventional DWS, the scattered photons are detected with a photomultiplier tube at a fixed scattering angel to measure the intensity autocorrelation function. Then this light signal is fed to an electronic correlator to calculate the correlation function. In order to obtain accurate results, the correlator output result is accumulated and then averaged over time. The process of accumulating and averaging are sophisticated and time-consuming, especially for very slow dynamic systems, such as colloidal glasses, polymeric and colloidal gels[97]. As Wong et al.[98] pointed out, in order to achieve a good accuracy, the averaging time should typically 1 to 10000 times longer than the characteristic time scale in the interest; as such, hours to days should be taken to have an adequate time average in calculating the autocorrelation function if the interested time scale is in the order of several to tens of seconds. Although PMT has high sensitivity to light even at low intensity flux, it is not an efficient approach to collect sufficient amount of intensity fluctuations to obtain the autocorrelation function. As a result, a new approach which only needs a short measurement time was derived, replacing the photomultiplier with a CCD camera.

Charge-coupled device (CCD) is a chip sensor for light signal detection. It is extensively used in professional photography, medical and physical applications. CCD is a light-sensitive-integrated circuit, capturing and storing the electrical charge, and converting the charge into digital values. It improves the resolution of pictures compared the old technologies. Figure 3.5 shows the CCD system which was used in our DWS experiment.

Figure 3.5 Fastcam Ultima APX CCD system made by Photron[99].

Replacing PMT with CCD camera is to develop a more direct and efficient approach for DWS measurement. When CCD camera works as a detector, the CCD chip acts as a number of arrays of PMT, all of which are positioned at nearly identical scattering vectors[100]. It collects light signal from a variety of speckles, and a set of multiple DWS measurements is then carried out simultaneously. For each set of data, the correlation functions measured on different pixels with the same scattering vector are processed and assembled. The time averaging of each pixel in the individual measurement is performed to determine the intensity autocorrelation. Apart from time-averaging, ensemble average is also calculated for an autocorrelation function. This new approach has been proved to reduce sampling times and to achieve high statistical accuracy. Cipelletti et al.[97] showed that since the assemblage was performed on different speckles with no dependence, the averaging conducted on pixels enhanced the statistical accuracy; in the mean time, the duration of experiment could be reduced by a factor equal to the number of coherent sampled areas. Because CCD camera significantly improves the experimental efficiency, this method is suitable for real time measurement, particularly for systems which have a long-time behaviour in which the motion of the scattering particle is hindered by elastic forces, such as polymer gels, glassy colloidal systems[101].

3.5 Experimental Set-up in the Project

The DWS experimental research in this work was carried out in Little Woods Laboratory located on the ground floor of Hartley Building, University of Liverpool. This laboratory is one of the laboratories in Medical Laser Institute which was found in 2000. It has a spacious area, and has a quite environment that is suitable to use laser to do research. The research

started from February 2009 and finished on September 2011. About 2000 experiments were run during this period, including experimental set-up calibration, boundary conditions determination, particle sizing, laser power testing, concentration tests and flow tests. A huge amount of data was collected from the operation, then processed and analysed after experiments. Based on the efficient data collection and statistical analysis, an insightful understanding of DWS for measurement of micro/nanoparticle size under various conditions was obtained.

Figure 3.6 shows the DWS set-up installed for this study. A coherent laser radiation was generated by an Argon Ion laser at wavelength of λ=488nm with power up to 2W. The laser beam was expanded to a required width and focused on the sample slab with a spot in a diameter of approximately 1.5mm. After fully scattering, the backscattering light was directly detected by a high speed CCD camera. Light intensity fluctuation was recorded in the form of pictures in the digital processor. Finally, the data was exported to a PC for calculating the ensemble average as multiple speckle data was collected.

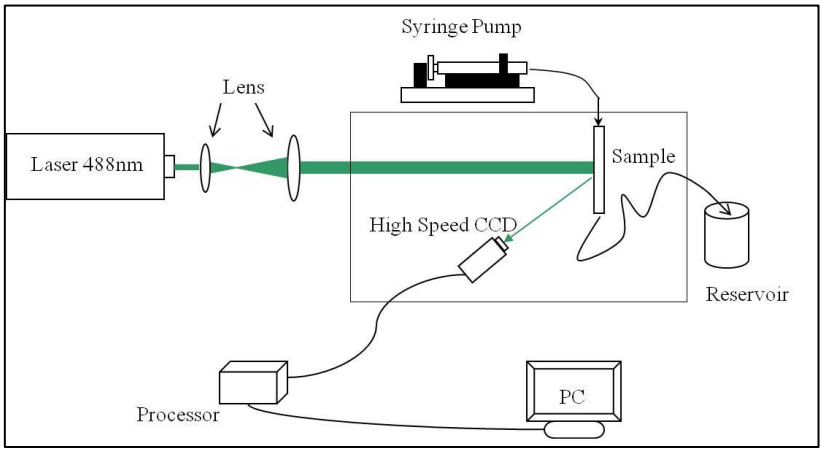

Figure 3.6 The DWS experimental set-up in this project.

3.5.1 Optical System

The coherent laser beam used in the DWS measurement is generated by an Argon Ion laser. The laser model is Spectra-Physics Stabilite 2017 which is manufactured by Newport. This laser uses the ionized Argon gas as its lasing medium which means that the energy level transitions contributing to the laser action come from the Argon ions. Because of this, the laser machine produces a continuous laser beam at two wavelength ranges, 333.6-363.8nm and 457.9-514.5nm, both of which are visible light. This type of laser is primarily applied for

particle image velocimetry (PIV) on transparent models, and in other tests which require a coherent light source. It has a switched-resistor power supply and a low-thermal gradient resontaor for rapid warm-up and stable operation. For each wavelength, the intracavity aperture can be easily adjusted for optimizing the mode control. Due to the large energy required for stimulation of ionic transition, this type of laser always has a water-cooling system to take away the heat produced by large current. Therefore, the system needs a large space and appropriate water supply. Since the tap water flow in the lab could not provide sufficient pressure and flow rate for the laser cooling system, a plastic tank was prepared to keep water supply. The water stored in the tank was then pumped into cooling pipes. Figure 3.7 is a picture of the Argon Ion laser used in the experiment, and Figure 3.8 shows the picture of the water cooling system.

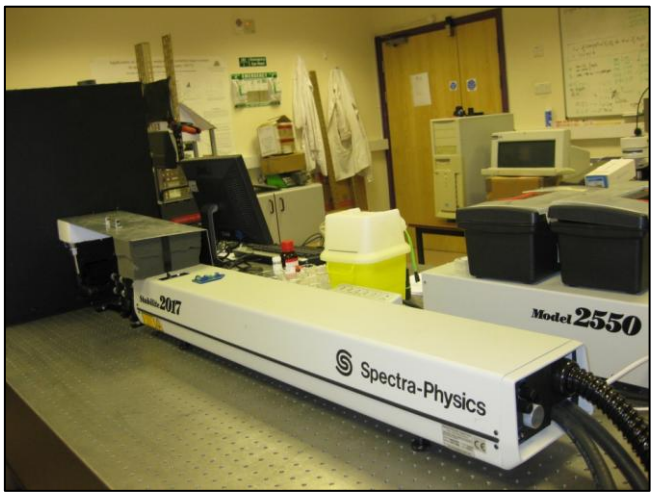

Figure 3.7 the Argon Ion laser applied in the experiment as a light source.

Figure 3.8 The water was stored in a tank and then pumped into the cooling system.

From Yang et al.[102], when choosing a wavelength to a planned experiment, the following should be considered: sufficient laser power, acceptable temporal and spatial mode structure, and adequate stability. Taking into account of material in the experiment, in order to reduce the thermal effect of near-infrared radiation, the 488nm wavelength visible light is selected, and the laser was maximally powered up to 2 Watts. This is similar to what was used, for example, by Scheffold [40], a high power (2W) Argon Ion laser with λ=488nm was employed in a typical DWS setup for polydispersity study and particle concentration effect research; in the experiment run by Viasnoff et al.[103], an Argon Ion laser operating at a wavelength of λ=514nm with a maximum output power of 1.6W was involved for particle sizing using polarized light. The results from our research proved this was a correct choice.

The optical system consisted of some optical lenses which were located between the laser machine and the sample slab. The two lenses (manufactured by Photon Control) were installed on optical rails that were precisely fixed on the central line of the optical system. These lenses were employed to expand laser beam with an appropriate width. The distance between the lenses was 60mm to guarantee that the radius of the laser beam was expanded to a diameter of approximately1.5mm when it reached at the sample. The arrangement is shown in Figure 3.9. Because of this design, the light can uniformly illuminate an area of the

incident face which was much wider than l^* [87] and the beam width was significantly larger than the sample cell thickness L [40].

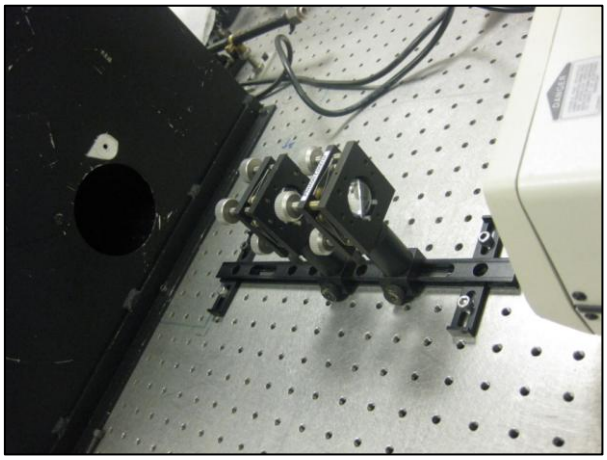

Figure 3.9 Two lenses with a distance of 60mm between each other were used to expand the laser beam.

The CCD camera is a key component in optical system, and the camera used in this work is Ultima APX1, manufactured by Photron. The high-speed digital imaging system includes a CCD, an APX processor, and a PC installed with picture recording software rented from Engineering and Physical Sciences Research Council (EPSRC) of the UK which is a government agency for funding research and training in engineering and the physical sciences. This high-speed imaging system offers high solution for our experiment. The CCD provides a frame rate up to 2000 fps at the full resolution and up to 120000 fps at the reduced resolution. It is highly sensitive to light and suitable for low noise and high dynamic range. Using the processor and the software, picture recording can be synchronized and directly stored in various formats. Figure 3.10 shows a part of the device.

Figure 3.10 A part of the CCD system: APX processor and PC installed with synchronizing software.

In operation, the CCD was set to a frame rate of 100000 fps with a resolution of 128*32 pixels. Chapter 4 will further discuss how to find the suitable frame rate and resolution. The data recording function can be provided in four modes, and the start mode was chosen for this research. Based on these setting, in each experimental run, 1572864 frames of image were recorded, which took just about 15 seconds. The superiority of CCD was obvious as data recording time was reduced to seconds. Each pixel of the imaging sensor served as an independent detector, and noise was reduced by averaging over thousands pixels.

3.5.2 Sample Cell System

The sample cell system is another important component in the experiment. It includes sample cell, protective box, syringe pump and a solution reservoir.

The protective box is a metal box painted in black. The sample cell, CCD camera, and a portion of the laser beam were shielded inside. This box worked as a barrier to isolate the laser radiation, block the power leakage and prevent the light from external environment. Inside the box, the sample cell was mounted on an optical platform which could be adjusted in pitch or on roll. This adjustment was needed to ensure the position of sample cell which located at the centre of the light path, so that the middle area of the sample cell was illuminated. Since a backscattering geometry was used in the experiment, the CCD camera was placed on the same side of the sample cell. The distance from the CCD to the sample cell

was approximately d=14.5cm in the horizontal direction and D=9.5cm in the vertical direction. The details of configuration in protective box are shown in Figure 3.11.

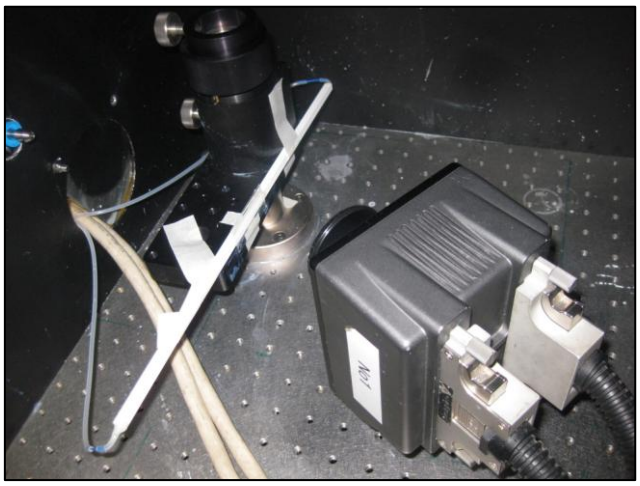

Figure 3.11 The sample cell, CCD camera, and a portion of the laser beam were shielded inside the protective box.

The sample cell was a small slab to keep particle solution. Because the research was to detect micro/nanoparticle size in static and dynamic fluid, a specific capacity and a particular dimension of this small component were required. They were designed in different sizes with different material. The first type was made up of microscope glasses with a dimension of $1x75x25mm^3$ and the thickness of 1mm. A microscope glass was cut into two equal parts with a dimension of $75x12.5x1mm^3$. They then were glued on the top of another microscope glass with a gap between them. The gap was 1mm in width. After that, a microscope cover slide thick 0.17mm was covered and glued on the top of them to seal the gap. Hence, a small channel with a dimension of $1x1x75mm^3$ was constructed. Finally, small tubes with 0.1mm inner size were connected on both side of the channel, and black tape was affixed on glasses to reduce light scattering from the area around the channel. Figure 3.12 shows the cell.

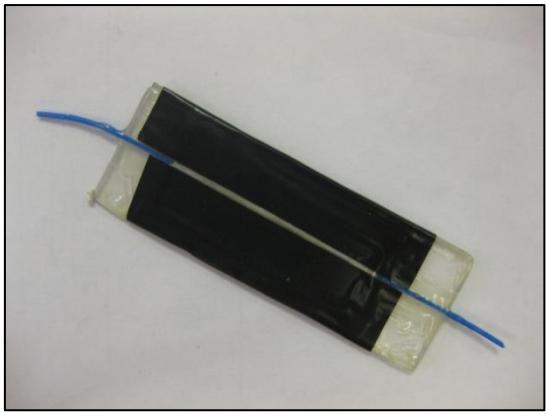

Figure 3.12 Sample cell made of microscope slides with a 1x1x75mm^3 channel.

Another type of sample cell was made of white plastic square-tubes with dimensions of 3x3x180mm^3, 3x6x180mm^3 and 6x6x180mm^3. A slot with dimension of 1.5x50mm^2 was opened on one side of each tube. The slot was sealed by a microscope cover slide with thickness of 0.17mm for observation and light incident. Finally, plastic tubes with an inner diameter of 1mm were connected to both sides of the square tube. The sizes of the channel were 3x3x180mm^3, 3x6x180mm^3 and 6x6x180mm^3. Figure 3.13 shows the picture of the sample cells.

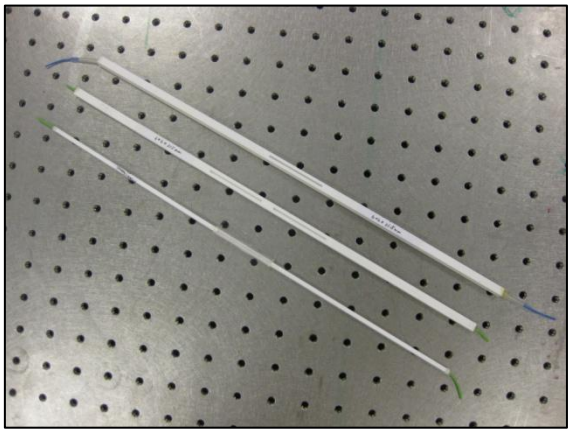

Figure 3.13 Sample cells made of plastic square-tubes with channel dimension: 3x3x180mm^3, 3x6x180mm^3 and 6x6x180mm^3, respectively.

Apparently, both sample cells met the DWS requirement that the sample thickness is $L > l^*$.

The experiment was carried out not only under the static condition in which the particle suspension was stagnant in sample cell, but also under the dynamic condition in which the solution flowed in the sample cell. Due to the small volume of the sample cell, particle solution was injected into the slab by a syringe pump (KDS100, KD Scientific). It is a classic

syringe pump with a wide range of flow rate. Suspension was injected into the sample slab by the pump, and it was then discharged into the reservoir. Figure 3.14 shows the apparatus for infusion and discharge process.

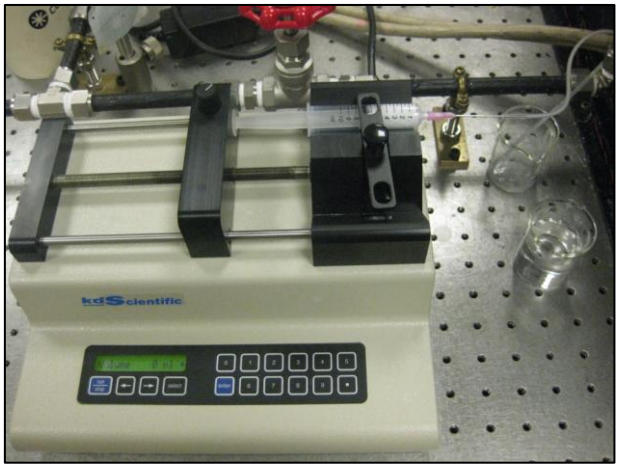

Figure 3.14 Suspension in syringe was injected into sample cell by syringe pump, and finally discharged into reservoir.

3.5.3 Material and Preparation

Polystyrene (PS) micro/nanoparticle solutions manufactured from styrene were used in DWS experiment. PS is a kind of plastic with lightweight, and easy to be coloured and fabricated. It is normally applied to make durable products, because it is a versatile material that can be made into sheets, beads, foam. The latex solution manufactured from polystyrene was normally prepared by emulsion polymerization process to form particle suspension in solution.

The PS suspensions used in the experiment were purchased from Sigma-Aldrich and Duke Scientific with the particle diameter ranging from 60nm to 3200nm (See Figure 3.15 and Figure 3.16). They were manufactured by Thermo Scientific and packaged in 1ml, 2ml, 5ml or 15ml volume. They are white, similar to milk, and no smell. They are made from polystyrene or polystyrene cross-linked with divinylbenzene, and dispersed in deionized water with a trace of amount of surfactant to inhibit agglomeration and promote stability. This largely reduces the particle clumping. The solutions have a pH of 5-8, and the boiling point and melting points are same as that of water. The microsphere density is 1.05g/cm^3 with a 1.59 index of refraction at 589nm wavelength. The solution with diameters of 60nm and 3200nm were packaged as aqueous suspension at 1% solid by weight; and the particles with

diameters of 100nm, 300nm, 500nm, 820nm and 1100nm particle solution have the concentration of 10% by weight. For example, LB8 solution contains particles with average diameter of 820nm and has a size distribution of $\sigma/D = 0.17$ where σ denotes the standard deviation of the size distribution. Other solutions have a similar value of σ which indicates a very narrow size distribution.

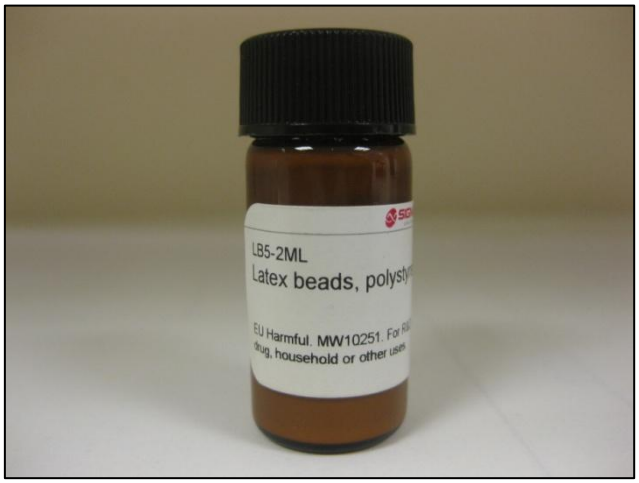

Figure 3.15 2ml 500nm latex beads solution with 10% in weight purchased from Sigma-Aldrich.

Figure 3.16 15ml 3200nm latex beads solution with 1% in weight purchased from Duke Scientific.

In order to make appropriate particle concentrations, the solution was diluted. The dilution process followed the guideline provided by the manufacturer. First, a portion of stock solution was taken to a clean beaker using syringe; an appropriate amount of distilled water

was then added to the concentrated solution. Finally, the suspension was stirred to ensure uniform mixture. From the information provided by Thermo Scientific, the diluted suspensions may not be stable over time. Therefore they recommended making the diluted suspensions as required rather than storing pre-made dilution. As such, the diluted solution required in each test was prepared on the day of the experiment to be conducted. After each test, the used solution was disposed. In the research, a variety of concentrations, from 0.1% in weight to 10% in weight, were prepared. Figure 3.17 shows the appearance of 300nm latex suspensions with different concentrations.

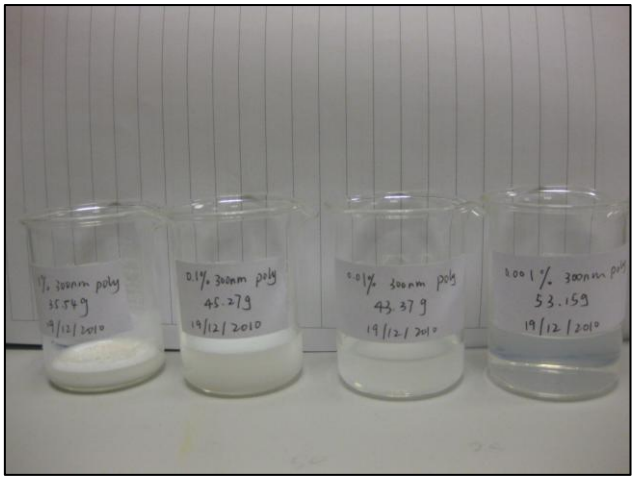

Figure 3.17 300nm latex suspensions with different concentrations: 1%, 0.1%, 0.01% and 0.001% (from left to right).

3.6 Summary

DWS measurement dose not require the knowledge of wave vector for particle sizing, therefore the angle between incident and detected light is not critical as in DLS. Transmission geometry is traditional, requiring access to the sample slab from two sides. However, backscattering only needs access to a sample cell only from one side. Therefore, comparing with backscattering, transmission geometry has space limitation. Also, in backscattering geometry the transport mean free path l^* is not a compulsory parameter when interpreting the autocorrelation function. Thus, it is more convenient for particle sizing computation, and is widely used in real-time measurement in applications.

Based on the fundamental experimental set-up, some apparatus have been added to enhance the power of DWS. Conventional DWS often uses PMT as light detector, but in the improved

method, high speed CCD camera is increasingly employed as a multi-speckle to reduce the measurement time. CCD chip acts as an array of PMTs, all of which are positioned at nearly identical scattering vectors. As a result, the time-averaging and the ensemble average can be carried out in the same time.

Considering the complex fluid studied in this work, the CCD backscattering geometry was used. The illumination was provided by an Argon Ion laser at 488nm wavelength with maximum 2W power. Polystyrene particle solutions with a wide range of diameter were diluted into suspension with different concentrations, and then injected into the sample cells. The sample cells with different volumes were made of glasses or plastic, and all of them met the requirements of DWS: the sample thickness $L > l^*$. The experiment was conducted from February 2009 to September 2011. Totally, about 2000 experiments were performed during this period. A large number of particle images were captured at a frame rate of 100000 fps and 128*32 pixels. These pictures were recorded, processed and exported to PC for analysis.

Chapter 4

Particle Sizing and System Calibration

4.1 Introduction

DWS is an improved DLS for measuring particle size in colloidal suspensions, emulsions, foams and other complex fluids. Considerable progress has been made in understanding multiple light scatterings from random medium in static condition and dynamic condition. It is anticipated that laser power and suspension concentration also have an important influence on particle size determination, but experiments are limited. Therefore, in order to gain a deeper insight of laser power and concentration effect on particle sizing in DWS, the experimental research has been conducted. This chapter aims to present the experimental details, the result of particle sizing and system calibration obtained using standard particle suspension.

The particle images were collected using backscattering geometry and a high speed CCD camera. A tiny time scale interval which was 1/100000 existed between two pictures. Hence, the pictures exactly recorded the scattered light fluctuation in this short recording period. An ensemble averaging was performed on the light signal to generate an autocorrelation function which contained the dynamic information of the scattering medium. Using the Stokes-Einstein relation, the autocorrelation function, usually an exponentially decaying function, then was inverted to obtain the particle size. However, a systematically calibration was required due to different experimental conditions in this research.

The calibration was for the resolution of CCD camera, the absorption effect, and the γ-factor determination. The resolution of CCD camera is inversely proportional to the frame rate, meaning that a good definition of picture will reduce the speed of data capture. The absorption effect is taken into account because it will affect the value of the transport mean free path l^*, and vary the light intensity fluctuation. The γ-factor is a parameter which is

dependent on the boundary condition of the experimental set-up. The value of γ was discussed in previous studies by other researchers, but it needs the verification in the system.

4.2 Particle Sizing

4.2.1 Optical Microscope Observation

The optical microscope (DM2500 M, Leica) was used to visualize the nano- and micro-particles. This microscope had an image field sizes from 20mm to 22mm and all the way to 25mm. The observation area was expanded, and the time for scan specimen was reduced by this wide image field. The microscope had N PLAN achromatic objective series, which guaranteed the image obtained always have a high-contract, pin sharp and full of details. In addition, it provided 1x, 1.5x and 2x optical magnification, enabling the microscope to externally magnify the images. Normally, the picture of specimen can be exported to PC through the eyepieces. In this experiment, in order to get the real-time particle images which described particle's Brownian motion, a 4910 series of Cohu high performance monochrome CCD camera was used. This camera worked with high resolution and high sensitivity under a broad range of light level. It had a microlens sensor, to reduce the dark current, lag and blooming to improve the dynamic range and spectral characteristics of the pictures.

With the help of microscope and Cohu CCD camera, the pictures of particles were displayed on a monitor as shown in Figure 4.1. These particles have a dimension of 1100nm, dispersing in a solution with concentration of 1% in weight. The images were taken under 100x objective and 2x optical magnification. Figure 4.2 shows particles with diameter of 300nm in 1% concentration under the 100x objective and 2x optical magnification. Because the particles were suspended in the solution, under Brownian motion, they moved randomly. Their movements were recorded by the Cohu CCD camera through the real-time recording software. Figure 4.3 shows a snapshot of particles with diameter of 1100nm that was capture by the camera. It is obvious that the sample particles have regular sphere shape with a narrow size distribution.

Figure 4.1 The image of particles with diameter of 1100nm under microscope with total 200x magnification.

Figure 4.2 The image of particles with diameter of 300nm under microscope with total 200x magnification.

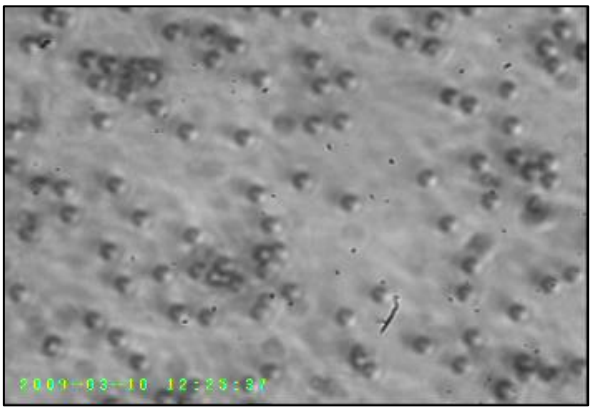

Figure 4.3 A snapshot of 1100nm-diameter particle under CCD monitoring. This picture is a frame image captured from a video in which the particles were in Brownian motion.

4.2.2 DWS Experimental Preparation

After the visualization of micro/nanoparticles under microscope which provided a direct impression, the DWS experiment was conducted. The stock latex beads solutions with particles diameter of 100nm, 300nm, 500nm, 820nm and 1100nm were diluted with distilled water to produce a wide range of concentration, from 10% to 1% in weight. The sample cell was then mounted on the optical platform. The Argon Ion laser was switched on, followed by a calibration and adjusting of the position of sample cell to guarantee that the laser was directed to the central line of the optical system and incident at the proper point of the sample cell. After that, a light spot approximately 1.5mm was focused on the sample. Particle sample was then injected into the sample cell till the channel was fully filled. High speed CCD camera, processor and PC were then switched on, and data collection was started.

4.2.3 Data Collection

The APX CCD was operated on a start trigger mode; it measured many points in the space simultaneously with a frame rate of 100000fps and a resolution of 128x32 pixels. Each pixel had a size of 17μm. For each run of the experiment, 1572864 frames were collected in a time scale of 15.7 seconds to ensure measurement accuracy, making real-time autocorrelation function possible. Because the evolution of the interaction and structure of the fluid was quick[104], the images were saved in the format of BMP which has a small file size. This format was chosen for the storage of the complex, real-world images. By storing each pixel individually, the accuracy and quality of the image were well reserved.

According to Viasnoff et al.[103], an accurate measurement of the correlation function requires that the fluctuations in the intensity needs to be measured over many fluctuation periods. For example, ~104 speckle lifetimes is needed to achieve ~ 1% accuracy. They presented that [103], if N is the number of speckle in CCD array's field, then dealing with the data likes having N-dependent sampling of intensity data processing simultaneously because the fluctuation of each speckle is independent; as a result of a sufficiently large N, the ensemble average on speckles can replace the time-averaging. Sampling the system over a long time was not necessary, and a snapshot of the system was sufficient to study the actual dynamic process. Therefore, in this experiment, 10000 frames in each experiment were selected and transmitted to the computer for further processing. Although these pictures only evaluated the decay time interval of 0.1 second, the information contained was sufficient to

describe the quick evolution of the interaction and structure of fluid. Figure 4.4 is a frame of the particle image taken by the high speed CCD camera.

Figure 4.4 A frame of particle images taken by APX CCD camera.

4.2.4 Data Processing

The series of particle images contained the information of the light intensity fluctuation. After laser beam incident to the sample cell, light is scattered by *N* particles in the solution and then detected in the far field away from the sample cell. For a single particle, the scattered field received by the detector is E_0. The superposition of the scattered fields from each particle contributes to a total scattered field E , which can be expressed as[87]

$$E(t)=\sum_{i=1}^{N}E_0\exp\left[iq\bullet r_i(t)\right] \tag{4.1}$$

where q is the scattering wave vector, $r_i(t)$ is the position of the *i*th particle. Measuring $G_1(\tau)$ can detect the light's small displacements up to hundredths of a wavelength of the radiation, therefore, in the multiply scattering system, the temporal autocorrelation function is[46]

$$G_1(\tau)=\left\langle E(t)E^*(t-\tau)\right\rangle \tag{4.2}$$

The normalized electric field autocorrelation function is given [46, 87]

$$g_1(t)=\frac{G_1(t)}{G_1(0)}=\frac{\left\langle E(0)E^*(t)\right\rangle}{\left\langle |E|^2\right\rangle} \tag{4.3}$$

The normalized intensity autocorrelation function of the scattered light is[46]

$$g_2(\tau)=\frac{\left\langle I(t)I(t-\tau)\right\rangle}{\left\langle I\right\rangle^2} \tag{4.4}$$

where I is the scattered light intensity. The intensity autocorrelation function characterizes the intensity fluctuation received by the detector. According to the Siegret relation, the field fluctuation and intensity fluctuation have the following relationship[85, 88]

$$g_2(\tau) = 1 + \beta \left| g_1(\tau) \right|^2 \tag{4.5}$$

where β is the coherence factor which is a constant determined primarily by the collection optics of the experiment[87]. According to Gisler et al.[105], a maximal value $\beta = 1$ could be used. Therefore,

$$g_2(\tau) = 1 + \left| g_1(\tau) \right|^2 \tag{4.6}$$

By using CCD camera as a detector, the light signal is collected in parallel. Thus, the calculation is carried out for several sets of pixels in the same time. To investigate the system's dynamic change in time, the ensemble averaged and the time averaged autocorrelation function of the scattered intensity fluctuations are processed simultaneously. The autocorrelation function can be calculated for different pixels for the same q of scattering vector and then averaged in time scale. From Cipelletti et al., the un-normalized intensity autocorrelation function $G_2(q,\tau)$ is expressed by averaging over the appropriate set of pixels[97]:

$$G_2(q,\tau) = \left\langle \left\langle I_P(t) I_P(t+\tau) \right\rangle_\phi \right\rangle_t \tag{4.7}$$

where $I_P(t)$ is the pth pixel intensity at time t, $\langle ... \rangle_\phi$ denotes the spatial averaging over all pixels, and $\langle ... \rangle_t$ indicates average over time. The normalized intensity autocorrelation function is computed from

$$g_1(q,\tau) = G_2(q,\tau) \Big/ \left[\left\langle \left\langle I_P(t) \right\rangle_\phi \right\rangle_1 \left\langle \left\langle I_p(t) \right\rangle_\phi \right\rangle_2 \right] \tag{4.8}$$

where $\langle ... \rangle_1$ means the average from time $t = 0$ to τ, $\langle ... \rangle_2$ represents time average from $t = \tau$ to entire running time.

A normalization with the mean intensity can also be performed[78],

$$g_2(t) = \frac{\left\langle \left\langle I(x,t) I(x,t+\tau) \right\rangle_t \right\rangle_x}{\left\langle \left\langle I(x,t) \right\rangle_t \right\rangle_x^2} \tag{4.9}$$

where $\langle ... \rangle_x$ indicates average over the two-dimensional CCD matrix. In Equation(4.9), $\left\langle \left\langle I(x,t) I(x,t+\tau) \right\rangle_t \right\rangle_x = \left\langle \left\langle I(x,t) I(x,t+\tau) \right\rangle_x \right\rangle_t$, meaning that the autocorrelation functions are first averaged over pixels and then on time. To ensure that the normalized field autocorrelation function $g_1(\tau)$ decays from 1 to 0, the averaging function was modified as follows[78]

$$g_2(\tau) = \left\langle \frac{\left\langle I(x,t) I(x,t+\tau) \right\rangle_t}{\left\langle I(x,t) \right\rangle_t^2} \right\rangle_x \tag{4.10}$$

by dividing and averaging sequence modification to avoid the non-uniform illumination which prevents $g_2(\tau \to \infty)$ approaching 1.

A C++ programme was written to calculate the ensemble averaged autocorrelation function. First, the field autocorrelation functions are collected for each pixel. Because the sample solution was illuminated by a broad beam and the suspension system was homogenous, the scattering volume was large enough to be statistically representative of the whole sample. Therefore, all speckles were processed in parallel for the intensity correlation determination in the same time; the pixel averaging was then performed. Finally, an averaged intensity autocorrelation function was generated. The code of custom-written C++ programme can be found in Appendix A.

The technique of multiple-speckle has significant advantage[97]: by substituting data sequentially with parallel collection, much longer time delays are accessed in a given measurement time scale. As such, the processes dramatically decrease the sampling time, and increase the statistical accuracy of the DWS.

4.2.5 Data Analysis

In backscattering geometry experiment, if the sample has an infinite or a semi-infinite thickness, that is $L > 50l^*$ or $L > 20l^*$, the intensity autocorrelation function Equation(2.10) can be simplified as[87]

$$g_1(t) = \frac{\exp\left[-\left(z_0 / l^* \right) \sqrt{6t/\tau_0} \right]}{1 + \left[(2/3) \sqrt{6t/\tau_0} \right]} \tag{4.11}$$

Substituting Equation(4.6) in Equation (4.11) , it can be derived

$$\sqrt{g_2 - 1} = \frac{\exp\left[-\left(z_0/l^*\right)\sqrt{6t/\tau_0}\right]}{1+\left[\left(2/3\right)\sqrt{6t/\tau_0}\right]} \tag{4.12}$$

The expression of τ_0 can be transferred from Equation(2.2) , giving the diffusion coefficient of spherical particles

$$D_0 = 1/\left(\tau_0 k_0^2\right) \tag{4.13}$$

where D_0 is defined as the single particle short time diffusion constant. If the thickness of the sample slab is much smaller than the transport mean free path, $L \gg l^*$; this is what in this research. For short correlation times $t < \tau_0$, Equation(4.12) can be modified as[40]

$$g_2(t) - 1 = \exp\left[-2\gamma\left(6t/\tau_0\right)^{1/2}\right] \tag{4.14}$$

where

$$\gamma = \frac{z_0}{l^*} + \frac{2}{3} \tag{4.15}$$

The parameter $z_0 \sim l^*$ is interpreted as that the distance from the point where light is incident to the point z_0 where photons start to propagate diffusively is expected to be of order l^* inside the sample[87, 106].

Using the data processed by C++ programme, logarithmically plotting the graph $\ln\left[g_2(t) - 1\right]$ against $\sqrt{t}$ will gives a straight line with slope of

$$S = -2\gamma\sqrt{6/\tau_0} \tag{4.16}$$

In this formula, γ is a constant with no unit, depending on the boundary conditions in the photon diffusion process. From Equation (4.13) the Stoke-Einstein relation

$$D_0 = \frac{K_B T}{6\pi\eta_s R} \tag{4.17}$$

the radius of the particle can be calculated as

$$R = \frac{16\gamma^2 n^2 \pi K_B T}{S^2 \lambda^2 \eta_s} \tag{4.18}$$

where n is the refractive index of the solvent, normally 1.33 for water at 20^oC; λ is the wavelength of the incident light, 488nm for Argon Ion laser; γ is the diffusion constant which is experimentally observed with the range from 1.5 to 2.7[87]. In this experiment, $\gamma = 2.0$ was used, which will be discussed in the next section. K_B is the Boltzmann constant with the value of 1.38*10^{-23} J/K, and T is the absolute temperature of experimental environment with a value of approximately 300K in this experiment; η_s is the viscosity of the suspension, which for water at 20^oC, is $\eta_0 = 0.001$Pa*s. For particle solution[107]

$$\eta_s = \eta_0(1+2.5\phi) \tag{4.19}$$

where ϕ is the volume fraction of suspension.

Figure 4.5 shows the autocorrelation functions of time t for particles with different size, 300nm, 820nm and 1100nm. They decay from 1 to 0 with various decay rates.

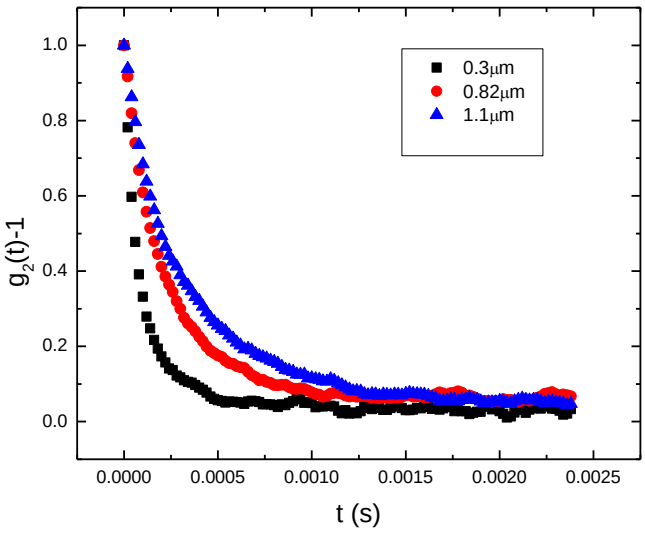

Figure 4.5 Autocorrelation functions for 300nm-, 820nm- and 1100nm-diameter polystyrene particles in 1.8% (volume fraction) solution, respectively.

Figure 4.6 shows the logarithmically plotting of $\ln\left[g_2(t)-1\right]$ as a function of $\sqrt{t}$ for particle of different particle size. It is obvious that the data are fitted very well by straight lines except a few fluctuations at large correlation time. This is due to the short non-diffusive light paths in the diffusion; diffusion approximations are valid for long path and break down for short

path[87]. However, the photo loss in the beginning of the decay can be neglected due to the container size $L > l^*$ in the experiment[40].

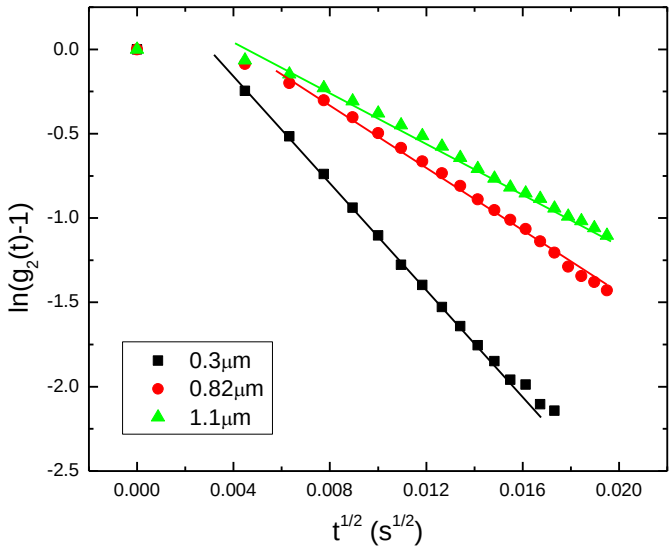

Figure 4.6 Intensity autocorrelation from a typical DWS measurement in backscattering geometry. Plotting $\lg\left[g_2(t)-1\right]$ vs $\sqrt{t}$, shows linear decays over a broad range of decay times.

Table 4.1 shows the slopes of $\ln\left[g_2(t)-1\right]$ against $\sqrt{t}$ for 300nm-, 500nm-, 820nm- and 1100nm-diameter particles at 1.8% volume fraction. Fitting to Equation(4.18), the values of γ were obtained for different particle size, and the values in Table 4.1 agree well with that reported in previous study. Therefore, the backscattering CCD-DWS system in our experiment has been proved reliable.

Table 4.1 The values of γ are determined from the slopes and other parameters for 300nm, 500nm, 820nm and 1100nm latex samples respectively with 1.8% volume fraction.

D (nm)	*Φ*	*k = 2πn/λ*	*K_B (J/K)*	*T (K)*	*η (Pa·s)*	*S*	*γ*
300	1.8%	17124300	1.4E-23	300	0.001045	211.3	2.126
500	1.8%	17124300	1.4E-23	300	0.001045	167.9	2.183
820	1.8%	17124300	1.4E-23	300	0.001045	134.3	2.235
1100	1.8%	17124300	1.4E-23	300	0.001045	117.8	2.270

Table 4.2 displays the particle sizing results when the value of $\gamma = 2$ is specified for different particles with various volume fractions.

Table 4.2 The particle sizing for 300nm, 500nm, 820nm and 1100nm latex beads samples respectively with various volume fractions, when $\gamma = 2$ is specified. D is the standard particle diameter, D_{DWS} is the particle diameter measured in experiment. ε indicates the accuracy and error of the measurement.

D (nm)	Φ	γ	K_B*(J/K)*	*T(K)*	*n*	λ*(m)*	η*(Pa*s)*	*S*	D_{DWS}*(nm)*	ε
300	1.80%	2	1.38E-23	300	1.33	4.88E-07	0.001045	196.52	306	2%
500	3.60%	2	1.38E-23	300	1.33	4.88E-07	0.00109	151.49	494	1.2%
820	3.60%	2	1.38E-23	300	1.33	4.88E-07	0.00109	117.54	821	0.12%
1100	1.80%	2	1.38E-23	300	1.33	4.88E-07	0.001045	104.72	1079	1.9%

4.3 System Calibration

The particle sizing result shown in Table 4.2 indicates that ε is within 5% which defines the small measurement error, therefore, it was proved the reliability of the experimental system for homogeous solution. However, the calibration is required to make the system repeatable and adaptive to various conditions for complex fluid.

The calibration was focused on the specification of the values of some parameters, including picture resolution, frame rate, light absorption and value of γ. In the calibration, the value of γ was experimentally studied associated with the CCD location, and a particular γ was then chosen corresponding to a specific CCD position for the experiment conducted later on.

4.3.1 CCD Frame Rate and Resolution

In order to investigate the short-time behaviour of the particle suspension system, a frame rate of 100000fps was set for the APX CCD camera. It means that the decay time for the correlation function can be accessible as small as micro-seconds with an exposure time of $\tau_0 = 10\mu s$. Physically, τ_0 represents the average time for photon to diffuse one wavelength of the light, and after the time scale, particle randomize the phases of light scattering off it[108]. This frame rate ensured that the measurement was sensitive to the fluctuations of medium. These fluctuations which had a much smaller length scale than the wavelength of light were

probed to be within an extraordinarily wide range of timescales, from 10^{-8} to 10^{5}s[101]. When 100000fps frame rate was applied, the time scale between two images was 10^{-5}s. Therefore, this time scale is small enough to record dynamic process of the particles.

Apart from the frame rate, the resolution of image is another aspect that plays important role in the experiment. The pixel size governs the number of pixels making up the particle projection[109]. If high resolution is required, the number of pixels is large and the size of pixel should be small. Pictures with high resolution constituting much larger files will result in dealing with a large number of pixels and increasing of the analysing time[110]. Therefore, a proper resolution should balance the relation between image quality and the size of the image file. The maximum resolution of APX CCD camera is 1024×1024 pixels, but for the particular frame rate 100000fps, APX CCD camera technically provides a maximum resolution of 128×32 pixels. To find a proper pixel which fits our experiment, pictures with different resolutions were investigated, and the corresponding autocorrelation functions were analyzed. As Figure 4.7 shows, the autocorrelation function of 16×16 pixels pictures is really close to that of full frame picture. Hence it is concluded that the minimum requirement of pixel is 16×16 pixels or above. In order to obtain a good picture with a small file size, the resolution of 128×32 pixels were selected. This resolution was proved to be reliable to obtain the accurate ensemble average.

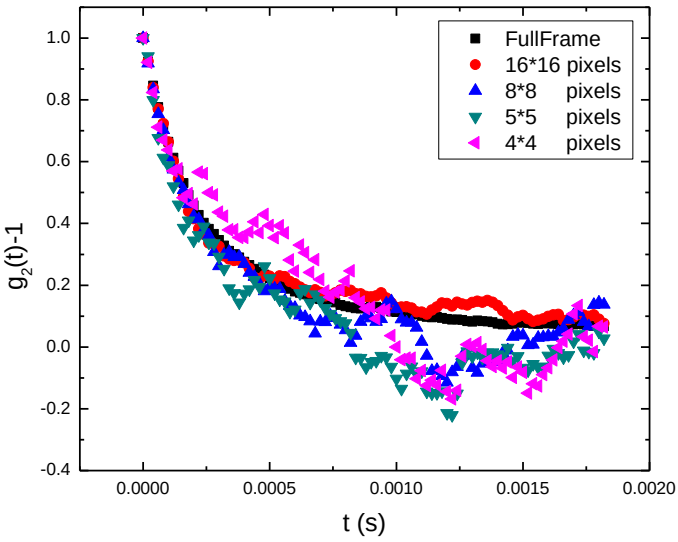

Figure 4.7 The autocorrelation functions $g_2(t)-1$ of different pixels resolutions are showed for the 820nm-diameter particle sample with 1% concentration (in weight).

4.3.2 Absorption

Absorption of light, the inherent property of all mediums, needs to be taken into account in DWS measurement. The effect of absorption is often enhanced in multiple scatterings due to the existence of long scattering paths[111]. Absorption will not only result in local thermal effect that heats the sample[74], but it also alters the distribution of the light path lengths $P(s)$ by reducing the contribution of long paths to the correlation function[90, 106]. From Weitz et al., when the absorption is absent, the expression of $P(s)$ for Equation(2.1) can be modified as[87]

$$g_1(t) = \int_0^\infty P(s)\exp\left[-\left(2t/\tau_0 + l^*/l_a\right)s/l^*\right]ds \tag{4.20}$$

where l_a represent the absorption length of the sample. For the backscattering geometry, we have $t/\tau_0 \to t/\tau_0 + l^*/2l_a$. Equation(4.14) is updated to[87]

$$g_2(t) - 1 = \exp\left[-\gamma\left(6t/\tau_0 + 3l^*/l_a\right)^{1/2}\right] \tag{4.21}$$

As noted in Pine et al.[90], the absorption just shifts the time scale of the correlation function. Therefore, mathematically, the same analysis can be performed as in the case without absorption.

In order to investigate the effect of absorption, the theoretical data with no absorption influence is compared with the real experiment values with different "effective" absorption lengths l_a. Figure 4.8 shows that there is no obvious difference between theoretical value and the experiment data. Due to the absorption, photons are lost, showing that as a round corner of correlation function at small decay time in Figure 4.6. However, Scheffold[40] argued that the photon loss in this correlation time window can be neglected. Therefore, it is concluded that the absorption effect can be ignored in this DWS measurement.

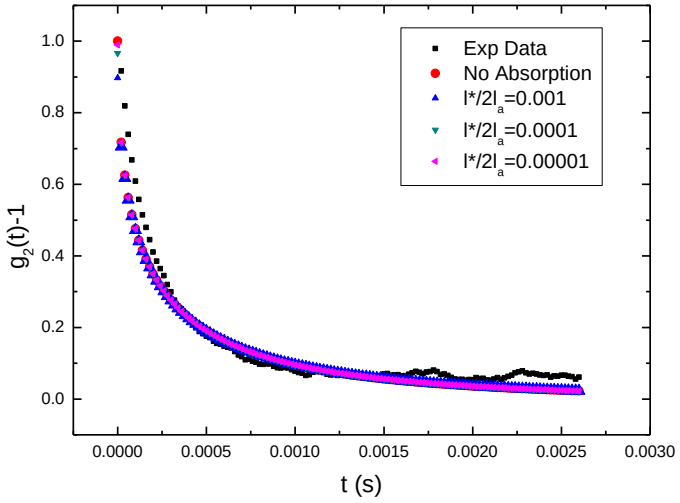

Figure 4.8 Comparison of results of different "effective" absorption lengths l_a, no absorption with the experiment result of the autocorrelation functions for 820nm-diameter particle in 1.8% volume fraction.

4.3.3 The Location of CCD

The backscattering geometry requires access to the sample cell from only one side, which means that the CCD should be located on the same side of incident laser beam to detect the scattered light. Although the angle between the incident and detected light is not as important as DLS, the location of CCD is still critical, because it is the boundary condition which influences the value of γ.

The parameter γ is a constant which reflects the contribution of short non-diffusive light paths to $P(s)$ [87, 112]; it plays important role in determination of the value τ_0. Ultimately, as described in Equation(4.18), it affects the result of particle sizing through its influence on the relax time τ_0. It is difficult to calculate γ because it requires the knowledge of low order scattering processes which is close to sample surface[40, 113]; and the low order scattering principally depends on the parallel polarization of the scattering[112]. So, to determine γ, the channels not only with perpendicular polarization, but also with parallel polarization should be detected. Some practical approaches have been proposed in previous studies, and the value of γ was presented. For example, Horne et al.[114] suggested an average value of $\gamma = 2$ for

all particle sizes. Weitz et al.[87] experimentally observed that the value varies between 1.5 to 2.7 for various particle sizes and polarizations.

In practice, γ is found to depend on the actual experiment set-up, such as the detection angel, sample cell and surface reflections[40]. In this experiment, the sample cell and surface reflection was fixed. Therefore, in order to investigate the values of γ, the detector was located on different position to change the detector angles. Figure 4.9 shows the different CCD locations around the sample cell. The distance between the laser spot on sample cell and CCD camera in the vertical direction is expressed as D and in the horizontal direction d, both with unit of cm.

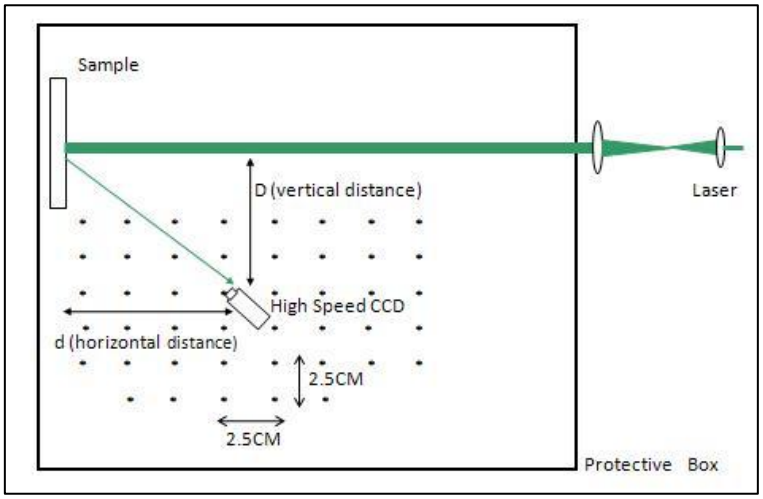

Figure 4.9 The CCD was placed at various locations to work out different values of γ.

For each experiment, the CCD was placed on a particular position. For each location, pictures were taken and processed to generate the autocorrelation function. Analysing the function and substituting the particle size into Equation(4.18) gives the value of γ. These values were used to construct a contour figure as shown Figure 4.10, where the sample cell was located at the left bottom corner with coordinate of (0, 0). In this graph, the legend with different colours reveals different values of γ, warm colour denotes high value and cold colour indicates low value. The high values are in the area of D=6-12cm and d=10-16cm, and the low values are on the top of the graph. Figure 4.11 is the 3D view of contour map. Although, as shown in Figure 4.10 and Figure 4.11 the experiment was carried out in a half field of the backscattering geometry, but it could be determined that the distribution of γ was identical for the other half field because of symmetrical geometry. From Equation(4.18), it is clearly

that high value of γ is associated with slop of the logarithm plotting which represents quick decay. As noted in Weitz et al.[87], long paths decay quickly and short path decays slowly and Equation(4.11) is based on the diffusion approximation and central limit theorem, valid only for long paths. Therefore, the system is calibrated with the highest value of $\gamma = 2$ for the experiments which was conducted later on. For this particular value, CCD was set at the location marked as L. Hereby, for the DWS experiments, the CCD was positioned at location with D=7.5cm and d=14.5cm, and $\gamma = 2$ was recommended.

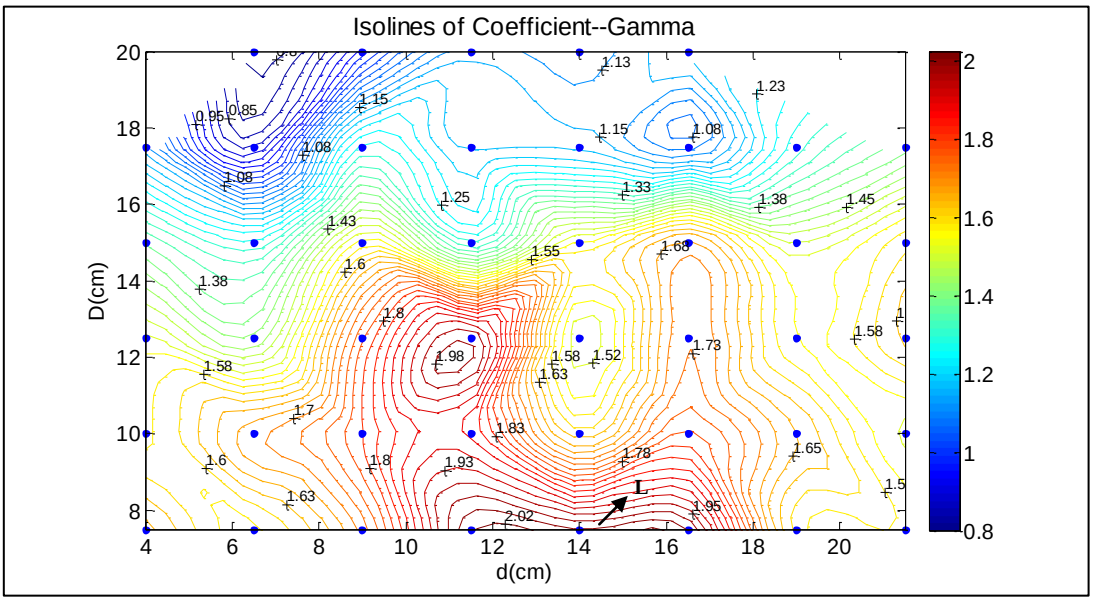

Figure 4.10 The contour plotting of γ.

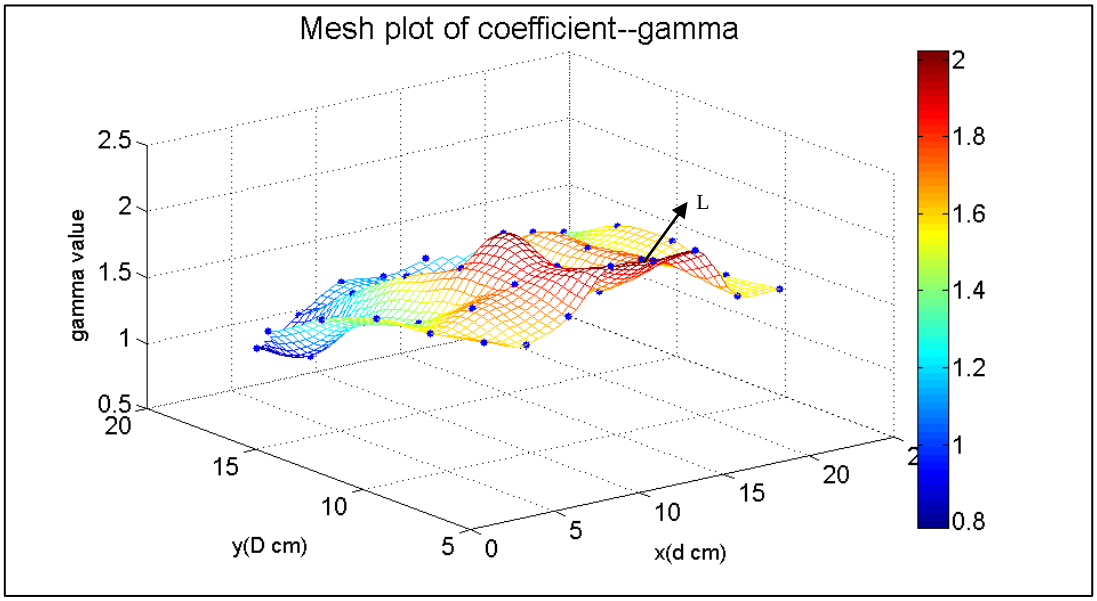

Figure 4.11 3D view of the contour plotting of γ.

4.4 Summary

This chapter gives the details of particle sizing using DWS technique and discusses the DWS system calibration.

At first, optical microscope was used for a direct observation of particles under Brownian motion. The particle suspension was mounted to produce the specimen. In a wide image field of DM2500 M optical microscope, particles were observed clearly after the objective magnification and optical magnification. The pictures were taken and displayed on monitor, displaying particles were under Brownian motion.

The high speed CCD camera was set at a frame rate of 100000fps to take particle pictures with a resolution of 128×32 pixels. For each experiment, 1572864 frames were collected in a time period of 15.7s. These images were taken in sequence with a time interval of 10^{-5}s. All the pixels were ensemble-averaged to get the intensity correlation functions by the custom-written C++ program. The autocorrelation function was processed, and then $g_2(t)-1$ was plotted against time t. The logarithmically plotting of $\ln\left[g_2(t)-1\right]$ against $\sqrt{t}$ produced a linear line with slope *S*. From the Stoke-Einstein relation, particle size can be obtained from $R=\frac{16\gamma^2 n^2 \pi K_B T}{S^2 \lambda^2 \eta_s}$.

Although the DWS set-up was proved to be reliable, the system calibration was necessary. The frame rate, image resolution and light adsorption were considered in the calibration. Comparison between theoretical data and experimental results, it was found that the impact of absorption was minor and could be ignored. Besides, the parameter γ which is dependent on boundary conditions was also investigated. The experimental results revealed that in the backscattering geometry the values of γ depended on the CCD location. High value of γ appeared to be along paths scattering, and coincided with the diffusion approximation. Therefore, for the subsequent DWS experiments, $\gamma = 2$ was used, and the CCD was positioned at the location with D=7.5cm and d=14.5cm.

Chapter 5

Effect of Laser Power on Particle Sizing

5.1 Introduction

A number of factors affect the DWS performance, and one of them is incident laser power which will influence the autocorrelation functions. Laser power is a key element in DWS to provide the light source and illuminate the sample cell. In the past, researchers thought that the particle's motion was not affected by the laser beam which barely altered the amplitude and phase of itself due to the particle's scattering; however, the particle's scattering is characterized by the thermodynamic properties of the system, and these properties may be affected by the introduce of laser beam; therefore, the study of the effect of laser radiation on DWS is indeed an requirement[115]. This chapter will systematically investigate the impact of laser power on particle size measurement for laser power with a wide range of laser radiation.

5.2 Previous Studies

5.2.1 Laser Power Input for DWS

Laser beam is generated by photons which are simulated and emitted from a laser device. The stimulation emission is a procedure in which the energy is extracted from a transition in an atom or molecule. Considering a visible laser, the violet radiation has the highest energy; and the red rays have the lowest power. The laser applied in our experiment has a wavelength of 488nm and is visible laser light with blue and green colour and a moderate energy. In the experiment, the light source illuminated the scattering medium, which was regarded as one of the most important components in DWS system.

The laser power in a conventional DWS experiment is not limited to a narrow range. Different laser powers have been employed in the studies. Some researchers have developed methods for laser power selection based on the research purpose. As noted by Chu[116] and

Yang et al.[102], the laser for particle sizing using light scattering method must have sufficient power, being stable under all expected conditions; otherwise, it could cause distortion in the measurement. Therefore, an appropriate laser power has to be carefully considered and estimated. It cannot be too high or too low. It must be adequate enough to meet the illuminating requirements and avoid unexpected results. Depending on the objectives and experimental set-up, a variety of laser power has been applied in DWS in previous studies.

In using DWS to study complex dry mechanism of film formation, the instrument of Horus, emitting 0.9mW laser radiation, was employed as the light source[117]; similar to our experiment, a COMS video camera was used for scattered light detection in that study. In investigation of inter-particle interactions in sodium caseinate-stabilized emulsions during acidification, 100mW laser power was used by Liu et al.[118]; in their experiment, a photomultiplier was used as the light detector. In a typical DWS setup, which could be run in backscattering and transmission geometry, the time autocorrelation of multiply scattered light was measured by Scheffold[40], and the high laser power of 2W with incident wavelength of 488nm was used. In DWS with a point source and backscattering geometry done by Rega et al., the laser light was powered to 100mW with 530nm wavelength used as the light source[119]; in their experiment, a photomultiplier was used as the detector. The particles in a randomly inhomogeneous turbid medium were studied by Skipetrov et al using DWS[41], in which a laser beam generated at wavelength of 514nm and powered to 1W was introduced into the medium through a narrow fiber-optic light guide. In another work, Navabpour et al. investigated the influence of medium concentration on particle sizing using DWS[44]; in their study, the experiment was designed to exclude the scattered light polarised in the same plane as the incident light, and geometrically excluded the paths shorter than l^*. For this, a laser beam with 532nm wavelength and 100mW of power input was used.

From the previous studies, it can be concluded that the laser power is dependent on the type of light detector and the research objectives.

5.2.2 Laser Power and Particle Sizing

In particle sizing experiment, it has been reported that there is a relation between measured particle size and the incident laser power. In the study of Kondrat'ev et al[120], they used a

laser power with a variable interval 0.07-2 W to investigate particles with the radius of 90nm;they observed the variation in the autocorrelation function with increasing the incident laser power and pointed that the variation was resulted from the laser-induced motion of scattering particles. In the research of determining nano-particles size in a suspension with low concentration, Kuyper et al.[43] focused a laser light to an avalanche photodiode that has high sensitivity to light source; particles with different diameters were studied for a number of tests. Their analysis showed that in the power changed from 300 to 900μW, there was a linear increase in the measured diffusion time. They then concluded that the measured particle size using DWS appeared to be power-dependent; for particles with a moderate size, low excitation power was sufficient to provide an accurate size measurement, but low power laser illumination could be a problem for smaller and less bright particles. Harada et al.[115] found the similar results; when using an Argon laser beam to illuminate a sample cell, they found that, with the laser power adjusted from 0 to 60mW and under improper laser power, the resultant particle size was larger than it should be, and the increase in particle size or laser radiation resulted in larger difference between true and measured sizes.

The previous studies have proved that laser light power is critical for particle sizing, especially for small particles, because small particles scatter less light than large particles. Under some conditions, the measured particle size could not be reliable. Yang et al. [102] have argued that the laser power effect came from the refractive index change of the medium; because the laser power caused local heating and resulted in thermal blooming. The optical index change induced errors in particle sizing. In order to accurately measure the size of micro- and nano- particles, the impact of laser power on the measurement were researched.

5.3 Experimental Methods

The polystyrene latex beads with diameter of 300nm and 500nm were prepared, respectively. A small amount of the suspension was taken out from the stock container and diluted with distilled water to get a variety of concentrations: 1%, 2%, 4%, 6%, 8% and 10% in weight, correspondingly 0.9%, 1.8%, 3.6%, 5.4%, 7.2% and 9% in volume. After that, the diluted solution was injected into a 1x1x50 mm^3 sample cell.

Experiment was conducted in the set-up discussed in previous chapters. For each sample with a particular concentration, the laser were powered to 40mW, 80mW, 160mW, 240mW,

320mW, 640mW, 800mW, 960mW, 1120mW and 1440mW, respectively to focus on the scattering medium. For each sample, 1572864 images were taken in a short period of time; and the images were then processed by the programme presented in Chapter 4 in attempt to find the influence of laser power on DWS.

5.4 Results and Discussion

The results for solutions with the particles of 300nm- and 500nm-diameter were similar to each other, giving evidence that the experimental system had a high repeatability. Hence, one of the data group was chosen for analysis.

The results for 300nm-diamter particles were analysed. Figure 5.1 shows the autocorrelation functions obtained from the 300nm-diameter particle suspension with concentration of 1.8% (volume fraction). The autocorrelation functions can be divided into two groups, with the diving line within the space between 320mW and 640mW. The power in the range of 40mW to 320mW is in low band, and the power from 640mW to 1140mW is in high band. The autocorrelation function $G_2(t)$ superpose for power at and above 640mW, uniformly decay from 1 to 0, as shown in Figure 5.1 (a). The overlapping of the curves indicates the identical particle size. In contrast, the autocorrelation functions $G_2(t)$ for the laser power below 320mW are different. The curves distribute widely and do not have any overlapping. Generally, autocorrelation function should change from 1, meaning maximum correlation, to 0, meaning no correlation at all. However, for low band, all curves starte from 1, but the decay stop at a point above 0, as demonstrated in Figure 5.1 (b). This give evidence of the laser power influence. The autocorrelation functions do not reach zero, and for a broad range of time scale, they remain a constant value. From some particular concentrations, 0.15 with power of 320mW, 0.2 with power of 240mW, 0.3 with power 160mW, 0.5 for 80mW and 0.55 for 40mW, the autocorrelation functions do not decrease to zero, instead they have long tails.

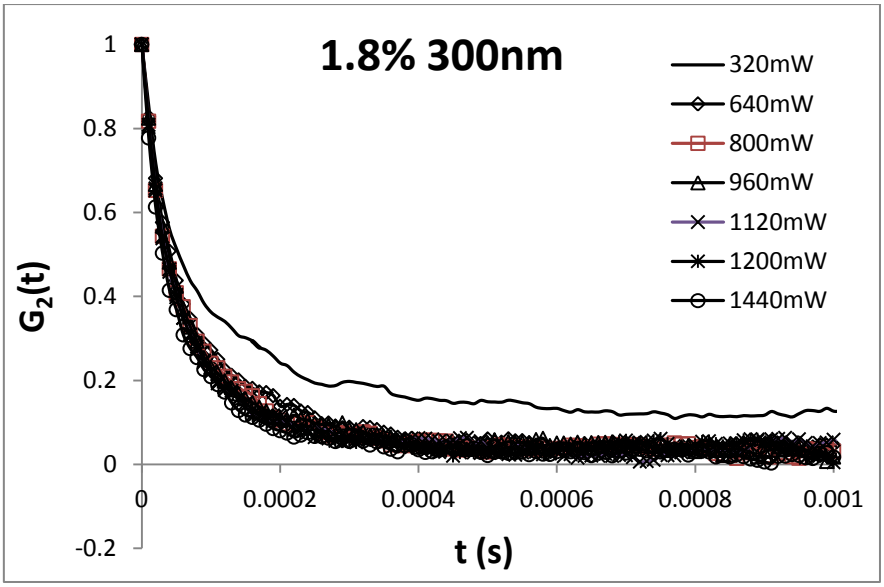

(a)

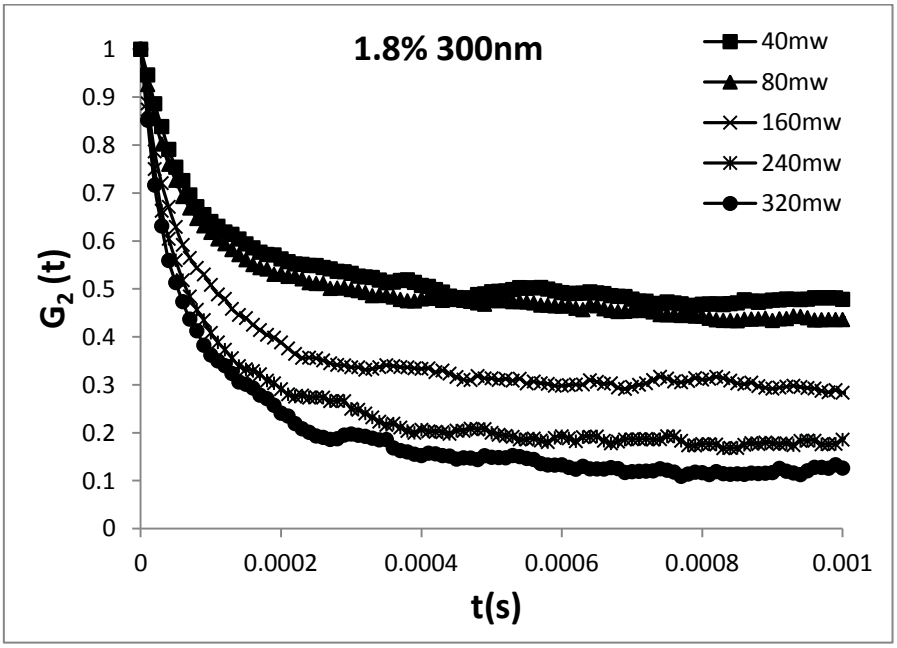

(b)

Figure 5.1 DWS autocorrelation functions $G_2(t)$ for the 300nm latex particles at 1.8% volume fraction with laser powers ranged from 40mW to 1440mW: a) laser power at or above 640mW is sufficient for DWS and all curves from 640mW to 1440mW clap together; b) a large variation displayed for the laser power range between 40mW and 320mW.

Further analysis shows that if the autocorrelation functions are normalised as following,

$$g_2(t) = 1 - \frac{1 - G_2(t)}{1 - G_2(\infty)} \tag{5.1}$$

$g_2(t)$ can decay from 1 to 0. After the normalization, all of the curves superpose together, indicating uniform values. The normalised autocorrelation functions are shown in Figure 5.2 (a). Following the normalization, the logarithm of autocorrelation function $\ln\left[g_2(t)\right]$ was plotted against the square root of time $\sqrt{t}$, and is shown in Figure 5.2 (b). It reveals that approximate linear curves are generated from the logarithm plotting, and the curves are well fitted by a straight line with a slope of -155.34.

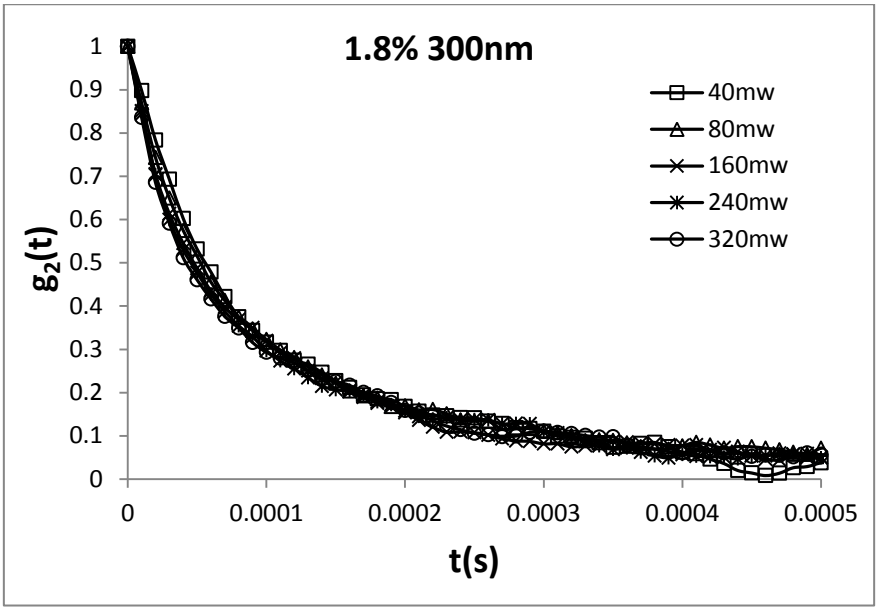

(a)

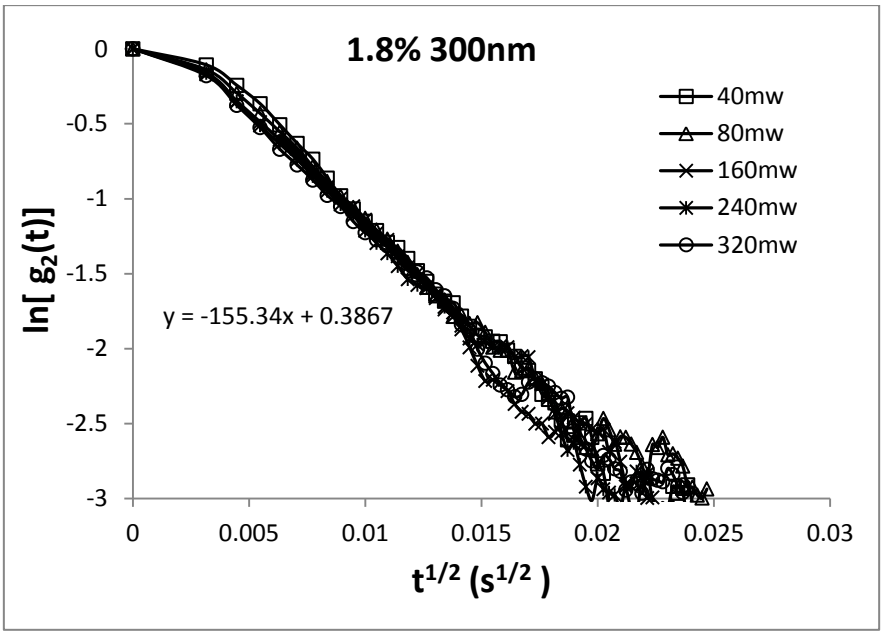

(b)

Figure 5.2 Normalisation of DWS autocorrelation functions $g_2(t)$ for the 300nm latex particles at 1.8% volume fraction with laser powers ranged from 40mW to 320mW: a) normalised $g_2(t)$ covering the full range between 0 and 1; b). logarithm plotting against $t^{1/2}$ shows a linear decay over a broad range of decay times.

The comparison of autocorrelation function and logarithm plotting between high band laser and normalized low band laser also carried out. As seen in Figure 5.3, there are some differences. Shown in Figure 5.3 (a), the normalized low band $g_2(t)$ has a slow decay rate than high band, but the difference is small enough to ignore. Also, there was a little variation for logarithm plotting which displays the slop -155.34 for low band and -211.26 for high band. The difference ε is approximate 33% revealed in Figure 5.3 (b). According to Equation(4.18), the difference ε of slope can be magnified by $1/\varepsilon^2$, and reflects a significant deviation of particle size. Therefore, the low laser band still could not be sufficient to get an accurate result, even it was normalized.

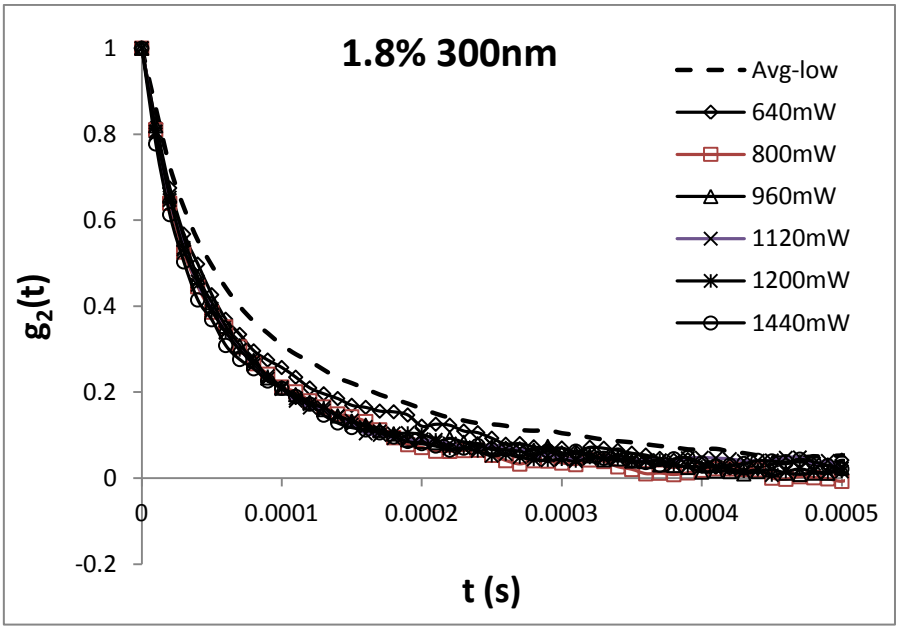

(a)

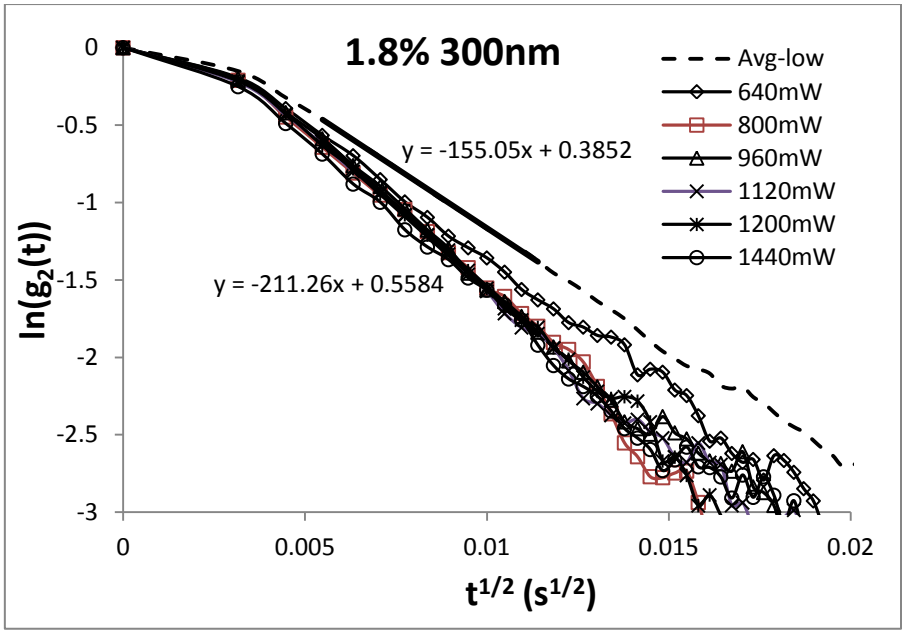

(b)

Figure 5.3 Comparing the normalised $g_2(t)$ of 1.8% volume fraction 300nm suspension in the low laser power band (40mW to 320mW) and high laser power band (640mW to 1440mW): a) plotting $g_2(t)$ against time t; b) log plotting against $t^{1/2}$ shows more than 30% difference in the slopes.

Besides particles in solution with concentration of 1.8%, solutions with other concentrations were also investigated. The autocorrelation functions are similar to that with concentration of 1.8%. Comparison between concentration of 0.9% and 9% under low laser band is shown in Figure 5.4. The normalized autocorrelation function for low band power is compared with those for high band power in Figure 5.5. A significant difference for concentration of 0.9% is found, but the variation for 9% is not as obvious as that for 0.9%. It is revealed that the difference between the normalised autocorrelation function in high band and low band is larger for low concentration solution than for high concentration, meaning that the laser power effect is more significant on solution with low particle concentration than for high particle concentration. A similar situation is shown in Figure 5.6, the logarithm plotting against time square. The difference between the fitting line for the high band laser and that for the low band laser is large for more diluted solution, whereas for concentrated solution, the fitting lines are only slightly different. Furthermore, both Figure 5.5 and Figure 5.6 indicate that the dividing line for low band laser and high band laser is not a constant; it has shifted from somewhere near 640mW for 0.9% solution to somewhere near 320mW for 9%

solution, indicating that the onset of laser power influence has been changed from high laser power to low laser power when the solution is getting increasingly concentrated. It can be concluded that an increase in solution concentration reduced the DWS system's dependence on high laser power supply. In another words, for high concentration solution, if there is an inadequate laser power supply, DWS system still generates a reliable particle sizing result. The result will not be affected by the laser power input.

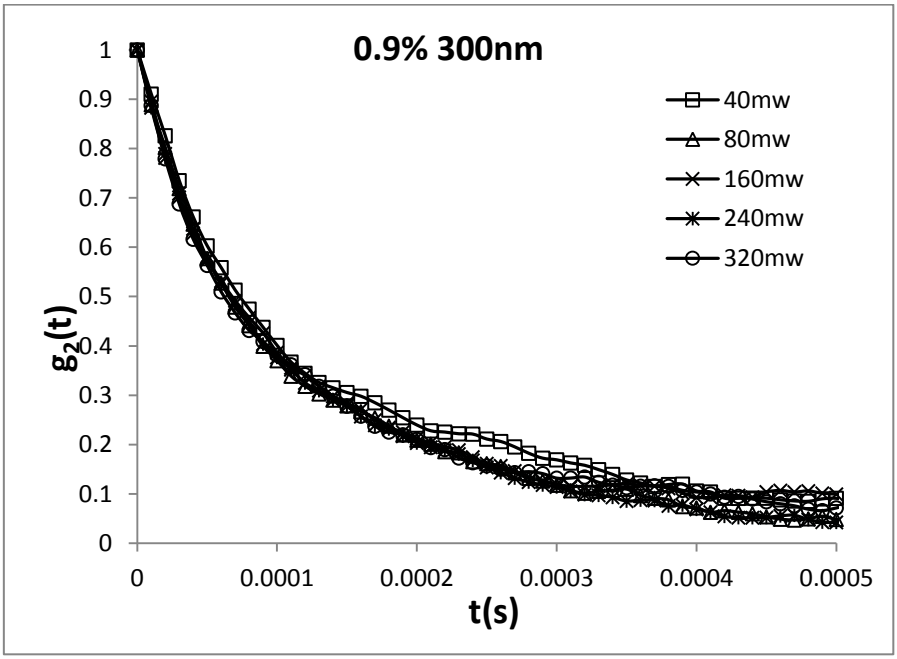

(a)

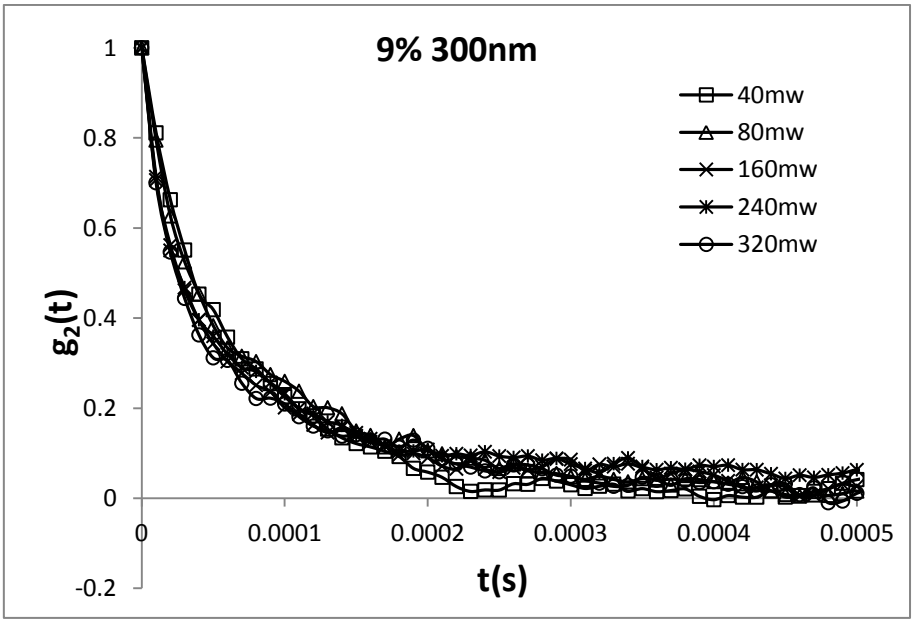

(b)

Figure 5.4 Successful normalization of DWS autocorrelation functions $g_2(t)$ for the 300nm latex particles in the low laser band (40-320mW) for all test cases with the concentration (a) at 0.9% volume fraction to (b) at 9% volume fraction.

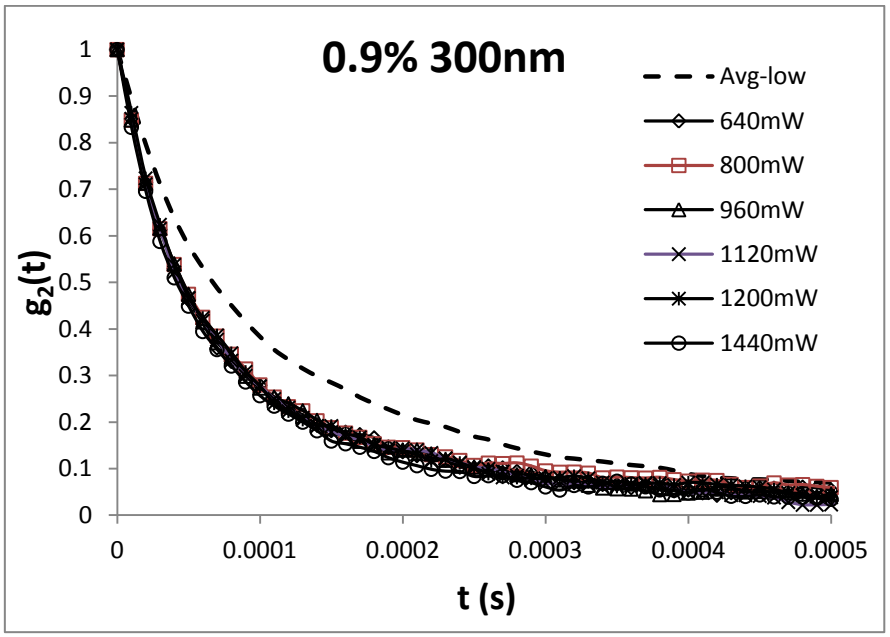

(a)

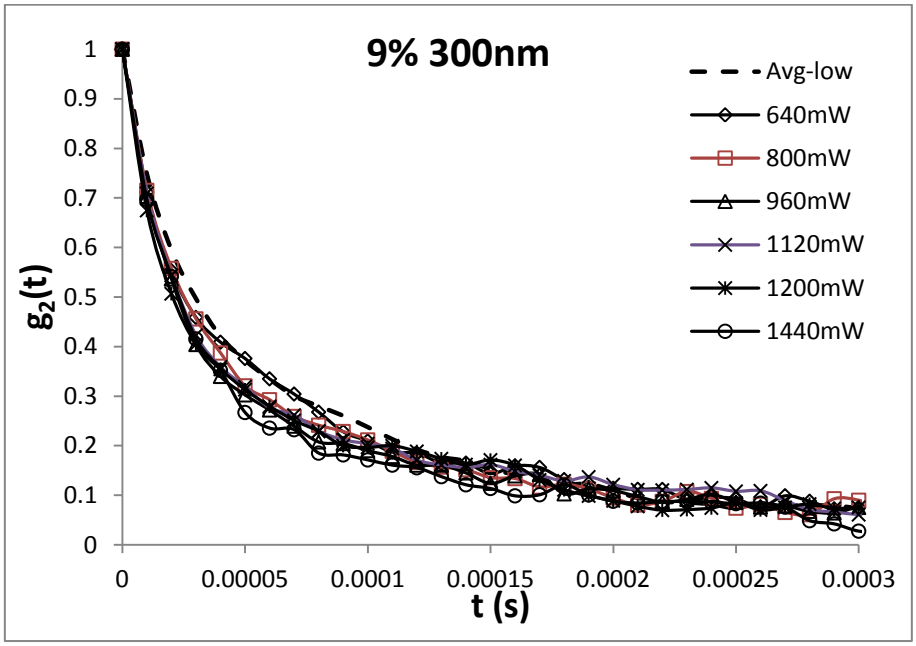

(b)

Figure 5.5 Comparing the normalised $g_2(t)$ of 0.9% and 9% volume fraction for 300nm suspension in the low laser power band (40mW to 320mW) and high laser power band (640mW to 1440mW).

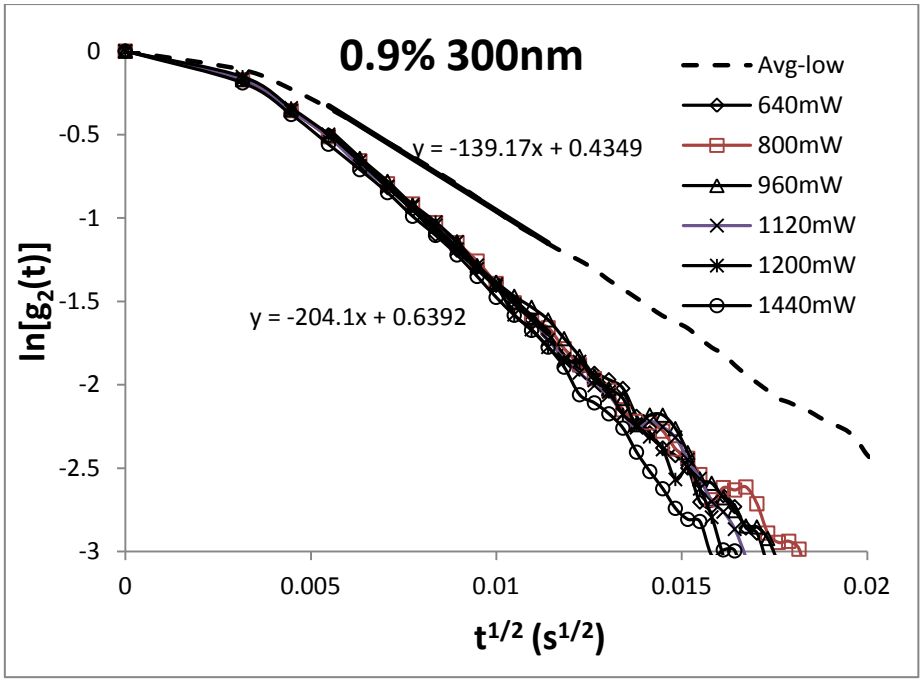

(a)

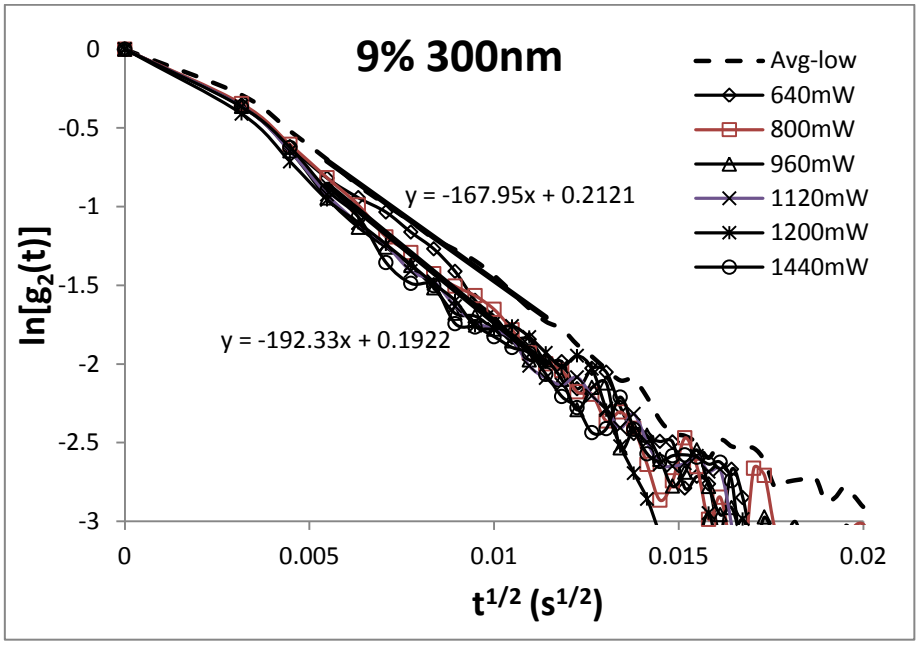

(b)

Figure 5.6 Comparing the normalised $g_2(t)$ of 0.9% and 9% volume fraction for 300nm suspension in the low laser power band (40mW to 320mW) and high laser power band (640mW to 1440mW), log plotting against $t^{1/2}$ shows more than 58% and more than 15% difference in the slopes, respectively.

The influence of later power on DWS particle sizing is shown in Figure 5.7. This figure reveals how high power band and low laser band affect the value of slope S, and finally the particle size determination. The following formula

$$\frac{S}{210} = 1 - 0.66\phi \tag{5.2}$$

is used to describe the linear relation between slope S and the volume fraction ϕ. It confirms that for high concentration, the slope is slightly changed under high laser power, but the alternation is small. Therefore, the laser effect in high band can be ignored. In low laser band, however the influence cannot be expressed by a single function, and a turning point at approximate 3.8% volume fraction exists. When concentration is lower than this value, the measured slopes increase with concentration increasing. If the concentration is higher than this value, the opposite trend is obtained. Apparently, it is found from the graph that under low band, the slope S is underestimated, and as a result the particle size might be overestimated.

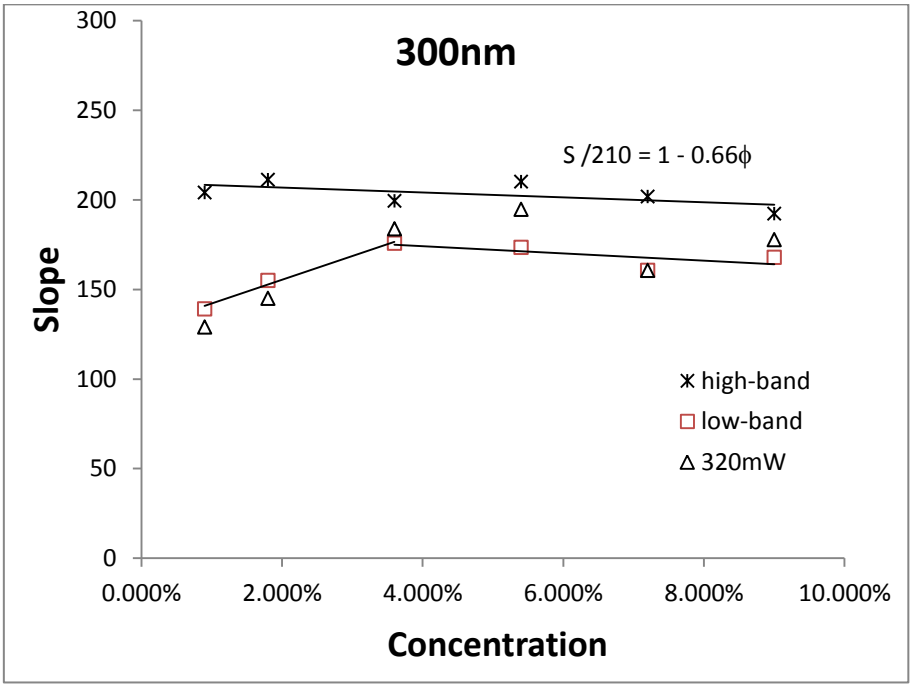

Figure 5.7 Slopes of DWS autocorrelation functions $\ln\left[g_2(t)\right]$ against $t^{1/2}$ for the 300nm-diameter latex particle with the volume fraction range from 0.9% to 9% (1% to 10% concentration by weight) under high band, low band and 320mW laser power respectively.

5.5 Conclusions

From the above analysis, first, it is confirmed that the laser power indeed has influence on DWS and particle size measurement. Then, it can be concluded that the high band with a power above 640mW is reliable for DWS particle sizing, while the low band with laser power below 320mW is proved to be insufficient to work as light source to illuminate the sample cell. As such, it is unable to get an accurate result. Further analysis for low band reveals that how the low laser band affects the particle size determination; that is, when the laser power decreases, the decay rates of $g_2(t)$ reduce. The decrease of decay rates leads to an increase of the slopes of the logarithm plotting, thereby resulting in an overestimated particle size. However, the laser power influence could be partly reduced by normalizing the autocorrelation function. After the normalization, the autocorrelation functions decay from 1 to 0.

Comparison of the autocorrelation function and logarithm plotting between the high band laser and normalized low band laser indicates that the onset of laser power influence is shifted from high laser power to low laser power when the solution gets increasingly concentrated. It means that the increase of solution concentration largely reduces the DWS system's dependence on high laser power. Even an insufficient laser power input, DWS system might still generate an accurate particle sizing result for concentrated particle solution.

Furthermore, the formula, $S/210 = 1 - 0.66\phi$, is found to be able describe the impact of laser power under high laser band. As such, it can be concluded that for high concentration, the slope is slightly changed under high laser power but the alternation is small. Therefore, the laser effect in high band is insignificant. However, the influence in low band could not be eliminated. The slopes vary with the concentration; the reliability of the measurement at low band power is still an open question.

5.6 Summary

In this chapter, the laser power effect was systematically investigated. From previous studies by other researchers, it could be known that the laser radiation will induce local heating, as a result change the refractive index. Hence, the particle size will be distorted under some conditions. In this work, it is confirmed that laser power input has a significant influence on

the result of particle sizing. By analysing the autocorrelation functions and logarithm plotting against time square, the laser power is categorized into two groups. The first is the range from 40mW to 320mW, and the other is the range from 640mW to 1140mW. For a given particle solution, when high laser band is used, identical autocorrelation functions are found; however when low band is applied, the function curves are different from each other, and the decay rate increases with laser power. This confirms that the high laser band is reliable for particle sizing, and the low band is insufficient. From the graph describing the relationship between slope and concentration for low band and high band, it is concluded that the resultant particle size is overestimated when using low power band. For high laser band, although the slope demonstrated a slightly decrease when the solution concentration increases, the influence is small and can be ignored.

Chapter 6
Effect of Suspension Concentration on Particle Sizing

6.1 Introduction

Besides the laser power effect, the concentration of solution also has impact on the DWS performance which will influence the autocorrelation functions as well. DWS investigates the particle's properties in different mediums, such as solution, gel, aerosol, in which the particle's scattering motion is different. When the laser light traverses in the medium, the amplitude and phase is modulated due to the particle's scattering which is characterized by the transport mean free path l^* of the photon. While, l^* which described the typical step length of photon random walk was affected by the particle's properties and the particle's concentration[121]. Therefore, the study of the effect of particle's concentration on DWS is necessary. This chapter will systematically investigate the impact on particle size measurement with a wide range of particle concentrations.

6.2 Previous Studies

6.2.1 Particle Diffusion Coefficient

A number of researches have been conducted to investigate feasibility of the DWS technique for different particle concentration, as well as the effect of concentration on autocorrelation function and particle size analysis.

Lloyd et al. and Pusey et al. investigated the concentration effect, and found that the dependence came from the particle's interaction which was a function of the time scale [122, 123]. Lloyd et al. reported that for low concentration suspension, the measured particle size by DWS decreased as the concentration increased; the effect of the concentration was noticeable from very low concentration and up to approximate 15% volume fraction, and

noticeably significant for solution less than 10%[122]. Similarly, other researches have revealed that the effect of concentration was due to the interactions between particles. The primary type of the interaction is hydrodynamic forces. When a particle moves in a suspension, it will hydraulically influence particles nearby. This hydrodynamic impact will reduce the mobility of the particle, leading to a decrease in its diffusivity. Wiese et al.[124] have noted that the decrease of particle mobility was reflected as the increase of the relaxation time; and it could be expressed as the change of particle's self-diffusion coefficient.

Two parameters, D_0 and D_{eff}, were introduced by Qiu et al.[125], where D_0 is the free-particle diffusion coefficient which denotes the self-diffusion of a particle in suspension, and D_{eff} is the effective diffusion coefficient that describes particle diffusion in the presence of both structural and hydrodynamic effects. For diluted and non-interactive systems, the free diffusion coefficient is given by the Stoke-Einstein relation as shown in Equation(4.17). According to Puesy et al., the effective diffusion coefficient could be expressed in a relation to the free-diffusion coefficient as following[123]

$$D_{eff}(q) = D_0 \frac{H(q)}{S(q)} \tag{6.1}$$

where q is the wave factor, $S(q)$ is the static-structure factor depending on the surrounding material, $H(q)$ is a function to express the effect of the hydrodynamic interactions between the particles.

The hydrodynamic effect has been studied theoretically by two groups. The first is Beenakker et al. who used many-body interactions to find the mobility tensor and then normalized the Einstein relation to get $H(q)$ [126, 127]. The second is Snook et al. who calculated $H(q)$ from a two-body mobility tensor using the effective-medium theory[128]. Both group found that $H(q)$ was less than 1 no matter what the concentration was because the relaxation of concentration fluctuation slowed down due to hydrodynamic interactions[129]. Therefore, the effective-diffusion coefficient was always small than the free-diffusion coefficient.

Apart from these, Horne et al.[114] suggested that the hydrodynamic effect could also be investigated using the solvent viscosity. When the particles existed in a solution, the viscosity

of the suspension was changed, and the viscosity in the Stoke-Einstein equation should be replaced by the actual viscosity η_s. They predicted that the particle mobility or the relaxation time was proportional to the real viscosity of the suspension and the particle size. Therefore, the viscosity of suspension was measured with different concentration. It presented that the dependence of concentration on viscosity could be expressed as a function of the dilution factor. This agreed with what Batchelor suggested as Equation(4.19).

Previous studies have revealed that the diffusion coefficient of spherical particles in suspension was concentration dependent. A number of theoretical formulas have been proposed to describe the concentration effect assuming the particles are spheres. A popular format is

$$D_{eff} / D_0 = A + B\phi + C\phi^2 \tag{6.2}$$

where A, B and C are constants, ϕ is the volume fraction. In this formula, when $\phi \to 0$, $D_{eff} = D_0$. Therefore A=1 has been assumed as a default value in most studies. Bachelor[107] suggested A=1, B=-1.83 and C=0, and the factor $(1-1.83\phi)$ represented the reduction in the changing rate of the mean-square displacement of a particle. Felderhof[130] gave another expression with A=1, B=-1.73 and C=0. Felderh further pointed out that the difference between his result and Bachelor's was from the numerical integration of the exact result for hydrodynamic two-body problem. However, Beenakker et al.[131] found that the two-sphere hydrodynamic interactions were not sufficient to describe the properties of suspension with high volume fraction by taking account of the three-body contribution; they suggested a second order approximation, which gave A=1, B=-1.73 and C=0.88. Later, they included many-body interactions and further investigated the density dependency of the short-time, collective diffusion coefficient, concluding that the effective diffusivity D_{eff} was reduced as concentration increased; when $\phi = 0.5$, the ratio D_{eff} / D_0 drops below 0.4[127]. For concentration in the range of $0.03 < \phi < 0.45$, Qiu et al.[125] run some experiments using polystyrene spheres with size of 0.412 and 0.913 μm. In their experiment, the particles were cleaned by ion-exchange, and HCl was added to reduce the screening length. They obtained A=1, B= $-(1.83 \pm 0.07)$ and C=0.88. Xue et al.[129] also experimentally investigated the particles with diameter d>2μm, and found A=1, B= $-(1.77 \pm 0.07)$ and C=0.

A number of researches have been done in attempts to find the concentration effect both theoretically and experimentally; the results were comparable, although a small difference existed between them. Based on available studies, Scheffold summarised them to following general formula[40]

$$D_{eff} / D_0 = 1 - 1.83\phi + 0.88\phi^2 \tag{6.3}$$

which was widely accepted.

On the other hand, for low concentration suspension, Bachelor[107] has found that the greater availability of particle site enhanced the particle diffusivity, and this enhancement was probably more significant than hydrodynamic effect, which reduced the diffusivity. Therefore, a theoretical formula has been derived to describe the diffusivity due to Brownian motion in a diluted suspension of rigid spheres[107]

$$D_{eff} / D_0 = 1 + 1.45\phi \tag{6.4}$$

The researches discussed above were established based on the assumption that the particles were hard-particles (or rigid spheres) and impenetrable, so they did not overlap with each other. In practical applications, however, most particles in a solution might not be hard-particles. Moreover, the ways to obtain hard particles are not routine methods which may change the properties of solution. For example, adding HCl to reduce the screening length cannot be allowed in most biological studies. Therefore, this may limit the application of DWS measurement for concentrated suspensions in industry.

6.2.2 Particle Sizing for Concentrated Solution

Because of hydrodynamic effect and Brownian motion, particle sizing for particle solutions with different concentration is a challenge.

Navabpour et al.[44], using DWS technique, analysed the particle size of a number of suspensions with polymer latex particles with a diameter in the range from 90 nm to 1300nm; the concentration changed from 2% and 18% in volume. They found that when the size of the particles was the same, the decay rates of the autocorrelation function increased with concentration. Interestingly, they also found that the decay rates decreased with particle size increasing even the concentration was kept the same. This is due to: an increase in concentration led to an increase in viscosity and scattering efficiency; as a result, the decay

rate increased. However, under the same concentration, larger particles moved slowly, which resulted in a slow decay of the correlation function. Apart from this, they also suggested that the autocorrelation decay time continuously reduced for high concentration suspension until it approached a limiting value.

Scheffold[40] also investigated the concentration effect in DWS. He analyzed the concentration influence due to hydrodynamic effect. He found that high concentration solution which meant the strong particles interactions led to deviations for the measured correlation functions, and this deviation made particle sizing complicated. When the volume fraction approached $\phi = 20\%$, the measured particle size increased to 1.4 times of the true value. However, he concluded that in principle, DWS is a good method for particle sizing for particles with a diameter in the range from 100nm to 3000nm, for volume fraction concentration up to at least 10-20%.

6.2.3 Particle Sizing for Diluted Solution

On the opposite of concentrated suspension, dilute suspensions have been traditionally assumed to be with no problem. In real application, research for particle suspension with concentration below 0.1% is necessary. For example, in water engineering, in order to measure the water turbidity, the particle concentrations could be very low to be measured by Nephelometric Turbidity Units (NTU). However, there is not so much quantitative information available to show DWS method for very low concentration solution. Therefore, in this work, DWS for very low concentration was also investigated.

6.3 Experimental Methods

Similar to laser power tests, the polystyrene latex beads with diameter of 300nm, 820nm and 1100nm were prepared. A variety of concentrations were obtained, 0.1%, 0.2%, 0.4%, 0.6%, 0.8%, 1%, 2%, 4%, 6%, 8% and 10% in weight, correspondingly, 0.09%, 0.18%, 0.36%, 0.54%, 0.72%, 0.9%, 1.8%, 3.6%, 5.4%, 7.2% and 9% in volume. For low concentration tests, the latex beads solution stock was diluted to a low concentration range from 0.0001% to 1% in weight, 0.00009% to 0.9% in volume. After that, the diluted solution was injected into 1x1x50mm^3 sample cell.

In laser power tests, the laser power at or above 640mW were regarded as an appropriate laser input. For the concentration tests, a moderate laser power 640mW was chosen. Experiment was conducted on the same experimental set-up as laser power tests. Every particle solution with different volume fraction was investigated. For each sample, a number of 1572864 pictures were taken in a short period of time. All the particle images were then processed by the programme, followed by analysis to gain an insight into the influence of concentration on DWS.

6.4 Results and Discussion

The same as previous studies, it is confirmed that particles interaction affects the autocorrelation function. The analysis from experiment data demonstrates that for a specific volume fraction concentration, the decay rate decreases as the particle size increases shown in Figure 6.1. This is because that the particle with larger size has a stronger power to drag adjacent particles than that of small particle; as a result, the particle diffusivity is reduced compared to that of small particles. In addition, Brownian motion is also believed to contribute to the particle diffusion. So, when particle size increases, the strength of Brownian motion gets weak, so does the diffusivity which leads to a slow decay as shown in Figure 6.1.

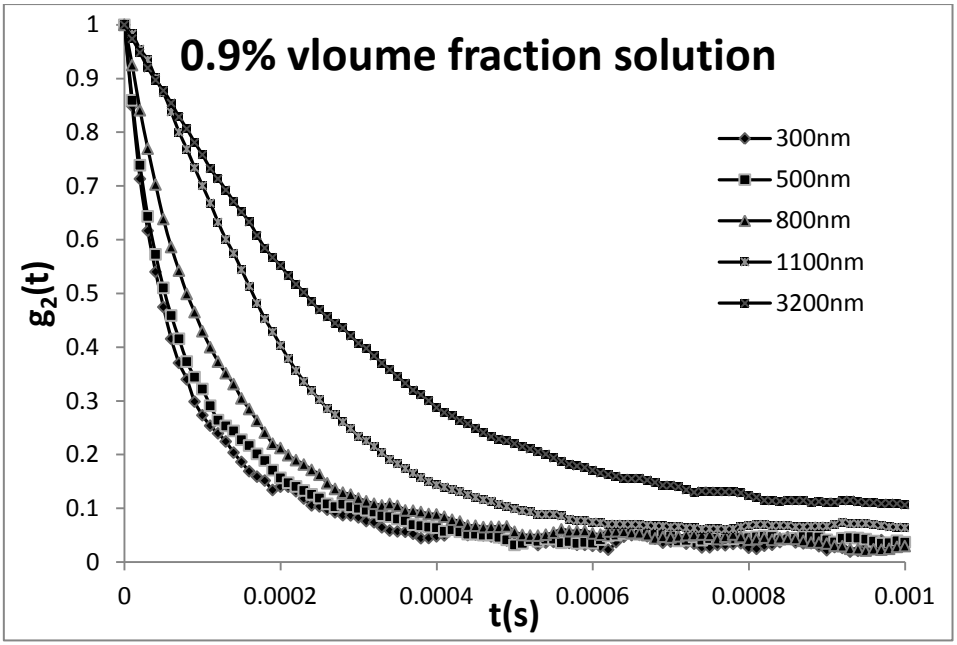

Figure 6.1 When the concentration is a constant, the decay rate of $g_2(t)$ deceased with particle size increase.

Figure 6.2 displays the decay times of the autocorrelation functions as a function of particle diameter at different concentration. It is apparent that the decay time reduces with particle size decreasing on the same concentration level; and the decay time reduces with the concentration increasing for the same particle size.

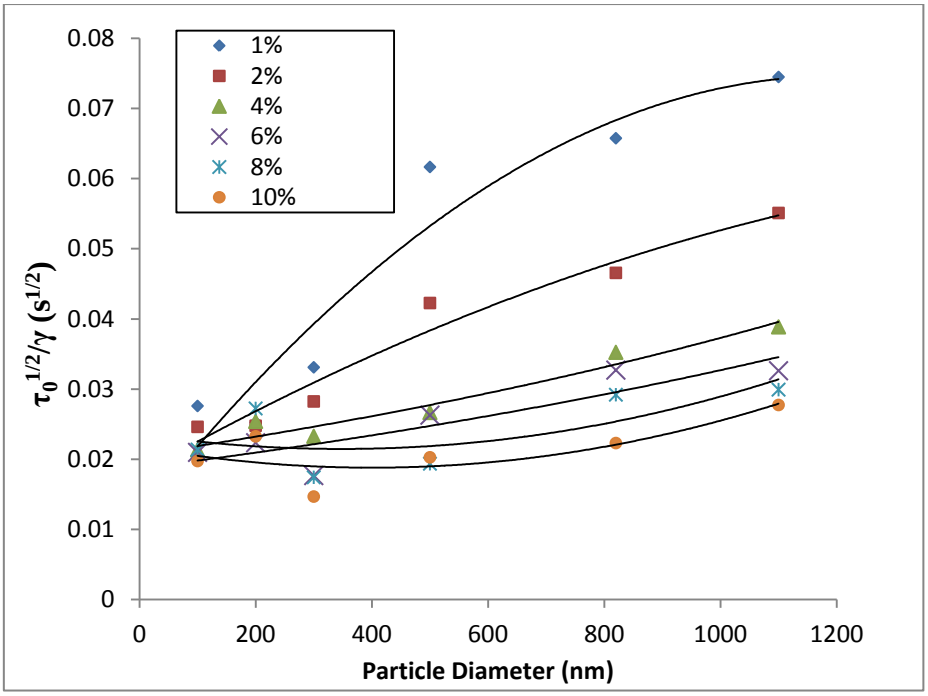

Figure 6.2 The decay times of the autocorrelation functions as a function of particle diameter at volume fraction 0.9%, 0.18%,0.36%, 0.54%, 0.72% and 0.9% (1%, 2%, 4%, 6%, 8% and 10% in weight).

Figure 6.3 displays the autocorrelation functions for 300nm-diameter particle solution with volume fraction concentration from 0.09% to 9%(0.1% to 10% in weight). Figure 6.3 (a) shows the increase of the decay rate for a higher volume fraction, which is consistent with the results of Navabpour [44]. This figure also shows that some functions do not decay to 0 when the decay time tends to be infinite. A similar normalization was performed based on Equation(5.1). The curves after normalization were demonstrated in Figure 6.3 (b).

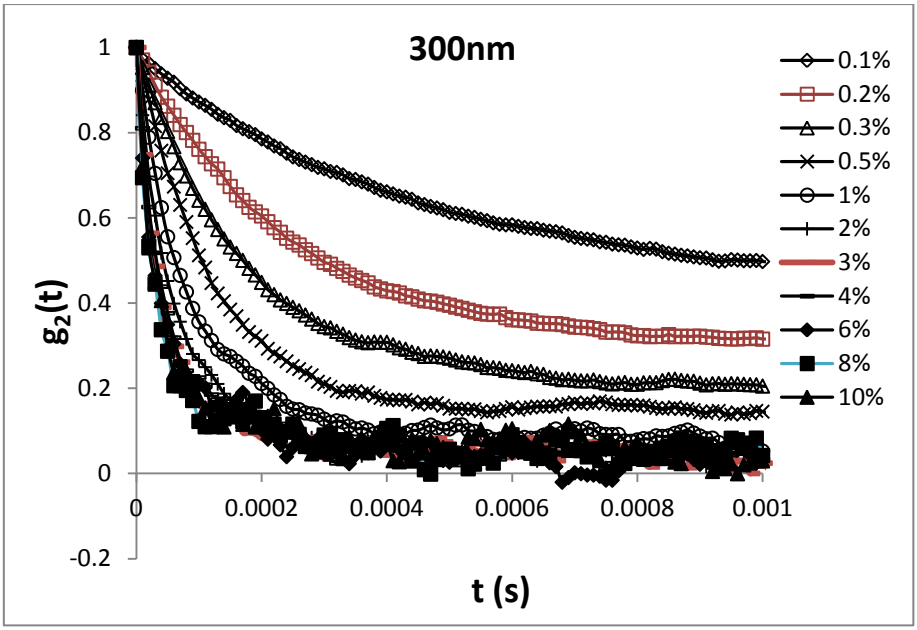

(a)

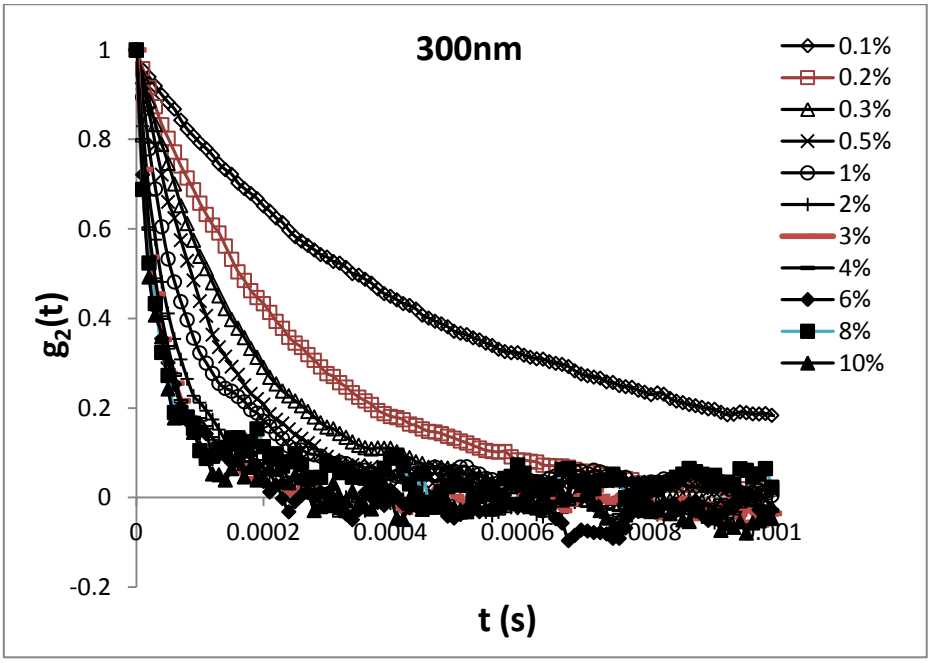

(b)

Figure 6.3 DWS autocorrelation functions for the 300nm latex particles with volume fractions from 0.09% to 9% (0.1% to 10% concentration in weight): a) autocorrelation functions $g_2(t)$; b) normalised $g_2(t)$ covering the full range between 0 and 1.

As discussed before, the effective-diffusion coefficient was related to free-diffusion coefficient as shown in Equation(6.1). According to the research of Qiu et al. this formula can also be defined as[125]

$$D_{eff} = D_0 H(\infty) \tag{6.5}$$

When the effect of hydrodynamic interaction was taken into account for concentrated suspension, Weitz et al. modified the field autocorrelation function G_1 from Equation(2.1) to[87]

$$G_1(\tau) = \int_0^\infty P(s) \exp\left[-(2\tau/\tau_0)(s/l^*)(D_{eff}/D_0)\right] ds \tag{6.6}$$

So, Equation(4.16) was changed to

$$\boldsymbol{S} = -2\gamma\sqrt{(6/\tau_0)(D_{eff}/D_0)} \tag{6.7}$$

Defining

$$C = \frac{4\gamma^2 K_B T k^2}{\pi\eta} \tag{6.8}$$

the following formula was derived

$$\frac{D_{eff}}{D_0} = \frac{S^2 d}{2C} \tag{6.9}$$

where S is the slope of the logarithm plotting against time square, d is the particle diameter. Obviously, the slope S is the only variable in this equation.

Figure 6.4 plots $S\sqrt{d}$ against the concentration ϕ. It reveals that the concentration does influence the value of S, thereby affecting the particle sizing result. From the volume fraction 0.9% to 9% (1% to 10% in weight), the relation between concentration and slope can be expressed in a linear function

$$y/100 = 1 - 1.83x \tag{6.10}$$

where x denoted the solution concentration, y denoted the value of $S\sqrt{d}$. From Equation(6.9), it was noted that $S^2 d$ could be replaced by D_{eff}/D_0, and Equation(6.10) could be changed to

$$\frac{D_{eff}}{D_0} = 1 - 1.83\phi \tag{6.11}$$

The equation denoted A=1, B=-1.83, C=0 which agrees with previous study. However, in this figure, some of the data points for 1100nm-diameter particles with low concentrations are not in line with the equation. This is probably that Brownian motion dose not have an obvious influence to particles with big size, therefore, the diffusivity is more effective.

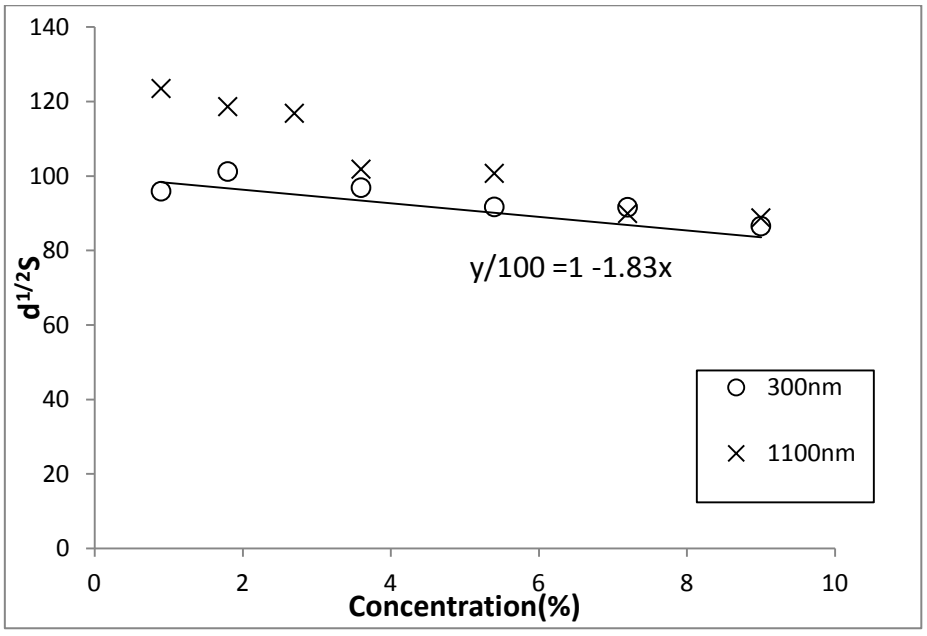

(a)

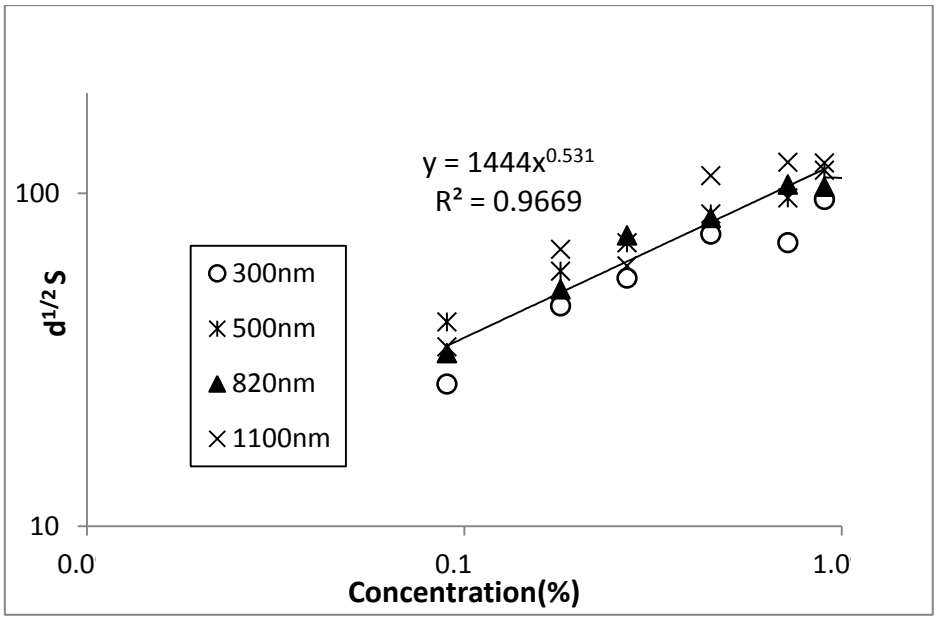

(b)

Figure 6.4 Variation of slope S in the range of 0.09% to 9% volume fractions (0.1% to 10% concentration by weight) in a 1 by 1mm channel: a) the effects of concentration on S are in line with previous theory; b). A function is used to describe the variations.

However, for a low volume fraction ranging from 0.09% to 0.9% (0.1% to 1% in weight), the influence was different from that for high concentration solution. It was represented as an exponential function as following

$$y = 1444x^{0.531} \tag{6.12}$$

Substituting x and y, the following equation was obtained

$$D_{eff}/D_0 = 14\phi^{0.531} \tag{6.13}$$

Therefore, the particle sizing method for particle solutions with different concentration can be summarized as following:

1) When the volume fraction is in the range of 0.9% - 9%, the relationship between D_{eff}/D_0 and ϕ agrees with the previous study, that is, $D_{eff}/D_0 = 1-1.83\phi$. According to Equation (6.8), the particle sizing formula is given

$$R = \frac{16\gamma^2 n^2 \pi K_B T}{S^2 \lambda^2 \eta_S} \times \frac{D_{eff}}{D_0} \tag{6.14}$$

For the concentrated solution, it can be changed to

$$R = \frac{16\gamma^2 n^2 \pi K_B T}{S^2 \lambda^2 \eta_0} \times \frac{(1-1.83\phi)}{(1+2.5\phi)} \tag{6.15}$$

From the equation above, the concentration effect could be minimized.

2) When the volume fraction is in the range of 0.09% - 0.9%. The following relation was derived from this research: $D_{eff}/D_0 = 14\phi^{0.531}$. Therefore, the formula of particle sizing is expressed as

$$R = \frac{224\gamma^2 n^2 \pi K_B T}{S^2 \lambda^2 \eta_0} \times \frac{\phi^{0.531}}{(1+2.5\phi)} \tag{6.16}$$

This equation shows that the influence of concentration decreases when volume fraction increases and the results could be acceptable.

Table 6.1 and Table 6.2 show the particle sizing results by using the formula above in which d is the real particle size, ϕ is the volume fraction of solution, S is the slope, d_{DWS} is the measured particle size, ε is the error which indicates the deviation of the measured particle size from the real particle size. The results confirmed that Equation (6.16) and Equation (6.17) can be used to characterise particle size under various volume fraction range.

Table 6.1 The particle sizing results for concentrated solution with a volume fraction in the range of 0.9% - 9%.

d (m)	ϕ	S	d_{DWS} (m)	ε
1E-07	0.009	348.2979417	1.02E-07	2%
3E-07	0.072	169.6434705	3.14E-07	4.6%
5E-07	0.036	142.9963673	5.18E-07	3.6%
8.2E-07	0.090	105.3048075	7.8E-07	4.8%
1.1E-06	0.018	102.8150599	10.82E-06	1.6%

Table 6.2 The particle sizing results for concentrated solution with a volume fraction in the range of 0.09% - 0.9%.

d (m)	ϕ	S	d_{DWS} (m)	ε
1E-07	0.009	365.2320446	1.04E-07	4%
3E-07	0.072	171.0156076	3.09E-07	3%
5E-07	0.036	238.416843	4.78E-07	4.4%
8.2E-07	0.090	213.8454098	8.6E-07	4.9%
1.1E-06	0.018	131.1686641	1.14E-06	3.6%

Very low concentration tests were conducted after the study of concentration effect. Figure 6.5 shows the normalized autocorrelation functions for the volume fraction ranging from 0.9% to 0.009% (1% to 0.01% in weight). It indicates that from volume fraction of 0.054% (0.06%

in weight) to 1% (0.9% in weight), the curves can decay from 1 to approximately 0. However, when the solution was more diluted with a volume fraction below 0.009% (0.01% in weight), the shape of curves change (see Figure 6.6). The curves with a volume fraction below 0.0036% are not as smooth as that in Figure 6.5, and some fluctuations can be found, indicating that the autocorrelation function dose not decay exponentially. Therefore, Equation (2.1) for particle sizing breaks down for solution with the very low volume fraction range.

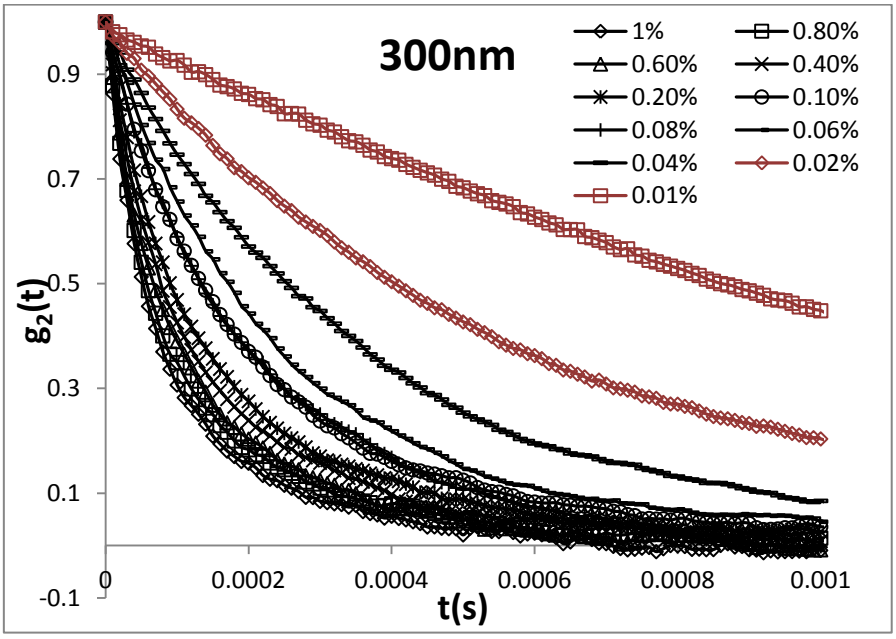

Figure 6.5 Normalised DWS autocorrelation functions $g_2(t)$ for 300nm latexes particle with volume fraction from 0.009 to 0.9% (0.01% to 1%in weight).

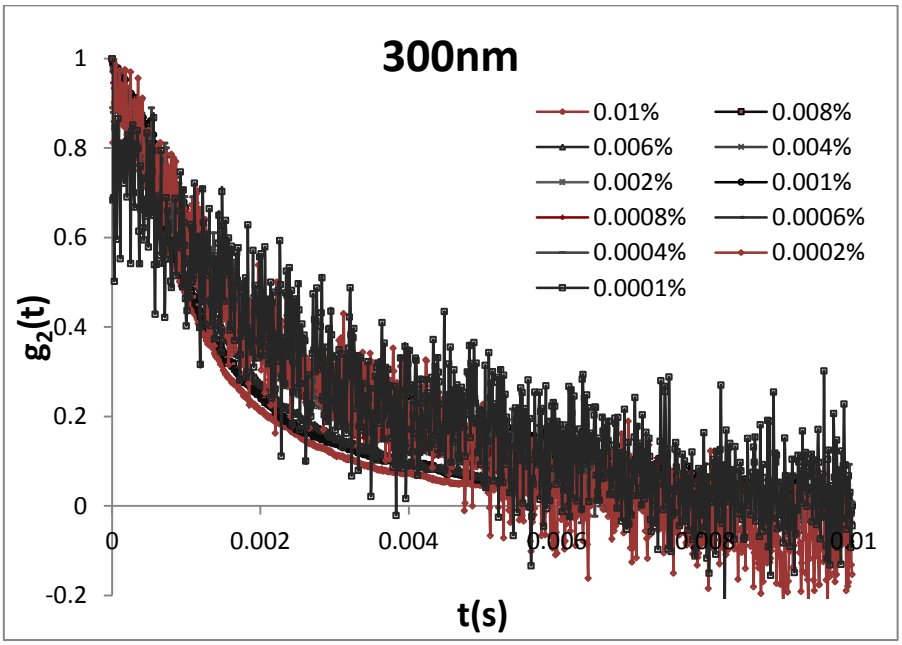

Figure 6.6 Normalised DWS autocorrelation functions $g_2(t)$ for 300nm particle with concentration from 0.0001% to 0.01%.

Hence, it might be concluded that by using the experimental set-up in this work, particle size can be determined for particles suspensions with a volume fraction above 0.054% (0.06% in weight). The exponential decay autocorrelation function is invalid for solution with a volume fraction below 0.0036% (0.004% in weight).

6.5 Conclusions

From the above analysis, it confirms that particle's concentration indeed has influence on DWS and particle size measurement. The concentration effect shows in three aspects. First, for a given concentration, the decay rate of the autocorrelation function decreases as the particle size increases due to hydrodynamic interaction and Brownian motion. When particle size increases, the hydrodynamic interaction and Brownian reduce the mobility of the particles. The decreasing mobility results in a decrease in particle diffusion, which leads to a reduction in decay rate. Second, it is found that the decay rate of the autocorrelation function is concentration dependent. Generally, the decay of the autocorrelation function is fast for high volume fraction, especially in the range from 0.1% to 1%. Third, mathematical formulas are developed to describe the concentration effect. The dependence between D_{eff}/D_0 and volume fraction ϕ is $D_{eff}/D_0 = 14\phi^{0.531}$ for solution concentration from 0.09% to 0.9%; and $D_{eff}/D_0 = 1-1.83\phi$ for solution with a high volume fraction from 0.9% to 9%. For the diluted solution, it is obvious that a decreased particle size is obtained when concentration slightly increases. For concentrated solution, a slightly increase in particle size is measured as the concentration increased. However, the concentration effect could be minimized in the particle sizing measurement by using two different formulas. For the volume fraction in the range 0.9%-9%, $R = \frac{16\gamma^2 n^2 \pi K_B T}{S^2 \lambda^2 \eta_0} \times \frac{1-1.83\phi}{1+2.5\phi}$ is used; while when the solution is diluted to a volume fraction ranging from 0.09% to 0.9%, using $R = \frac{224\gamma^2 n^2 \pi K_B T}{S^2 \lambda^2 \eta_0} \times \frac{\phi^{0.531}}{1+2.5\phi}$ is the proper method to get an accurate result. Besides, for very low concentration solution, it can be concluded that, by using the experimental set-up in this work, DWS is a good method to measure particle size in solution with a volume fraction above 0.054% (0.06% in weight). It

might be not valid for solution with a volume fraction below 0.0036% (0.004% in weight). Between these two thresholds, particle sizing by DWS is still an open question.

6.6 Summary

In this chapter, the concentration influence was systematically investigated. From previous studies by other researchers, it can be known that the concentration effect comes from the particles interaction. In this work, the autocorrelation function is confirmed concentration dependent due to hydrodynamic interaction between particles. Hydrodynamic interaction reduces the particle's diffusion. Generally, the decay rate of the autocorrelation function increases when the volume fraction increases. Particularly, for high concentration solution, the relation between the ratio of effective-diffusion coefficient and free-diffusion coefficient and the volume fraction is consistent with previous study, but for low particle concentration, a new formula is developed to describe the concentration effect on the diffusion coefficient ratio. Based on the relation between the diffusion coefficient ratio and the volume fraction, the particle sizing equations are changed. In addition, the very low concentration tests give a result, showing that there is a threshold of volume fraction below which the DWS might break down for particle sizing.

Chapter 7

Particle Sizing in Shear Flow

7.1 Introduction

In previous chapters, the autocorrelation function of DWS technique was investigated under different laser powers and different concentrations. The experiment was conducted in static condition, where the fluid did not move; the particles were suspended in solution and subjected to only Brownian motion. Under this condition, DWS was proved to be a reliable method to measure particle size. However, in practice, the fluid might not be static but flows under a driving force, imposing shear force to the particles. In fact, particles under dynamic movement are interested in many fields, such as aggregation and break-up of photocatalyst particles in a Couette flow system, the bubble dynamics in continuously sheared aqueous foam, and the coagulation of hydrosols. In shear flow, the particle's movement is not only subjected to Brownian motion, but also shear strain. Therefore, the random light scattering in the medium will be affected, which might lead to a significant change in the autocorrelation function, and hence the particle sizing.

In order to apply it to dynamic systems, such as foam system, sol-gel systems and flow systems, we extended DWS to a medium with spatially localized flow of scatters. In this medium, the light was transmitted by flow, and the intensity fluctuation signal was collected under a collective physical effect of Brownian motion and shear rate.

7.2 Previous Studies

7.2.1 Particle's Brownian motion

The starting point of the study of Brownian motion was in 1827, when a botanist Robert Brown from Scotland discovered that the pollen grains randomly moved under the observation of microscope[132]. Nowadays, the name of Brownian motion which denotes particle's random movement is widely accepted by the people. Brownian motion is a

continuous-time irregular process in which the position of particles cannot be predicted. It is important for particles with diameter smaller than 1000nm[133], and it is always present, regardless whether the shear flow exists or not[134]. In Brownian motion, the particle motion is considered as "ballistic" in a short time, while it is regarded as diffusive in long times[86]; the interaction between particles and surrounding fluid is the key point to determine the transition from ballistic to diffusive motion[135]. Brownian movements that are executed by individual particles increase the diffusivity of the bulk suspension. As discussed in previous chapters, the effective diffusivity produced by Brownian movement was expressed in the form of particle free-diffusion, and it was characterized by the free-diffusion coefficient D_0 .The coefficient was derived from Stokes-Einstein relation and was displayed as Equation(4.17). Figure 7.1 displays the particle pictures under the image field of microscope, which were taken in a sequence with small time intervals. These pictures reveal the particle's random "diffusive" motion.

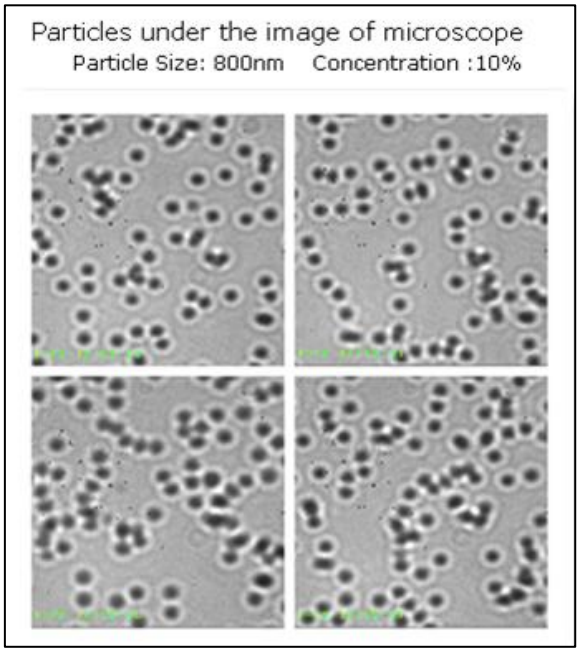

Figure 7.1 Pictures of Polystyrene particles taken in sequence under the image field of microscope .

7.2.2 Particle's motion in Shear Flow

Shear flow happens when fluid moves at low velocity and in the laminar stage. Laminar flow will turn to turbulent as the velocity increases. The dimensionless Reynolds number is often used to determine whether a flow is in laminar range or turbulent range.

In a laminar flow, a force gradient exists in the fluid. Due to viscous dragging and friction, fluid near the solid boundary is nearly static. Therefore, a velocity gradient is formed, giving rise to shear strain. Under the shear train, the particle movement changes and its trajectory alters. It was found that when subjected to a simple shear flow, the particle moved along a closed orbit that was determined by the initial condition[136]. Tehrani found that the particles formed a string-like structure along the flow direction due to the high shear strain in a visco-elastic suspension[137]. However, Won et al. found that, after a long time shearing, the particles remained almost evenly distributed in the fluid[138]. Under shear strain, the particle became more active. The shear stress was the second mechanism that contributes to the increase in the collision frequency[133]. When the collision frequency was increased, the particle's aggregation and disaggregation were both affected; the rate of particle's aggregation and disaggregation depended on the shear rate[139].

7.2.3 Light Scattering under Brownian Motion and Shear Strain

When the light is multiple-scattered by a concentrated medium under shear strain, the scatters are subjected to a shear flow and Brownian motion. There are two dynamic processes that should be considered in DWS when measuring the autocorrelation functions.

As presented in previous chapter, the intensity of the autocorrelation function, $g_2(t)$, of a multiple scattered light is related to the motion of the scatters as shown in the following equation[140]

$$g_2(t) = |g_1(t)|^2 + 1 = \left(\int_0^\infty P(s) \exp\left(-\frac{1}{3} X(t) \frac{s}{l^*} \right) \right) + 1 \tag{7.1}$$

where $X(t)$ describes the average contribution of a moving scatter to the dephasing of a light path. It is dependent of the motion of the scatter, if only considering the Brownian motion, the term can be written as [108]

$$X(t) = 6t / \tau_0 \tag{7.2}$$

where τ_0 is defined in Equation(2.2).

According to Wu et al., for pure Brownian motion, the square of Brownian particle displacement $\langle \triangle r^2(\tau) \rangle$ is proportional to time, τ_B, which is the characteristic time scale representing Brownian motion. Similarly, τ_B can be expressed as

$$\tau_B^{-1} = D_0 k_0^2 \tag{7.3}$$

Therefore,

$$X(t) = 6t/\tau_B \tag{7.4}$$

In laminar flow, the displacement of particle is also influenced by shear rate, Wu et al. suggested that the deterministic motion $\left\langle \Delta r(\tau)^2 \right\rangle$ was proportional to τ_S^2. In this case[108]

$$X(t) = 6(t/\tau_S)^2 \tag{7.5}$$

where τ_S is defined as the shear relaxation time. Bicout et al. presented[141]

$$\tau_S = \frac{\sqrt{30}}{k_0 l^* \Gamma} \tag{7.6}$$

where Γ is the macroscopically applied shear rate.

There are two independent time scales for $g_1(t)$ in laminar flow, τ_B for Brownian motion and τ_S for convective shear flow[45]. When the shear rate dose not exist, $g_1(t)$ decays exponentially at a rate of $\exp(-2t/\tau_B)$ for pure diffusive process. When the Brownian motion is insignificant, a Gaussian decay applies in which $g_1(t)$ decays at $\exp\left[-2(t/\tau_S)^2\right]$. When particle's movement is subjected to both Brownian motion and shear strain, the following equation was propose[45]

$$X(t) = 6t/\tau_B + 6(t/\tau_S)^2 \tag{7.7}$$

That is, when the characteristic decay time $t \ll \tau_S^2/\tau_B$, Brownian motion is dominant, when $t \gg \tau_S^2/\tau_B$, particle's movement is dominated by shear strain.

7.2.4 Experimental Studies of Shear Flow Effect

Some researchers have investigated the autocorrelation function and the particle size measurement when particles are subjected to shear strain in fluid.

DWS was used to study the influence of shear flow on particle aggregation and break-up. For example, Ruis et al used DWS to investigate the effect of shear flow on the acidification of a

sodium caseinate-stabilized emulsion[140]. The shear rates of 0.005, 0.01, 0.1, 1 or 10 s^{-1} were applied in their experiment. They found that for pH in a certain range, the photon-transport mean free path l^* was not influenced by the shear flow rate. However, under some pH values, it was affected by the shear rate, and the autocorrelation function could not decay to 0. In addition, they have found that the decay time decreased with shear rate increasing, and the autocorrelation function curves changed from the usual near exponential shape to a more Gaussian shape. The process of gas bubble flowing under a shear rate in aqueous foam was called "melting" by Gopal et al.[108]. In their research, DWS was used to probe the response of the bubble to the shear strain. After a wide range of shear strain rates was used on the foam system, they found that the decay rate of the autocorrelation function was significantly affected by the shear strain.

DWS was also employed to determine the position of dynamic fluid region and the velocity of the particles. Skipetrove et al.[41] researched the medium in a cylindrical capillary tube which was subjected to spatially localized flow. They found for different types of motion (Brownian motion, laminar low, and turbulent flow), the autocorrelation functions were extremely different. In addition, they found that the experimental results for flow velocity agreed with theoretical results. Therefore, they concluded that DWS had the ability to determine the position and size of the flow region, and to measure the scatter velocity in these regions. Later, Skipetrove et al.[46] did similar work using a cylinder and found that the decay rate of the function increased with the increasing of shear rate.

The previous study revealed that if the shear strain was introduced into a multiple scattering medium, the mobility of the particle would be enhanced; then the autocorrelation function of the scattering light would change. The change of the correlation was dependent on the particle motion, and was often expressed as different decay time scales. Through the time scale, the researchers experimentally obtained the relationship between particle dynamic properties and shear rate; furthermore, the flow region and scatter velocity were determined. However, no research result has been presented in the form of specific formulas to show the flow effect by using the characteristic time scales of both Brownian motion and shear flow, and to determine the particle size according to the flow regions. This project aims to fill this gap.

7.3 Experimental Methods

A series of shear flow experiments were carried out. Polystyrene micro/nanoparticle solutions with particle size 60nm, 100nm, 300nm, 500nm, 820nm, 1100nm and 3200nm were used in the experiment. The solution stock was diluted by distilled water to produce a concentration of 0.9% in volume fraction. After the dilution, solution was well stirred; and sample cells with dimensions of 1x1x50mm^3, 3x3x360mm^3, 3x6x360mm^3 and 6x6x360mm^3 were used. The cross-sectional area of the flow cells was small enough compared to their length to ensure laminar flow. The sample cells were fixed on an optical platform. By adjusting the height of the platform, the incident point of laser beam was ensured to be in the middle of the flow channel. A syringe pump with a flow rate control console was applied to inject the latex beads solution into the flow channel. The flow rate can change from 0.001ml/m to 10ml/m. In order to obtain close flow velocity, the small flow rates were used for channels with small size, the large flow rates for channels with large size.

The Argon Ion laser was set at wavelength of $\lambda = 488nm$ and 960mW power output. The laser beam was expanded to a spot with diameter approximately 1.5mm. CCD camera was set at start-trigger mode and the frame rate at 100000fps. Pictures were saved at the BMP format with the resolution 128x32 pixels. For each experiment, 1572864 pictures were taken in a short period of time. Then, all of the particles were processed, followed by a further analysis to investigate the influence of shear strain on the particles.

7.4 Results and Discussion

Table 7.1 shows the mean flow velocities for each flow cell. Table 7.2 shows the associated Reynolds Number calculated from

$$\mathrm{Re} = \frac{\rho V_{\max} a}{\mu} \tag{7.8}$$

where ρ is the fluid density (kg/m^3), a is the width of the cross-section of the flow cell (m). μ is the dynamic viscosity of the fluid (kg/ms), and it is known as the absolute viscosity η_s. $V_{\max}$ is the maximum velocity in the centre of the flow channel(m/s) calculated by the following formula

$$V_{\max} = 3Q/2ab \tag{7.9}$$

In which Q is the flow rate (m^3/s) and b is the depth of the cross-section of the cell (m). Table 7.2 shows that the maximum Reynolds Number is 257, ensuring laminar flow in all the experiments.

Table 7.1 The mean flow velocity range for each sample cell.

Cross-sectional Area of Flow Channel (mm^2)	1x1		3x3		3x6		6x6	
Flow Rate (ml/min)	0.001	10	0.001	10	0.001	10	0.001	10
Flow Velocity (m/s)	1.67E-05	1.67E-01	1.85E-06	1.85E-02	9.26E-07	9.26E-03	4.63E-07	4.63E-03

Table 7.2 The calculated Reynolds Numbers for each experiment.

Flow Channel (mm^2)	1x1		3x3		3x6		6x6	
a(m)	0.001		0.003		0.006		0.006	
b(m)	0.001		0.003		0.003		0.006	
Q(m^3/s)	1.67E-11	1.67E-07	1.67E-11	1.67E-07	1.67E-11	1.67E-07	1.67E-11	1.67E-07
ρ (kg/m^3)	1050							
μ (kg/ms)	1.02E-03							
V_{max}(m/s)	2.51E-05	0.2505	2.78E-06	2.78E-02	1.39E-06	1.39E-02	6.96E-07	6.96E-03
Re	2.57E-02	2.57E+02	8.56E-03	8.56E+01	8.56E-03	8.56E+01	4.29E-03	4.29E+01

From Landau et al.[142], for a given flow rate Q, the velocity profile across the cell (z direction) was a parabolic. The shear rate can be expressed as a linear function of the horizontal distance z [45]

$$\Gamma(z) = 8V_{\max} z / a^2 \tag{7.10}$$

for $-a/2 < z < a/2$. Based on this formula, a spatially averaged shear rate was given[45]

$$\bar{\Gamma} = \sqrt{\langle \Gamma^2 \rangle} = 3Q / a^2 b \tag{7.11}$$

This equation was used for calculation of the shear rate, and the results are shown in Table 7.3.

Table 7.3 The calculation result of Reynolds Number of minimum and maximum flow rates for each flow cell.

Flow Channel (mm^2)	1x1		3x3		3x6		6x6	
a(m)	0.001		0.003		0.006		0.006	
b(m)	0.001		0.003		0.003		0.006	
Q(m^3/s)	1.67E-11	1.67E-07	1.67E-11	1.67E-07	1.67E-11	1.67E-07	1.67E-11	1.67E-07
Γ(rms)	0.0501	501	0.00186	18.56	0.00046	4.64	0.00023	2.32

In order to investigate the effect of shear flow on particle movement, the autocorrelation functions were studied. Figure 7.2 shows the autocorrelation functions for the flow tests for particle with diameter of 100nm, 300nm, 500nm and 820nm, respectively, flowing in channel with cross-section of 3x3mm^2 under different shear rates. As shown in Figure 7.2, for particle with a constant size, when the flow rate increases, the decay rate of the autocorrelation function increases as well; for particles with different size, the required time for the autocorrelation function to approach 0 is longer for large particles than for the smaller particles; in addition, the shape of the curve are consistent with exponential decay for particles with small size, while for particles with bigger size, the curves show obvious differences between high flow rates and low flow rates.

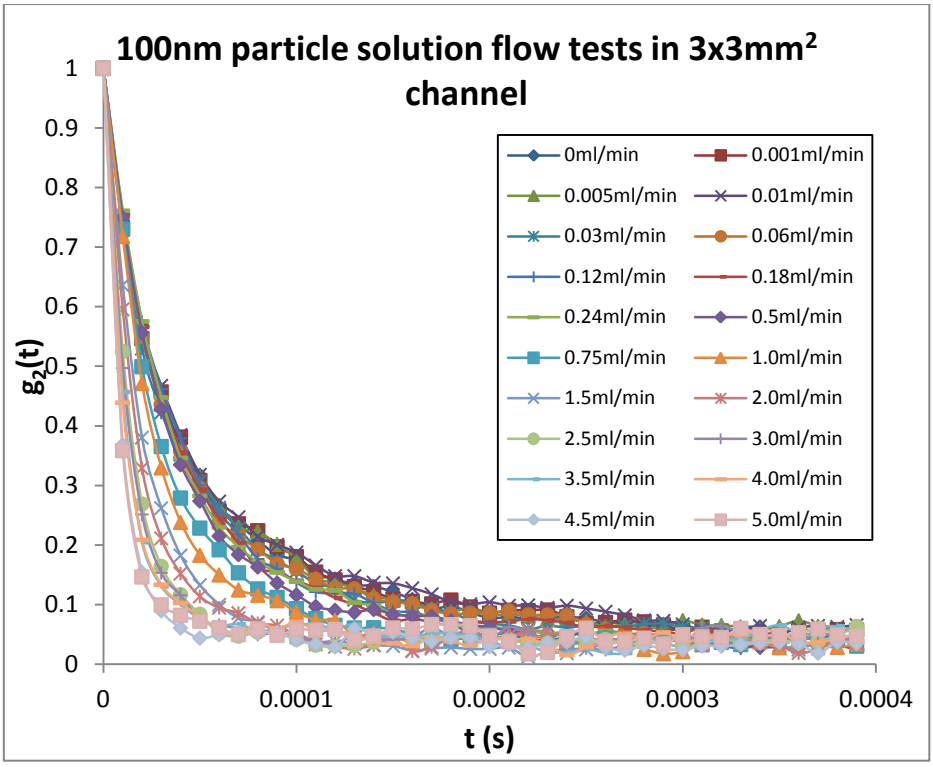
100nm particle solution flow tests in 3x3mm² channel
g₂(t)
t (s)
0
0.1
0.2
0.3
0.4
0.5
0.6
0.7
0.8
0.9
1
0
0.0001
0.0002
0.0003
0.0004
0ml/min
0.001ml/min
0.005ml/min
0.01ml/min
0.03ml/min
0.06ml/min
0.12ml/min
0.18ml/min
0.24ml/min
0.5ml/min
0.75ml/min
1.0ml/min
1.5ml/min
2.0ml/min
2.5ml/min
3.0ml/min
3.5ml/min
4.0ml/min
4.5ml/min
5.0ml/min

(a)

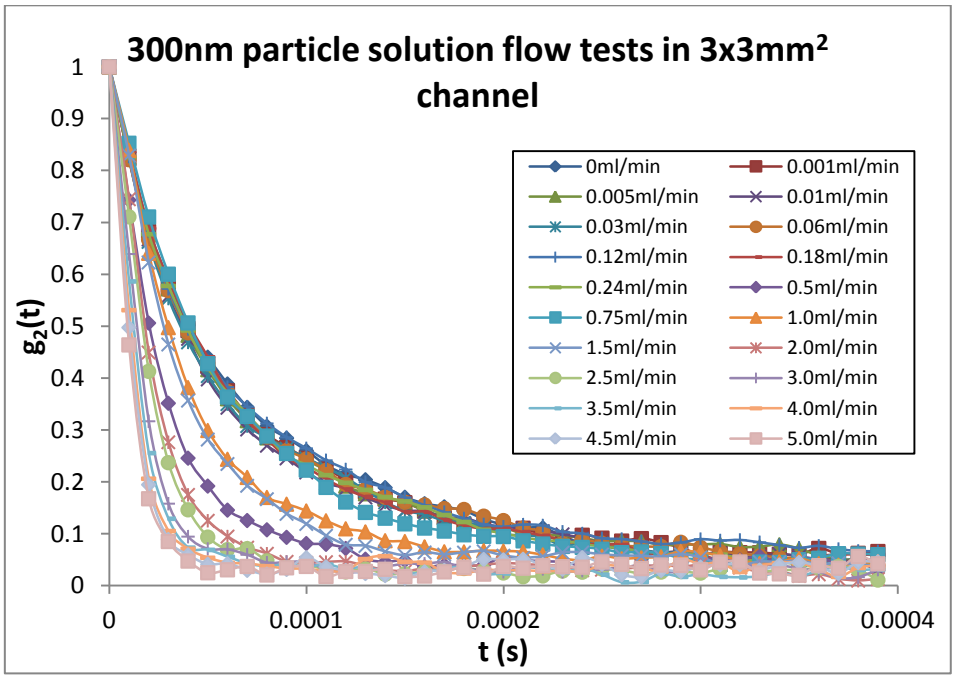
300nm particle solution flow tests in 3x3mm² channel
g₂(t)
t (s)
0
0.1
0.2
0.3
0.4
0.5
0.6
0.7
0.8
0.9
1
0
0.0001
0.0002
0.0003
0.0004
0ml/min
0.001ml/min
0.005ml/min
0.01ml/min
0.03ml/min
0.06ml/min
0.12ml/min
0.18ml/min
0.24ml/min
0.5ml/min
0.75ml/min
1.0ml/min
1.5ml/min
2.0ml/min
2.5ml/min
3.0ml/min
3.5ml/min
4.0ml/min
4.5ml/min
5.0ml/min

(b)

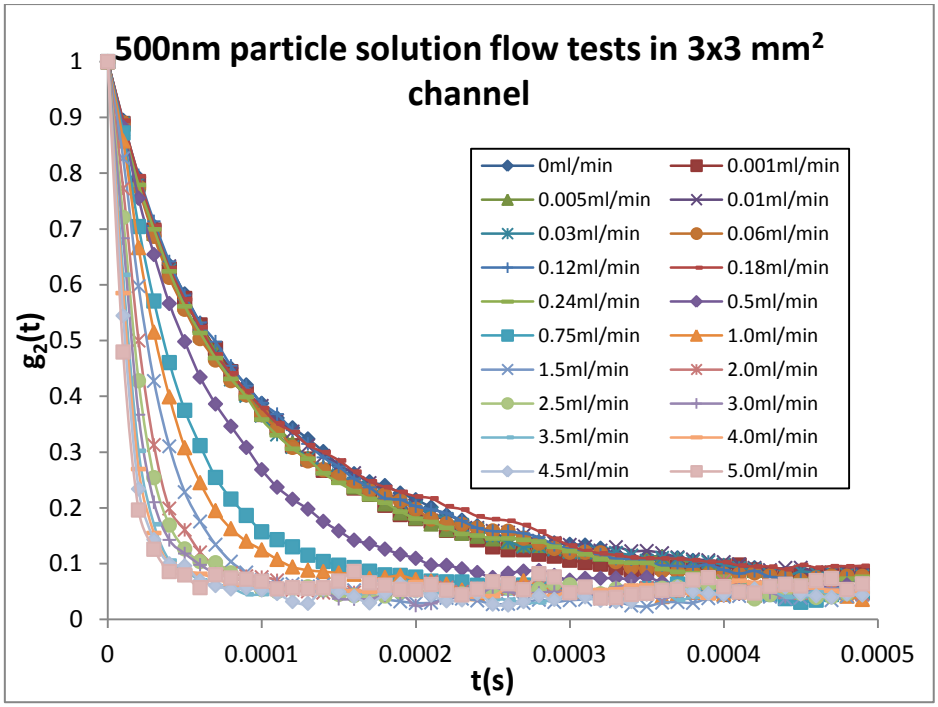

(c)

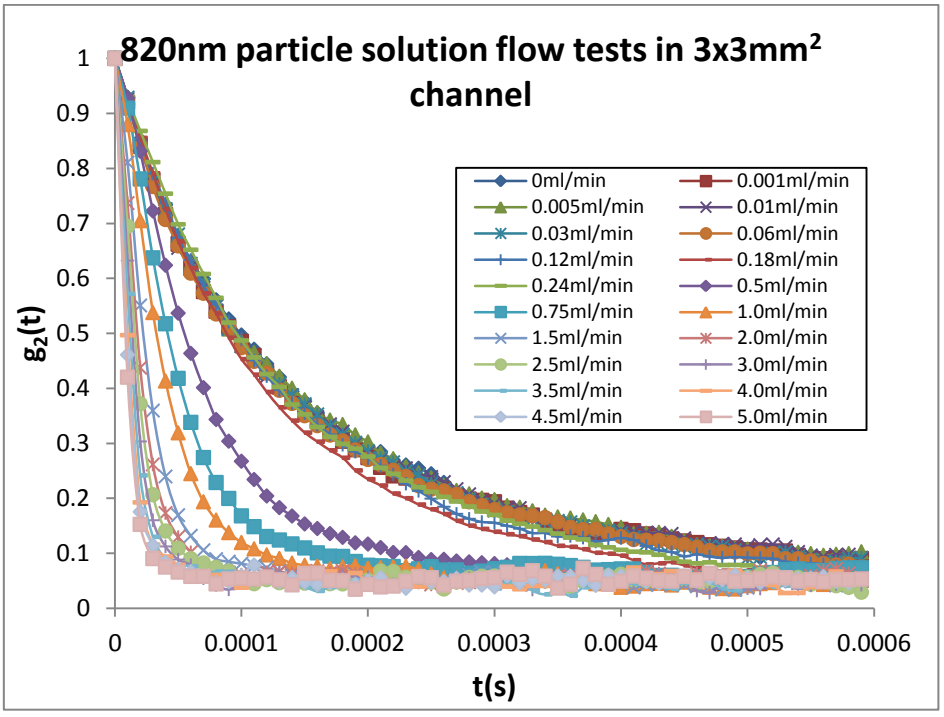

(d)

Figure 7.2 The auto-correlation functions for different particle solutions in 3x3 mm^2 sample channel under various shear flows. The legends denote series of flow rates.

Figure 7.3 (a) shows the autocorrelation functions for 500nm particles with 0.9% volume fraction in the flow cell with cross-section of 3x6mm^2. At low flow rates, the shear rate is

small and the decay of the autocorrelation function is also slow. In contrast, at high flow rates, the shear rate is high and the autocorrelation functions decay fast. Figure 7.3 (b) is the logarithm plotting against time square. It shows how the flow rate affects the curve slope.

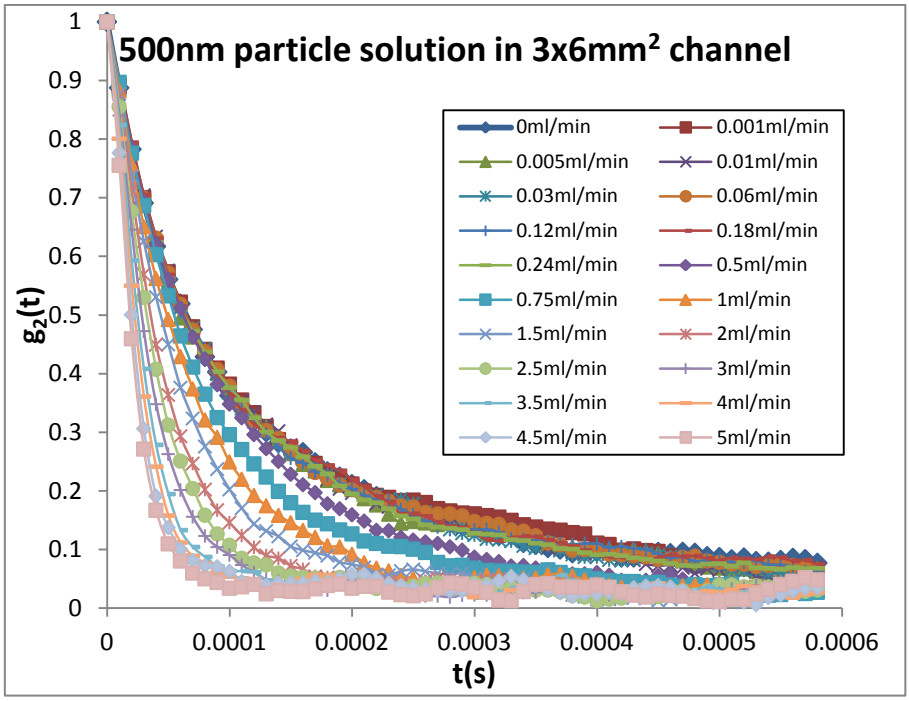

(a)

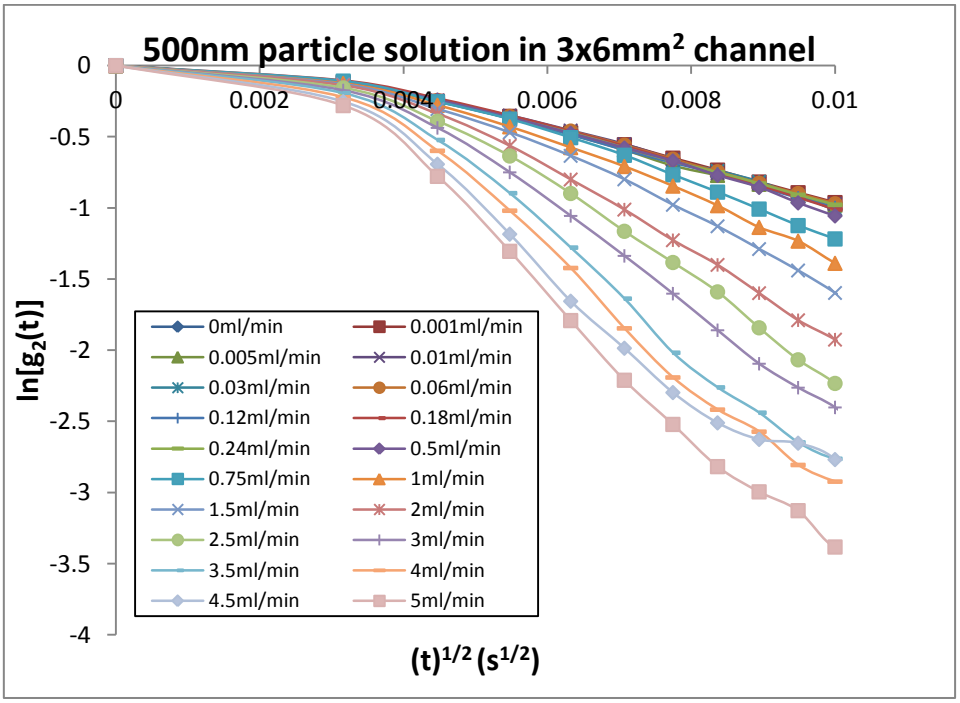

(b)

Figure 7.3 The autocorrelation functions (a) and logarithm plotting against time square (b) for 500nm particles with 0.9% volume fraction in a 3x6mm^2 sample channel under shear stress.

In Figure 7.3 (a), curves with low flow rates superpose and have exponential decay in t; while curves with high flow rates overlap together as well but have fast decay rate that seems like to decay approximately exponential in t^2; but the curves with moderate flow rate are separated and distributed evenly. Hence, it can be noted that the curves are distributed to form three regions. They are high flow rate region, low flow rate region and the transition region; these regions might reflect the influence of Brownian motion and flow effect. To test the idea that the autocorrelation functions can be grouped in three categories, the logarithm plotting against time square was investigated for the data derived from each experiment. For example, for sample cell with a cross-sectional area of 3x3mm^2, first, the logarithm plotting $\ln[g_2(t)]$ against time square $t^{1/2}$ for 100nm-, 300nm-, 500nm-, 800nm- and 3200nm-diameter particles under a wide range of flow rate were completed. Then, for each plotting, a straight line was fitted to get the slop S. It should be noted that the slope S has a unit of s^2 because the y-axis of logarithm plotting is labelled as $t^{1/2}$. After that, the value of slope was extracted and then plotted against flow velocity. Figure 7.4 shows the plotting of slope against flow velocity for 100nm-, 300nm-, 500nm-, 800nm- and 3200nm-diameter particles tests in 3x3mm^2 sample cells.

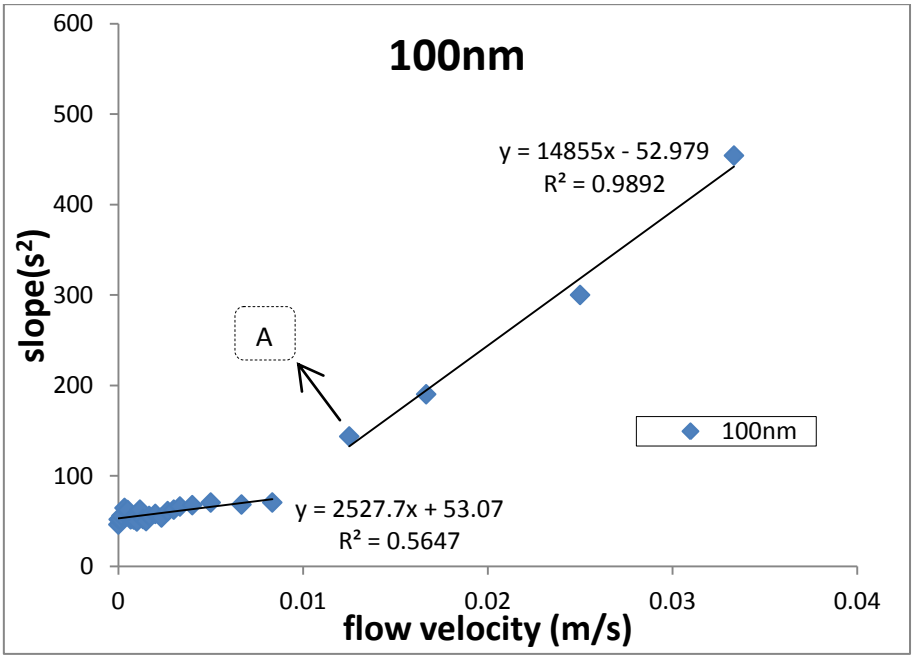

(a)

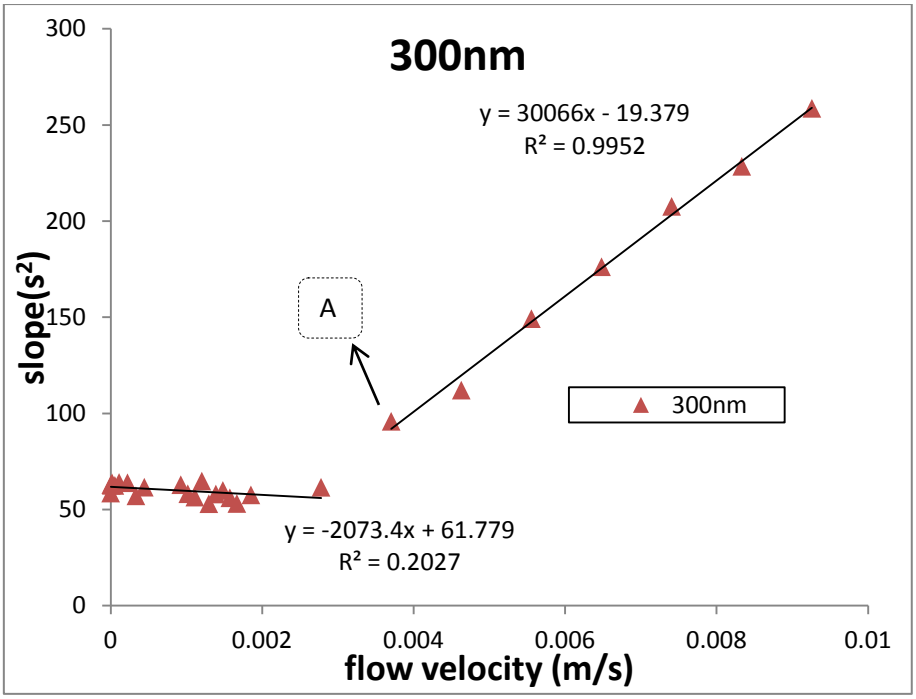
300nm
y = 30066x - 19.379
R² = 0.9952
A
300nm
y = -2073.4x + 61.779
R² = 0.2027
slope(s²)
flow velocity (m/s)
0
50
100
150
200
250
300
0
0.002
0.004
0.006
0.008
0.01

(b)

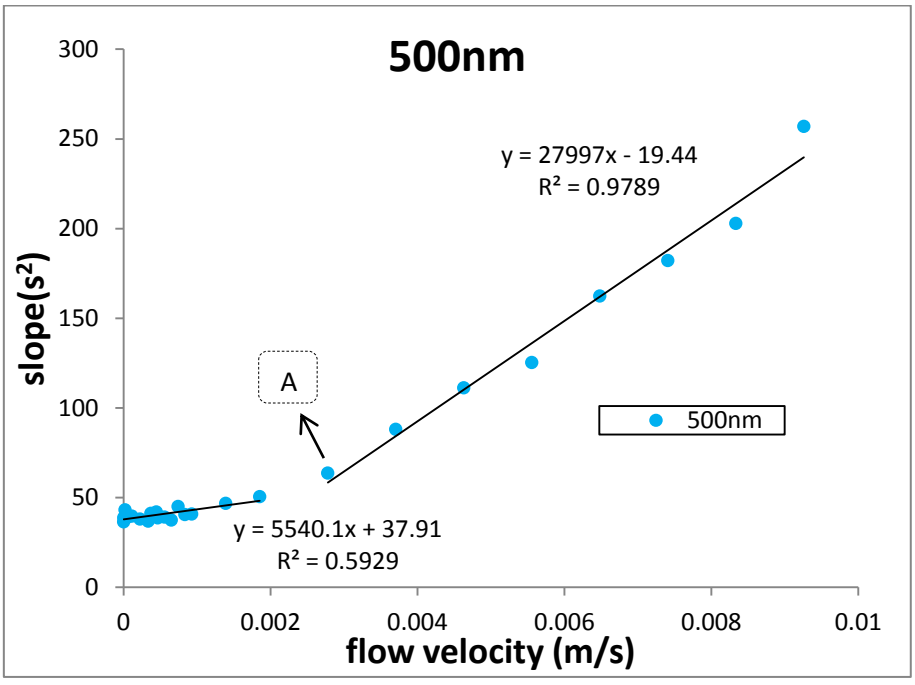
500nm
y = 27997x - 19.44
R² = 0.9789
A
500nm
y = 5540.1x + 37.91
R² = 0.5929
slope(s²)
flow velocity (m/s)
0
50
100
150
200
250
300
0
0.002
0.004
0.006
0.008
0.01

(c)

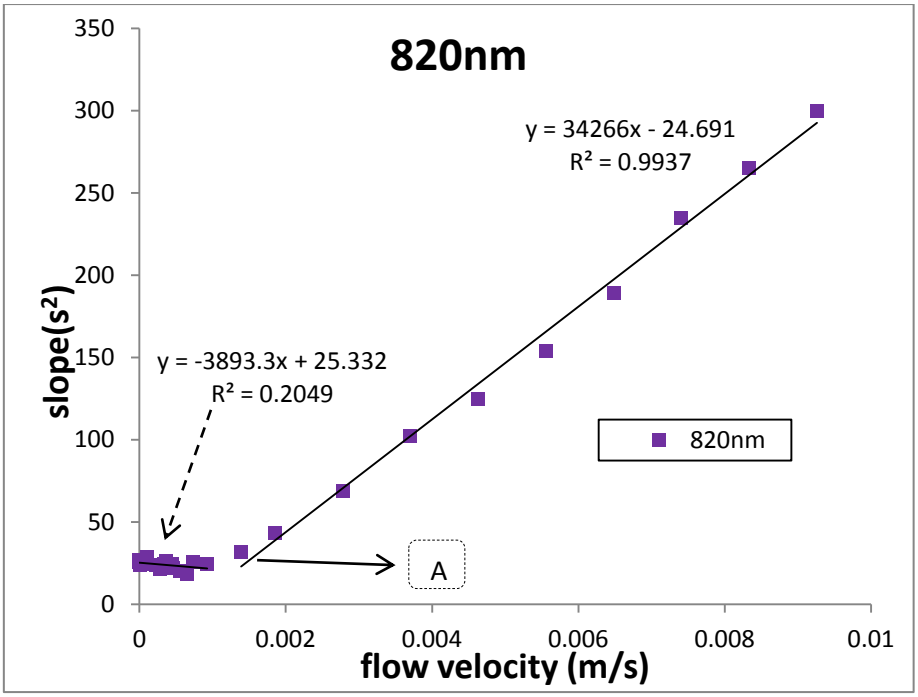

(d)

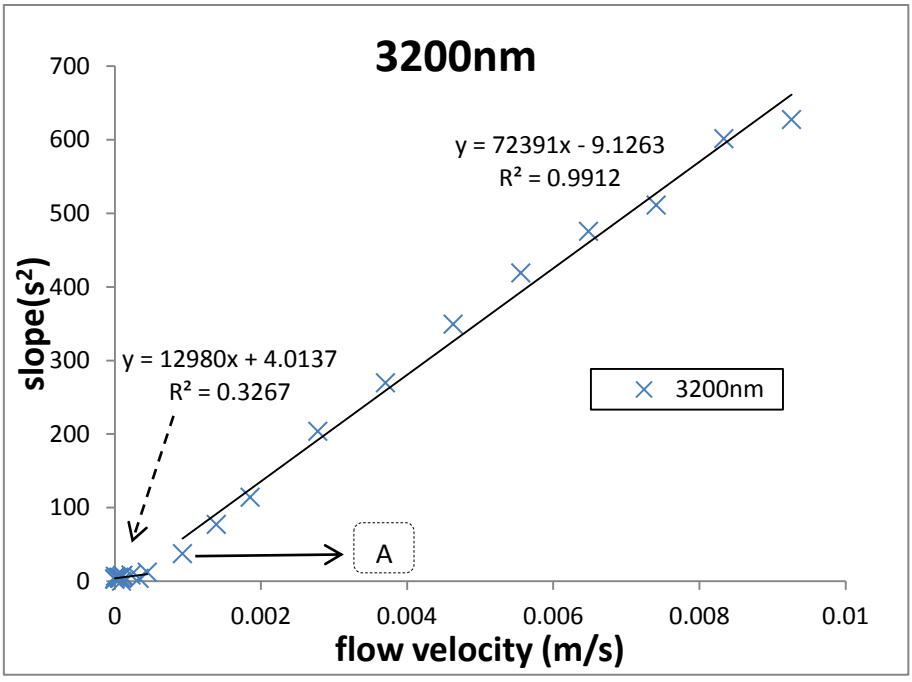

(e)

Figure 7.4 the plotting of slope against flow velocity for (a) 100nm-, (b) 300nm-, (c) 500nm- , (d) 820nm- and (e) 3200nm-diameter particles tests in 3x3mm^2 sample cells.

From Figure 7.4, it is noted that for every graph, the data can be grouped in two categories; for each category, the plotting can be fitted with a straight line. This demonstrates the influence of flow rate: when the flow velocity is low, and the value of slope is small,

indicating a slow decay rate of autocorrelation function; when the flow velocity increases, the value of slope increases, leading to a high decay rate. It can be imaged that at some point, when the flow velocity is low, the particles movement is only dominated by Brownian motion; oppositely, if the flow velocity increases, shear force is sufficient to influence the particle's movement. At that point, particle's motion is dominated by shear strain, and Brownian motion is not significant. Between the two thresholds, particles are in transition region where both of Brownian motion and shear strain have influence on their movement. Therefore, from the graph of slope against flow velocity, the point A is defined as the diving point of a threshold of the flow effect (see Figure 7.4); in addition, for flow velocity below point A, a 20% reduction of slope between two successive points is suggested as the diving point B for another threshold of the flow effect. By using this method, point A and point B for all cases are picked out to establish the dividing lines which describe the domination of Brownian motion or shear strain. After that, the points are properly fitted to describe the low and high boundaries which are shown in Figure 7.5.

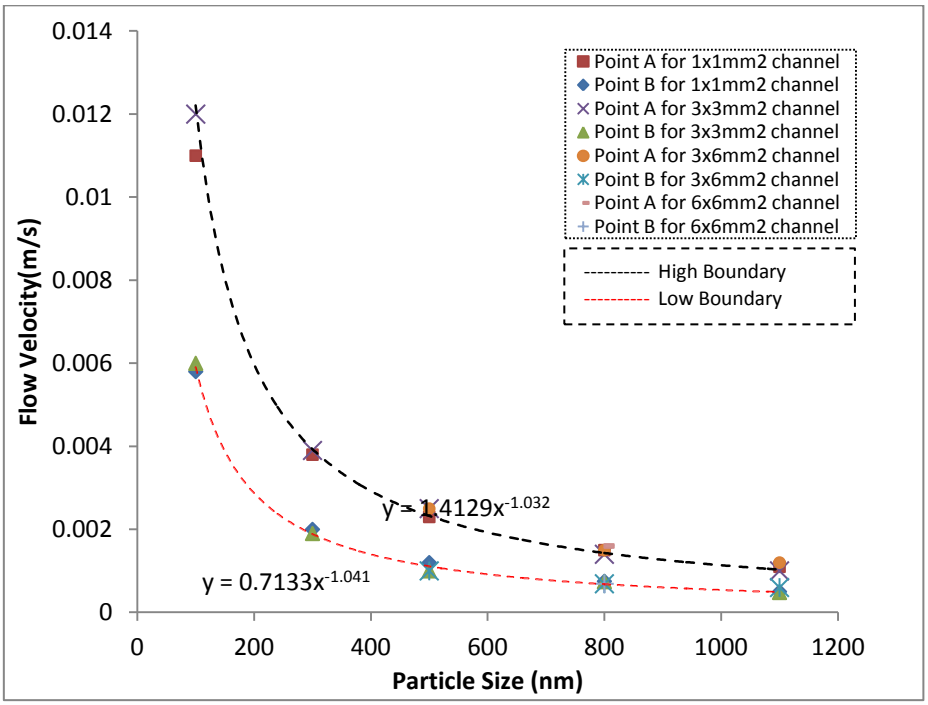

Figure 7.5 The graph shows the low and high boundaries between Brownian and shear flow effects.

It should be noted that in Figure 7.5 the data of particle with 60nm- and 3200nm-dimater are excluded from the data set, only data of 100nm, 300nm, 500nm, 820nm and 1100nm particles

are displayed. In fact, the data for 60nm- and 3200nm-diamter particles are irregular, probably due to the sample solutions which were purchased from Duke Scientific with 1% concentration in weight. They were different from the other solutions which had original 10% concentration and were diluted with distilled water in our lab. Therefore, the dynamic properties of particles may slightly different. In addition, 3200nm-diamter particles had a strong sedimentation due to the large size, leading to the change of autocorrelation functions.

Based on Figure 7.5, by setting the axis to logarithmic scale, straight lines are obtained to describe the three regions which were Brownian motion dominated area, transition area and shear flow dominated area, respectively. This is shown in Figure 7.6. The flow rates which construct the high and low boundaries can be seen in Table 7.4.

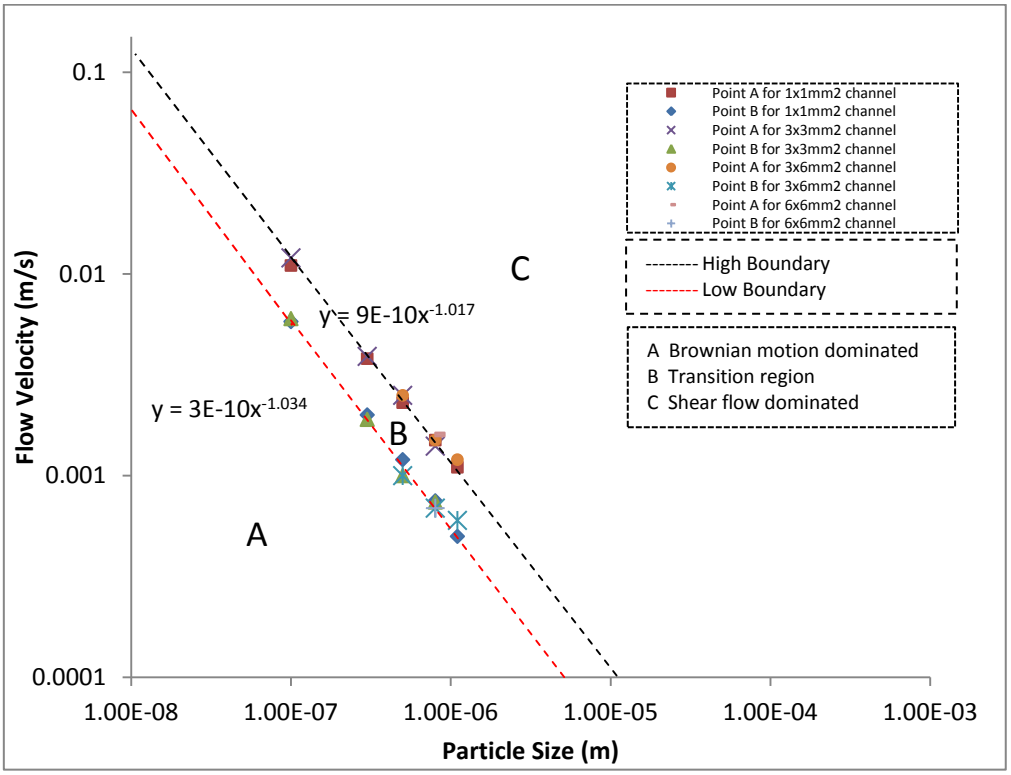

Figure 7.6 The three regions, Brownian motion dominant area A, transition area B and shear flow dominant area C.

Table 7.4 The average value for high and low boundaries.

	size (nm)	100	300	500	820	1100
Flow rate (m/s)	low	0.006	0.002	0.0012	0.0007	0.0005
	high	0.012	0.004	0.0024	0.0015	0.0011

To present the result, a new parameter which is in the format of Peclet Number is introduced here as

$$P_e = \frac{V}{k_0 D_0} \tag{7.12}$$

where V is the flow mean velocity, $k_0 = 2\pi n/\lambda$ is the wave number in the scattering medium, and D_0 describes the diffusivity cause by Brownian motion. Actually, the P_e is directly proportional to a ratio τ_B/τ_S where τ_B is the characteristic time scale representing the Brownian motion and τ_S is the relaxation time scale representing the flow effect. According to Equation(7.3) and Equation(7.6), the value of τ_B/τ_S can be expressed as

$$\frac{\tau_B}{\tau_S} = \frac{l^*\Gamma}{\sqrt{30}k_0 D_0} \tag{7.13}$$

In previous chapters, the definition was given for l^* which was the transport mean free path of photons in medium and could be worked out from Equation (2.4) and Equation (2.5).

$$l^* = \frac{1}{\rho_N \sigma(1-\cos\theta)} \tag{7.14}$$

Akkermans et al. also defined[143]

$$\frac{1}{l^*} = n\int_0^{\pi} \sigma(\theta)(1-\cos\theta)\, d\theta \tag{7.15}$$

where n is the density of the uncorrelated scatters, θ is the scattering angle and $\sigma(\theta)$ is the differential cross-section.

Therefore, the P_e can be changed to

$$P_e = \frac{\sqrt{30}V}{l^*\Gamma} \cdot \frac{\tau_B}{\tau_S} \tag{7.16}$$

By calculating P_e, it was interesting to notice that for all particles, the value of P_e were approximately approach to a constant for both low boundary and high boundary. For low boundary which indicated the onset of the shear flow effects, the average of the constants for all cases is $P_e = 79$, or $\tau_B/\tau_S = 4.88$; for high boundary which indicated the domination of shear force to the particle's movement, the average is $P_e = 159$, or $\tau_B/\tau_S = 9.81$.

As a result, the autocorrelation function for particles under different flow velocity can be presented in three ways:

1) when $\tau_B/\tau_S < 4.88$, particles are under a low flow velocity and only subjected to Brownian motion, $g_1(t)$ decays at a rate of $\exp\left[-2\left(t/\tau_B\right)\right]$. The particle sizing method which is presented in Chapter 4 can be used.

2) when $\tau_B/\tau_S = 9.81$, it means that the shear flow rate increases to a high value that shear flow dominates the particle's motion, $g_1(t)$ decays at a rate of $\exp\left[-2\left(t/\tau_S\right)^2\right]$; according to Equation (7.6), τ_S depends only on the shear rate, because l^* is constant and not affected by the application of shear force. Hence, plotting $\ln\left[g_2(t)-1\right]$ against t still approximately derived a straight line, and Equation(4.16) was changed to

$$S = -2\sqrt{6}\gamma/\tau_S \tag{7.17}$$

Combing Equation(7.6) and Equation (7.17) with above equation gave

$$S = -\frac{2}{\sqrt{5}}\frac{\gamma k_0 \Gamma}{\rho_N \sigma \langle 1-\cos\theta\rangle} \tag{7.18}$$

The total cross-section σ can be approximately calculated by[144]

$$\sigma = \frac{8\pi}{3}\left(\frac{2\pi n}{\lambda}\right)^4\left(\frac{m^2-1}{m^2+1}\right)^2 R^6 \tag{7.19}$$

where $m = n_{particle}/n$ is the ratio of the refractive index of the particle to that of the medium. So the particle sizing equation is

$$R = \left[\frac{3\gamma k_0 \Gamma}{64\sqrt{5} S \rho_N \pi \langle 1-\cos\theta\rangle}\right]^{1/6} \times \left(\frac{\lambda}{\pi n}\right)^{2/3} \times \left(\frac{m^2+1}{m^2-1}\right)^{1/3} \tag{7.20}$$

Therefore, by plotting the logarithm of autocorrelation function against time, getting the straight line slope S and using Equation(7.20) , the particle size is derived.

3) In the transition region where particle's movement is subjected to both of Brownian motion and shear strain, the decay rate is changed to $\exp\left\{-2\left[t/\tau_B+\left(t/\tau_S\right)^2\right]\right\}$. Wu et al.[45] have presented that the autocorrelation function for this region could be simplified to the result obtained for the case without shear rate. Therefore, the same particle sizing method as in 1) can be used.

However, what should be noticed here is that the value of τ_B/τ_S is unknown in the real process of particle sizing, only the flow velocity can be obtained. Due to this, for particle sizing in shear flow, only particle sizing for solution with the flow velocity approximately above 0.2m/s works in real measurement. Because when the flow velocity increased to this value, shear flow would dominate particle's motion, ignoring the particle size (see Figure 7.6).

7.5 Conclusions

It is found that the shear stress would enhance the mobility of the particle and has an influence on the autocorrelation function. First, as the flow rates increases, the decay rate of the autocorrelation function also increases. The required time for the autocorrelation function to approach 0 is longer for large particles than for small particles, due to variation of particle displacements under different shear flows. Second, for smaller particles, the autocorrelation function curves are distributed evenly, while for larger particles, the curves are distributed unevenly, with gaps between particular flow rates. This indicates that the flow influence is significant for large particles than for small particles. Third, it is clear that there are three regions to describe the influence of shear force on the autocorrelation functions. If the flow velocity is low ($P_e<79$ or $\tau_B/\tau_S<4.88$), particles are solely controlled by Brownian motion. Hence, the decay rate of the autocorrelation function is $\exp\left[-2\left(t/\tau_B\right)\right]$, particle size could be generated by using Equation (4.18); when the flow velocity increases to a large value ($P_e>159$ or $\tau_B/\tau_S>9.81$), the particle's movement is dominated by shear flow, and the Brownian effect decreases to an insignificant level. The decay rate of the autocorrelation is $\exp\left[-2\left(t/\tau_S\right)^2\right]$. Correspondingly, the particle sizing formula is changed to Equation(7.20); if there is a moderate flow velocity ($79<P_e<159$), both of Brownian motion and shear flow

have influence on the particles. In this transition region, the autocorrelation function decays $\exp\left\{-2\left[t/\tau_B+\left(t/\tau_S\right)^2\right]\right\}$. Noting that the autocorrelation function could be simplified to that without shear, Equation(4.18) can also be used in the particle size measurement.

7.6 Summary

DWS technique has been frequently used over the past two decades to investigate particles in flow fluids. This chapter investigated the impact of the shear flow in laminar flow range. A CCD-DWS backscattering experiment was set up, and the latex particles was injected into flow cells after dilution. By adjusting the pumping rate, a variety of flow rates was produced to induce different shear rates. The light intensity fluctuation was captured and processed. The results show that the shear stress has an impact on particle's motion when the flow velocity approached a specific value. It influences the decay rate of autocorrelation function; the decay increases significantly with the flow velocity increasing. The characteristic time scales for Brownian motion and shear force are used to describe this influence. $\tau_B/\tau_S=4.88$ indicates the threshold of shear flow effect , while $\tau_B/\tau_S=9.81$ indicates the extinction of Brownian motion effect. Between the two boundaries $4.88<\tau_B/\tau_S<9.81$, particles are under the control of both Brownian motion and shear stress. Therefore, when particle size measurement is carried out, specific formulas should be applied for a particular flow velocity depending on which range τ_B/τ_S is in.

Chapter 8
Conclusions, Discussions, Applications and Future Work

8.1 Conclusions

This thesis provides a systematic study on use of the Diffusing-wave Spectroscope (DWS) to measure particle size in both static and flow conditions.

Micro- and nano-particles have been widely used in many areas, and the nanotechnology develops quickly, in which the determination of particle size is of great interest. However, the quantification of particle size is problematic because descriptive measurements of particle morphology do not exist[58]. Particle's dimension is difficult to defined for particles with irregular shape, even though a number of methods have been proposed, including Feret's diameter, Martin's diameter, the projected area diameter, maximum horizontal intercept and perimeter diameter[60]. Each of the above method gives a specific parameter of the particle size. In practical application, a combination of them might be required to provide a precise quantification of the particle size[58]. For experimentally measuring particle size, a number of methods have been developed, including the optical microscopy, laser diffraction, digital image-based analysis and dynamic light scattering. Among them, the dynamic light scattering method has potential advantages.

Dynamic light scattering (DLS) is a method for particle sizing developed over the last 30 years[40]. It is limited to dilute solution due to the theoretical models used to calculate the particle sizing is valid only in single scattering regimes. In the late 1980s, Diffusing-wave spectroscopy (DWS) was introduced to extend the DLS principles to multiple scattering systems. The same as DLS, DWS measures the temporal autocorrelation function of the scattered light intensity to obtain the characteristics of particles and the dynamic structure of the medium. However, different from conventional DLS, DWS has two approximations[87]: the first is that the propagation of the light through a highly scattering medium is treated as a

diffusive process, and the photons execute random walk after numerous scattering events; the second is that the individual behaviour of the photons can be approximated by an average scattering, and each scattering event contributes to the total scattering. Based on these two approximations, the number of scattering can be determined for each path length. The contribution of an individual path to the total correlation function can be expressed as the sum of the average scattering. Therefore, the temporal autocorrelation function can be written as $G_1(t)=\int_0^\infty P(s)\exp\left[-(2t/\tau_0)(s/l^*)\right]ds$. The normalized intensity autocorrelation has a relationship with $G_1(t)$, i.e., $G_2(t)=1+\left|G_1(t)\right|^2$. Also it can be altered as $G_2(t)-1=\exp\left[-2\gamma(6t/\tau_0)^{1/2}\right]$. Plotting the logarithm of $G_2(t)-1$against the square root of t gives a straight line. Using the slope of the straight line S, the particle radius can be obtained from $S=-2\gamma\sqrt{6/\tau_0}$, $R=\frac{16\gamma^2n^2\pi K_BT}{S^2\lambda^2\eta_s}$, then the particle diameter is $d=\frac{32\gamma^2n^2\pi K_BT}{S^2\lambda^2\eta_s}$. The general error of the particle sizing result is within 5%.

A DWS-CCD backscattering experiment set-up was used in this project. A coherent laser radiation produced by an Argon Ion laser at a wavelength of $\lambda=488nm$ was expanded to a speckle spot with 1.5mm diameter. Latex beads suspension diluted by distilled water was pumped into a sample cell which was fixed on optical platform. The laser light was focused on the sample cell, and was then detected on the same side by a high speed CCD camera after it was scattered from the suspension medium. In the experiment, solutions with various particle sizes and volume fractions were employed. For each experiment, 1572864 pictures with resolution of 128x32 pixels were collected by CCD. Each of the individual CCD array was considered as an independent detector. The data derived from each detector were processed on ensemble averaging to obtain the autocorrelation functions. In all, about 2000 experiments were performed during the project, including system testing, laser power influence study, concentration effect study and shear flow study.

The results reveal that the experimental set-up is reliable and repeatable. The laser power input is found to have a remarkable influence on particle sizing. Investigation of the autocorrelation functions shows that the laser power can be categorized into two ranges, low

band range from 40mw to 320mw, and high band range above 640mw. Under low laser power, the autocorrelation functions decay slowly and cannot change from 1 to 0. That is, using insufficient laser radiation may overestimate the particle size. However, the influence of laser power can be reduced by normalizing the autocorrelation function as $g_2(t) = 1 - \left[1 - G_2(t)\right] / \left[1 - G_2(\infty)\right]$. The normalization makes the autocorrelation functions approaching to 0. The results also show that the autocorrelation function is concentration dependent due to the interactions between particles, especially the hydrodynamic interaction. In multiple scattering regimes, the effective diffusion coefficient is determined by self-diffusion and collective diffusion coefficient, and is related to the volume fraction of the suspension. The experiments find that for volume fraction above 0.9%, the result is consistent with previous study in that $D_{eff} / D_0 = 1 - 1.83\phi$, while for concentration in the range of 0.09%-0.9%, the impact of concentration on the effective diffusion coefficient can be expressed as $D_{eff} / D_0 = 14\phi^{0.531}$;new particle sizing equation are derived: $R = \frac{16\gamma^2 n^2 \pi K_B T}{S^2 \lambda^2 \eta_0} \times \frac{(1 - 1.83\phi)}{(1 + 2.5\phi)}$ and $R = \frac{224\gamma^2 n^2 \pi K_B T}{S^2 \lambda^2 \eta} \times \frac{\phi^{0.531}}{(1 + 2.5\phi)}$, respectively. In addition, it is found that by using the experimental set-up in this work, DWS is a good method to measure particle size in solution with a volume fraction above 0.054% (0.06% in weight), but it is invalid for solution with a volume fraction below 0.0036% (0.004% in weight).

The effect of shear flow on particle sizing was also researched. Generally, when Reynolds number is below 2300, the flow is laminar shear flow. In laminar flow, two independent time scales for $g_1(t)$ were derived, τ_B for Brownian motion and τ_S for shear flow. The results show that the values of the P_e, defined as $P_e = V / k_0 D_0$, is proportional to the ratio τ_B / τ_S. The value of P_e which determines the dominance of the Brownian motion and shear flow is a constant for some specific flow rates. When $P_e < 79$, the autocorrelation is dominated by Brownian motion. In this situation, the formula $R = \frac{16\gamma^2 n^2 \pi K_B T}{S^2 \lambda^2 \eta}$ can be used for particle sizing in flow fluid. When $P_e > 159$, the particles are dominated by shear flow and the Brownian effect decreases to an insignificant level. Therefore, the formula $R = \left[\frac{3\gamma k_0 \Gamma}{64\sqrt{5} S \rho_N \pi \langle 1 - \cos\theta \rangle} \right]^{1/6} \times \left(\frac{\lambda}{\pi n} \right)^{2/3} \times \left(\frac{m^2 + 1}{m^2 - 1} \right)^{1/3}$ should be used to calculate the particle

size instead of the previous one. In the transition region, when $79 < P_e < 159$, both of Brownian motion and shear flow has influence on the particles. Noting that the autocorrelation function can be simplified to that without shear, $R = \frac{16\gamma^2 n^2 \pi K_B T}{S^2 \lambda^2 \eta}$ still can be applied for particle sizing.

8.2 Discussions

DWS was developed 20 years ago[85, 86]. In DWS, the light is scattered by the medium to produce an intensity fluctuation. Investigating the intensity autocorrelation function can obtain the particles dynamic properties, including the particle size, particle distribution etc. The experiment in this work was believed to be a reliable set-up for particle sizing. However, there are still some issues that require a further research.

8.2.1 Particle Sedimentation

Particles sedimentation was encountered in the experiment using the latex beads solutions purchased from Sigma-Aldrich and Duke Scientific. They are polystyrene or polystyrene cross-link composed, mainly contain with latex beads and water with a small amount of surfactant, sodium bicarbonate and potassium sulphate. Surfactant is added to stabilize the suspension. According to the handling and storage guidance, the particles should be stored at room temperature, and can be re-suspended by gentle agitation to return it back to a uniform distribution. For dilution, it is said that deionized water can be used and additional surfactant can be applied when necessary.

In the experiment, the distilled water was used for the dilution due to the difficulty of obtaining deionized water. When the distilled water was used for dilution, some particles settled down during the experiment. In order to reduce such an influence, the following actions were taken. First, in each experiment, the material preparation was completed in time, and the time gap between preparation and experiment was reduced to small to keep the particle evenly distributed. Second, the solution was stirred before pumping it into the flow cell. Third, the samples were discarded after several runs of experiment if any sedimentation was discovered. However, the sedimentation still cannot be avoided. Due to this, there might be some errors of the concentration in the experiment. Therefore, a huge number of experiments were conducted to statistically reduce the errors.

8.2.2 Ensemble Average and Time Average

The high speed CCD used in DWS instead of a single PMT, can be regarded an array of speckles working simultaneously. Therefore, a series of DWS measurement was conducted in the same time with autocorrelation functions derived from each speckle. For each set of data, the correlation functions measured from different pixels with the same scattering vector were processed and assembled. The ensemble average is calculated for a final autocorrelation function.

Besides the ensemble average, time average can also be applied to increase the statistic accuracy. The order of ensemble average or time average can be adjusted. The autocorrelation functions can be averaged over all pixels and then normalized by time, or, in a reverse order[97]. Using time average has an advantage that the data can be collected in parallel and sequentially. Thus, for a given total measurement time, no matter how long the decay time is, the data process is always accessible.

8.2.3 Thermal Effect of Laser

The laser power effect was investigated in this thesis. It was found that for the CCD-DWS backscattering experiment, there were low laser band and high laser band. The high laser band was reliable for measuring particle size, but low band did not provide sufficient illumination. In addition, the measured particle size was laser power dependent.

Although the high laser band is regarded as a safe laser power input for DWS, the associated thermal blooming will affect the result. According to Lin et al.[74] when the laser light was absorbed by the medium, it leads to local heating in the path of the laser beam. The heating causes an alternation of the medium's optical index of refraction, which could result in a divergence of the beam. They also found that at low laser intensity, the autocorrelation function decays exponentially, while when high laser was applied, the curve deviated. As such, the high laser power band has a problem of inducing thermal effect.

In this work, high laser band was considered as a proper laser power input, but the thermal effect was not investigated. It needs a further study.

8.3 Applications

DLS has been applied in research and industry, but DWS is still not a standard method for particle sizing. The objective of this research is to study the DWS under various conditions. The followings are some potential application in environmental engineering.

8.3.1 Turbidity Measurement

The water turbidity is an important parameter of water quality. It is defined as cloudiness or non-transparency caused by small particles in water. In environmental engineering, the total suspended solid (TSS) in water is often considered. The water appears more turbid if the TSS value is high. A high value of turbidity is significant problematic to the water quality which will affect the aquatic organisms. Thus the turbidity is one of the parameters that need to be measured, which can be done using a turbidimeter.

Turbidimeter is an apparatus to examine the turbidity through an expression of optical properties that the light cannot transmit the sample, but is scattered or absorbed. Generally, this expression is delivered in the unit of NTU. The research has found that the particle size, shape, colour and refractive index affect the turbidity measurement, especially the particle size. When the light is scattered forwardly, the particle size could influence the result. Thus, the turbidity measurement by turbidimeter with transmission mode is difficult, and the result varies. To solve the problem, the turbidimeter which detects the scattered light at angle of 90 degree to the incident light was developed; it is noted that the angel is very sensitive to the light scattering; thus sometimes, additional light source is required to measure the scattered light from other angles[145]. Figure 8.1 shows the principle of turbidity measurement.

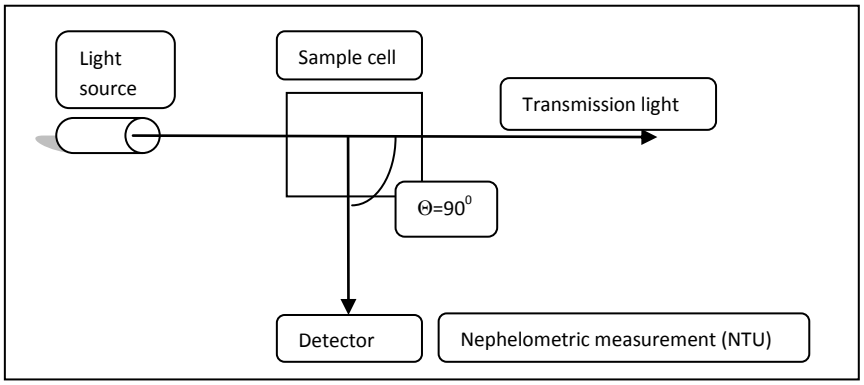

Figure 8.1 The principle of turbidity measurement.

DWS has potential for turbidity measurement and particle sizing. First, backscattering DWS does not depend on the scattered angle. So the angle for detecting the scattered light is not critical in DWS. Second, the conventional trubidimeter only determines water turbidity. In contrast, DWS can not only measure the light scattering, but can also measure the particle size.

8.3.2 Particle Aggregation Investigation

photocatalytic particles aggregate and break up in the reactor. In order to maintain the activity of photocatalyst particles, the concentration and the surface area of the particles should be strictly controlled. As pointed out by Gondal et al.[146], when the photocatalyst was used for conversion of methane into methanol, it was found that if the light source was an intense light, such as laser, optimizing the concentration of the catalyst under the direct illumination was extremely important.

The aggregation and disaggregation of particles are dynamic processes, some of which take place in shear flow. Serra et al.[139] reported that the aggregation rate depended not only on the rate that particles collided each other, but also on the probability of particles cohering after the collision. The disaggregation rate depended on the shear rate which induced the probability of particles splitting after the collision. The final size after aggregation and disaggregation depended on the shear rate and the volume fraction; and the balance between aggregation and break-up depended on that the flow is laminar or turbulent[133].

In this work, the particles size and the interaction between shear flow and particles under various conditions were studied. The results can be used to develop an in-situ particle size monitoring equipment to examine the particle size in real-time to determine if the aggregation has taken place or not. Controlling the flow rate can adjust the shear rate, and hence the particle size and concentration. This could benefit the separation and recycling of photocatalyst in the water.

8.3.3 Flow Velocity Measurement

Dealing with fluid flow often needs to measure flow velocity in environmental engineering. For example, in primary wastewater treatment which aims to reduce the total suspended solids, the reactors are designed in a particular size and shape. When the wastewater flows

through each reactor, the flow velocity needs to be controlled with a specific value; then the suspended solid can settle down at the bottom of the reactor. Also, the flow rate of fluid with contaminants which is discharged to the nature water body needs to be controlled in a particular range.

DWS has the potential to provide the on-line velocity measurement. As shown in Chapter 7, the autocorrelation functions of the scattered light intensity varies for different mean flow velocity. This makes DWS possible to be a new method for determining the flow velocity. It is also possible to examine the shear rate or shear strain, which the water flow is subjected to, by measuring the autocorrelation functions.

8.4 Future Work

The current research has successfully achieved the objectives, but further work is still needed. The work listed below will benefit DWS to become a standard method for particle sizing, and a novel method for the on-line monitoring.

- A device was developed in our lab for particle aggregation analysis. It is a spiral channel embedded in the plastic, with water pumped from the bottom to produce various shear rates, as shown in Figure 8.2. The channel is covered by a Perspex glass to produce a hermetic environment. This device is inspired by the research of TiO_2 particle in photocatalystic process. One of my colleagues has completed the research of TiO2 working as photocatalyst to degrade the active dyes under ultraviolet lights. It has been found that the aggregation influences the progress of the degradation. Therefore, this device was developed to study the particles aggregation in photocatalystic process. DWS can be used to investigate particle size in the shear flow in this device to monitor particle's aggregation. Also, the aggregation can be directly observed by an optical microscope through windows opened on the Perspex glass.

Figure 8.2 The spiral channel designed for future experiment.

- The PMT-ADC system was developed in our lab which uses a 16 pixles Photomultiplier to collect the light signal and then transform it to ADC evaluation board (see Figure 8.3). This system has a PMT with high light sensitivity which can replace the CCD camera in future work. Using this device aims to research the DWS experiment under low laser power with insufficient illumination. In addition, the evaluation board supports several digital output formats. By using the ADC analyzer software, the light intensity signal can be collected and processed.

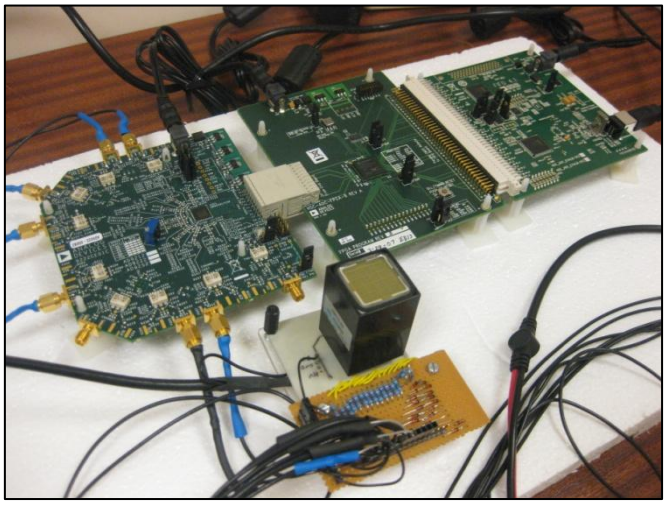

Figure 8.3 The PMT-ADC system for future work.

- The Vanilla system was developed for picture collection by researchers with background of medical images investigation (see Figure 8.4). This system contains a Vanilla COMS

Sensor and a MI3 OptoDAQ board. Also, there is an intensifier with optical fibre inside the vanilla camera. The sensor has an obvious advantage that it has a high resolution than the CCD camera currently used. In the future work, this system will be employed for the purpose of obtaining high quality particle pictures.

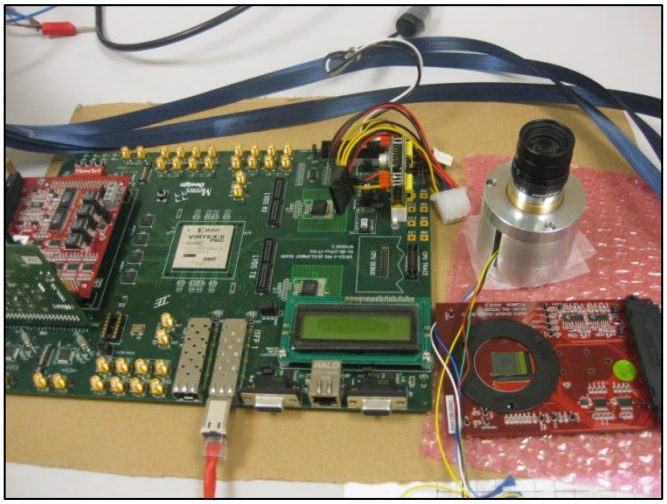

Figure 8.4 The Vanilla system for high quality picture collection.

- In this work, the laser beam was expanded to a diameter approximate 1.5mm. Particle solution in sample cell was believed to be evenly illuminated under such a laser spot. A sufficient sample volume was in the range of radiation. Weitz et al.[87] reported that the size of laser spot had influence on the autocorrelation function. On the other hand, it has been proved that the laser has a thermal blooming effect[74]. Therefore a proper sample volume which is illuminated by laser beam should be considered with care. In the future, some research can be done to investigate the impact of laser spot, such as the beam diameter and the length of the beam in experiment.

- In the flow effect experiment in Chapter 7, the flow velocity varied from 4.63×10^{-7}m/s for 6x6mm^2 flow channel to 0.167m/s for 1x1mm^2 flow channel. The maximum Reynolds Number is 257, and a wide range of shear rate from 0.00023rms to 501rms was studied. Theoretically, to determine the relative dominance of Brownian motion and shear flow, it requires that the flow rate tends to be infinite, the pure flow effect limit then can be reached. The flow range involved in the experiment is far away from the required. Furthermore, the experiment was carried out for the sample cells which have a square cross-section area of 1x1mm^2, 3x3mm^2, 3x6mm^2 and 6x6mm^2. For a specific flow rate,

the flow velocity of large flow cell is 1/9, 1/18 and 1/36 as that for flow cell with the smallest cross-section, and the shear rate is 1/27, 1/54 and 1/216 respectively. Because in environmental engineering, practically the water often flows in open channel or pipe with large diameter. Comparing to that, the channels in this work look like capillary tubes, so the case study is not universe. In open channels or pipes, the flow range and shear rate are enormously different from each other, and they are higher than that in this experiment. Therefore, the future work will investigate the interaction between flow and Brownian motion particles under high velocities and high shear rates in channels or pipes with a large diameter.

Appendix A

The Code of C++ Programme for Autocorrelation Function

```
#include <stdio.h>
#include <math.h>
#include <string.h>
#include <stdlib.h>
const Numi=128;
const Numj=32;
const nin=0;
const min=0;

void main()
{
   long int n, m, i, j, k, frame, N;
        double p, q, r;
        long int refer[128][32], I[128][32];
        double g2[10][1002], sqrg1[10][1002],sum[1002];
   unsigned char strength[128][32];
        char  name[100], strfilename[100];

        const char *path="*** \\";
        const char *path1="1\\";

                                //printf ("input the path where images are placed:");
                                //scanf ("%s", path);
        frame=1000;//printf ("input the number of frames needed for each function:");
                        //scanf ("%d", &frame);
        N=1000;                 //printf ("input the number of frames between two
successive functions:");
                                //scanf ("%d", &N);

        FILE *fname, *fmid;

   for( i = 0; i <frame; i++)
        {
                sum[i]=0;
        }


        for (j=3; j<=10000-frame; j+=N)
        {
                k=j/N;
           for( i = 0; i <frame; i++)
           {
                sprintf(name,"%s***%06d.bmp",path,i+j-1);
                     if (( fname = fopen(name,"rb")) == NULL)
```

```
        {
                printf("can't open this file\n");
                exit(0);
        }

        fseek(fname, 1078L, 0);

              for(n=0;n<128;n++)
              {
                        for(m=0;m<32;m++)
                        {
                                fread(&strength[n][m], 1, 1, fname);

                                if (i==0)
                                {
                                        refer[n][m]= strength[n][m];
                           }
                                I[n][m]= (strength[n][m]);

                        }
              }

        for ( n = nin, p=0, q=0, r=0; n <Numi; n++)
        {
                        for(m=min;m<Numj;m++)
                        {

                                p+= refer[n][m]*I[n][m];
                                q+= refer[n][m];
                                r+= I[n][m];
                        }
        }

                g2[k][i]= p/r/q*(Numi-nin)*(Numj-min);
sqrg1[k][i]=(g2[k][i]-1)/(g2[k][0]-1);

sum[i]=sqrg1[k][i]+sum[i];

      sprintf(strfilename,"%scor-func%03d.txt",path1,(j-1)/N+1);

      if((fmid=fopen(strfilename,"a"))==NULL)
      {
              printf("can't open this file\n");
              exit(0);
      }

      fprintf (fmid, "%4.5f\t%f\t%f\n", 0.00001*i,sqrg1[k][i],g2[k][i]);
                fclose(fmid);

        fclose(fname);
```

```
                    // printf("file %s read ok\n",name);

            }

                printf ("the %d g2 done\n",j);
        }
                for(i = 0; i <frame; i++)
                {
                        sprintf(strfilename,"%scor-func%03d.txt",path1,11);

              if((fmid=fopen(strfilename,"a"))==NULL)
              {
                      printf("can't open this file\n");
                      exit(0);
              }

              fprintf (fmid, "%4.5f\t%f\n", 0.00001*i,sum[i]/9);
                        fclose(fmid);
                }
   printf ("All done!\n");

}
```

where *** denotes the scattered light image file.

References

1. Gokhberg, L., Fursov, K., and Karasev, O., *Nanotechnology development and regulatory framework: The case of Russia.* Technovation, 2012. **32**(3-4): p. 161-162.
2. Nixon, J.R., *Microencapsulation,* 1976, New York: M. Dekker.
3. Deasy, P.B., *Microencapsulation and Related Drug Processes,* 1984, New York: M. Dekker.
4. Kreuter, J., *Nanoparticles,* in *Encyclopedia of Pharmaceutical Technology,* S. J. and B. J.C., Editors. 1994, M. Dekker: New York. p. 165-190.
5. Granqvist, C.G., Buhrman, R.A., Wyns, J., and Sievers, A.J., *Far-infrared Absorption in Ultrafine AL Particles.* Physical Review Letters, 1976. **37**(10): p. 625-629.
6. Hayashi, C., Uyeda, R., and Tasaki, A., *Ultra-fine particles: exploratory science and technology* 1997.
7. Sattler, K.D., *Nanoparticles and Quantum Dots,* 2010: Taylor & Francis.
8. Buzea, C., Pacheco I., and Robbie K., *Nanomaterials and nanoparticles: Sources and toxicity.* Biointerphases, 2007. **2**(4): p. MR17-MR71.
9. Gubin, S.P., *Introduction,* in *Magnetic Nanoparticles*2009, Wiley-VCH Verlag GmbH & Co. KGaA. p. 1-23.
10. Mahmoodi, N.M., Arami, M., Limaee, N.Y., Gharanjig, K., and Nourmohammadian, F., *Nanophotocatalysis using immobilized titanium dioxide nanoparticle: Degradation and mineralization of water containing organic pollutant: Case study of Butachlor*. Materials Research Bulletin, 2007. **42**(5): p. 797-806.
11. Mitchnick, M.A., Fairhurst, D., and Pinnell, S.R., *Microfine zinc oxide (Z-Cote) as a photostable UVA/UVB sunblock agent.* Journal of the American Academy of Dermatology, 1999. **40**(1): p. 85-90.
12. Siegel, R.W., Chang, S.K., Ash, B.j., Stone, J., Ajayan, P.M., Doremus, R.W., and Schadler, L.S., *Mechanical behavior of polymer and ceramic matrix nanocomposites.* Scripta Materialia, 2001. **44**(8-9): p. 2061-2064.
13. Zhu, W., Bartos, P., and Porro, A., *Application of nanotechnology in construction.* Materials and Structures, 2004. **37**(9): p. 649-658.
14. El Naschie, M.S., *Nanotechnology for the developing world.* Chaos, Solitons & Fractals, 2006. **30**(4): p. 769-773.

15. Liming, D., *Carbon Nanotechnology: Recent Developments in Chemistry, Physics, Materials science and device applications*2006, Netherland: Elsevier. 727.
16. de Azeredo, H.M.C., *Nanocomposites for food packaging applications.* Food Research International, 2009. **42**(9): p. 1240-1253.
17. Sricharussin, Threepopnatkul, W., P., and Neamjan, N., *Effect of Various Shapes of Zinc Oxide Nanoparticles on Cotton Fabric for UV-blocking and Anti-bacterial Properties.* Fibers and Polymers, 2011. **12**(8): p. 1037-1041.
18. Tarimala, S., Kothari, N., Abidi, N., Hequet, E., Fralick, J., and Dai, L.L., *New approach to antibacterial treatment of cotton fabric with silver nanoparticle-doped silica using sol-gel process.* Journal of Applied Polymer Science, 2006. **101**(5): p. 2938-2943.
19. Ganta, S., Devalapally, H., Shahiwala, A., and Amijil, M., *A review of stimuli-responsive nanocarriers for drug and gene delivery.* Journal of Controlled Release, 2008. **126**(3): p. 187-204.
20. Dionysiou, D.D., Suidan, M.T., Bekou, E., Baudin, I., and Laine, J., *Effect of ionic strength and hydrogen peroxide on the photocatalytic degradation of 4-chlorobenzoic acid in water.* Applied Catalysis B: Environmental, 2000. **26**(3): p. 153-171.
21. Lee, S., Choo, K., Lee, C., Lee, H., Hyeon, T., Choi, W., and Kwon, H, *Use of ultrafiltration membranes for the separation of TiO2 photocatalysts in drinking water treatment.* Ind. Eng. Chem. Res., 2001. **40**(7): p. 1712-1719.
22. Fujishima, A. and Honda, K., *Electrochemical Photolysis of Water at a Semiconductor Electrode*. Nature, 1972. **238**(5358): p. 37-+.
23. Phanikrishna Sharma, M.V., Sadanandam, G., Ratnamana, A., Durga, Kumari, V., and Subrahmanyam, M., *An efficient and novel porous nanosilica supported TiO2 photocatalyst for pesticide degradation using solar light.* Journal of hazardous materials, 2009. **171**(1-3): p. 626-33.
24. Saien, J. and Shahrezaei F., *Organic Pollutants Removal from Petroleum Refinery Wastewater with Nanotitania Photocatalyst and UV Light Emission.* International Journal of Photoenergy, 2012.
25. Shen, W., Zhao, W., He, F., and Fang Y., *TiO2-Based Photocatalysis and Its Applications for Waste Water Treatment.* Progress in Chemistry, 1998. **10**(4): p. 349-361.
26. Salim, N.T., Yamada, M., Nakano, H., Shima, K., Isago, H., and Fukumoto, M., *The effect of post-treatments on the powder morphology of titanium dioxide (TiO2)*

powders synthesized for cold spray. Surface & Coatings Technology, 2011. **206**(2-3): p. 366-371.

27. Qian, C. and McClements, D.J., *Formation of nanoemulsions stabilized by model food-grade emulsifiers using high-pressure homogenization: Factors affecting particle size.* Food Hydrocolloids, 2011. **25**(5): p. 1000-1008.
28. De Beer, T.R.M., Baeyens, W.G., Vander, Heyden, Y., Remon, J.P., Vervaet, C., and Verpoort, F., *Influence of particle size on the quantitative determination of salicylic acid in a pharmaceutical ointment using FT-Raman spectroscopy.* European Journal of Pharmaceutical Sciences, 2007. **30**(3-4): p. 229-235.
29. Vrana, A. and Andrysek, T., *The effect of particle size on bioavailability in cyclosporine preparations based on submicron dispersions.* Biomedical Papers (Olomouc), 2001. **145**(2): p. 9-15.
30. Elizalde, O., Leal, G.P., and Leiza, J.R., *Particle size distribution measurements of polymeric dispersions: A comparative study.* Particle & Particle Systems Characterization, 2000. **17**(5-6): p. 236-243.
31. Tolpekin, V.A., Duits, M.H.G., van den Ende, D., and Mellema, J., *Aggregation and breakup of colloidal particle aggregates in shear flow, studied with video microscopy.* Langmuir, 2004. **20**(7): p. 2614-2627.
32. Foster, I.D.L., Millington, R., and Grew, R.G., *The Impact of Particle-size Controls on Stream Turbidity Measurement - Some Implications for Suspended Sediment Yield Estimation.* Erosion and Sediment Transport Monitoring Programmes in River Basins, ed. Bogen, J., Walling, D.E., and Day, T.J.. Vol. 210. 1992, Wallingford: Int Assoc Hydrological Sciences. 51-62.
33. Levine, A.D., Tchobanoglous G., and Asano, T., *Characterization of the Size Distribution of Contaminants in Wastewater: Treatment and Reuse Implications.* Journal (Water Pollution Control Federation), 1985. **57**(7): p. 805-816.
34. Zhang, W.X., *Nanoscale Iron Particles for Environmental Remediation: An Overview.* Journal of Nanoparticle Research, 2003. **5**(3): p. 323-332.
35. Lee, B.J., Fettweis, M., Toorman, E., and Molz, F.J., *Multimodality of a particle size distribution of cohesive suspended particulate matters in a coastal zone.* Journal of Geophysical Research-Oceans, 2012. **117**.
36. Tratnyek, P.G., Sarathy, V., Kimyoon, J., Change, Y., and Bae, B., *Effect of Particle Size on the Kinetics of Degradation of Contaminants*, in *International Environmental Nanotechnology Conference -- Applications and Implications*2009: Chicago. p. 67-72.

37. Andronic, L., Andrasi, D., Enesa, A., Visa, M., and Duta, A., *The influence of titanium dioxide phase composition on dyes photocatalysis.* Journal of Sol-Gel Science and Technology, 2011. **58**(1): p. 201-208.
38. Boyd, R.D., Pichaimuthu S.K., and Cuenat A., *New approach to inter-technique comparisons for nanoparticle size measurements; using atomic force microscopy, nanoparticle tracking analysis and dynamic light scattering.* Colloids and Surfaces a-Physicochemical and Engineering Aspects, 2011. **387**(1-3): p. 35-42.
39. Miller, C.M., Sudol. E.D., Silebi, C.A., and Elaasser, M.S., *Capollary Hydrodynamic Fractionation (CHDF) as a Tool for Monitring the Evolution of the Particle-size Distribution During Miniemulsion Polymerization.* Journal of Colloid and Interface Science, 1995. **172**(1): p. 249-256.
40. Scheffold, F., *Particle sizing with diffusing wave, spectroscopy.* Journal of Dispersion Science and Technology, 2002. **23**(5): p. 591-599.
41. Skipetrov, S.E. and Meglinski, I.V., *Diffusing-wave spectroscopy in randomly inhomogeneous media with spatially localized scatterer flows.* Journal of Experimental and Theoretical Physics, 1998. **86**(4): p. 661-665.
42. Chiu, D.T. and Zare, R.N., *Biased diffusion, optical trapping, and manipulation of single molecules in solution.* Journal of the American Chemical Society, 1996. **118**(27): p. 6512-6513.
43. Kuyper, C.L., Fujimoto, B.S., Zhao, Y., Schiro. P.G., and Chiu, D.t., *Accurate sizing of nanoparticles using confocal correlation spectroscopy.* Journal of Physical Chemistry B, 2006. **110**(48): p. 24433-24441.
44. Navabpour, P., Rega.C., Lloyd, C.J., Attwood, D., Lovell, P.A., Geraghty, P. and Clarke, D., *Influence of concentration on the particle size analysis of polymer latexes using diffusing-wave spectroscopy.* Colloid and Polymer Science, 2005. **283**(9): p. 1025-1032.
45. Wu, X.L., Pine, D.J., Chaikin, P.M., Huang, J.S. and Weitz, D.A., *Diffusing-wave Spectroscopy in a Shear-flow*. Journal of the Optical Society of America B-Optical Physics, 1990. **7**(1): p. 15-20.
46. Skipetrov, S.E., Chesnokov, S.S., Meglinski, I.V. and Tuchin, V.V., *Diffusing wave spectroscopy of flows,* in *Laser Spectroscopy and Optical Diagnostics: Novel Trends and Applications in Laser Chemistry, Biophysics, and Biomedicine - Icono'98*, Chikishev, A.Y., Zadkov, V.N., and Zheltikov, A.M., Editors. 1999, Spie-Int Soc Optical Engineering: Bellingham. p. 336-344.

47. Jian, G., Fu, Q.Y., and Zhou, D.X., *Particles size effects of single domain CoFe2O4 on suspensions stability.* Journal of Magnetism and Magnetic Materials, 2012. **324**(5): p. 671-676.
48. Suttiponparnit, K., Jiang, J.K., Sahu, M., Suvachittanont, S., Charinpanitkul. T. and Biswas, P., *Role of Surface Area, Primary Particle Size, and Crystal Phase on Titanium Dioxide Nanoparticle Dispersion Properties.* Nanoscale Research Letters, 2011. **6**.
49. Zhang, Y. and Johnson, K.C., *Effect of drug particle size on content uniformity of low-dose solid dosage forms.* Pharmaceutical Research (New York), 1996. **13**(9 SUPPL.): p. S349.
50. Cha, J.U., Cha, J.H., Hong, J.K., Lee, S.W., Ko, W.H. and Beak, H.H., *Effect of Particle Size of HPMC on Dissolution Rate of Venlafaxine HCl and Carbamazepine Sustained Release Tablet.* Polymer-Korea, 2012. **36**(3): p. 332-337.
51. Johnson, K.C., *Dissolution and absorption modeling: Model expansion to simulate the effects of precipitation, water absorption, longitudinally changing intestinal permeability, and controlled release on drug absorption.* Drug Development and Industrial Pharmacy, 2003. **29**(8): p. 833-842.
52. Kim, B.S. and Chang, S.Y., *Microstructure and Magnetic Properties of Nano-Sized Ba-Al Ferrite Particles by High Energy Ball Milling.* Journal of Nanoscience and Nanotechnology, 2012. **12**(2): p. 1301-1304.
53. Svoboda, R. and Malek, J., *Particle size influence on crystallization behavior of Ge2Sb2Se5 glass.* Journal of Non-Crystalline Solids, 2012. **358**(2): p. 276-284.
54. Jillavenkatesa, A. and Kelly, J.F., *Nanopowder Characterization: Challenges and Future Directions.* Journal of Nanoparticle Research, 2002. **4**(5): p. 463-468.
55. Nolte, H., Schilde, C., and Kwade, A., *Determination of particle size distributions and the degree of dispersion in nanocomposites.* Composites Science and Technology, 2012. **72**(9): p. 948-958.
56. Finsy, R., *Particle sizing by quasi-elastic light scattering.* Advances in Colloid and Interface Science, 1994. **52**(0): p. 79-143.
57. Naito, M., Hayakawa, O., Nakahira, K., Mori, H. and Tsubaki, J., *Effect of particle shape on the particle size distribution measured with commercial equipment.* Powder Technology, 1998. **100**(1): p. 52-60.

58. Houghton, M.E. and Amidon, G.E., *Microscopic Characterization of Particle-size and Shape - An Inexpensive and Versatile Method*. Pharmaceutical Research, 1992. **9**(7): p. 856-859.
59. Wikipedia. *Particle Size*. 2012 [cited 2012 31/08/2012]; Available from: http://en.wikipedia.org/wiki/Particle_size.
60. Brewer, E. and Ramsland, A., *Particle-size Determination by Automated Microscopic Imaging Analysis with Comparison to Laser Diffraction.* Journal of Pharmaceutical Sciences, 1995. **84**(4): p. 499-501.
61. Walton, W.H., *Ferets Statistical Diameter as a measure of Particle Size*. Nature, 1948. **162**(4113): p. 329-330.
62. Hackley, V.A. and Clogston, J.D., *Measuring the hydrodynamic size of nanoparticles in aqueous media using batch-mode dynamic light scattering.* Methods in molecular biology, 2011. **697**: p. 35-52.
63. Vigneau, E., Loisel, C., Devaux, M.F. and Cantoni, P., *Number of particles for the determination of size distribution from microscopic images.* Powder Technology, 2000. **107**(3): p. 243-250.
64. Almeida-Prieto, Blanco-Mendez, S., J., and Otero-Espinar, F.J., *Microscopic image analysis techniques for the morphological characterization of pharmaceutical particles: Influence of the software, and the factor algorithms used in the shape factor estimation.* European Journal of Pharmaceutics and Biopharmaceutics, 2007. **67**(3): p. 766-776.
65. Davidson, J.A. and Butler, R.S., *Sizing Particles by Optical Microscopy Through Criteria Developed by The Analysis of Image Profiles*. Particle & Particle Systems Characterization, 1992. **9**(4): p. 213-222.
66. Ronnest, N.P., Stocks, S.M., Lantz, A.E. and Gernaey, K.V., *Comparison of laser diffraction and image analysis for measurement of Streptomyces coelicolor cell clumps and pellets.* Biotechnology Letters, 2012. **34**(8): p. 1465-1473.
67. Wanogho, S., Gettinby, G., and Caddy, B., Particle-size Distribution Analysis of Soils Using Laser Diffraction. Forensic Science International, 1987. **33**(2): p. 117-128.
68. Wang, N.N., Zhang, H.J. and Yu, X.H., *A Versatile Fraunhofer-diffraction and Mie Scattering Based Laser Particle Sizer*. 2 World Congress : Particle Technology, Pts 1-5, 1990: p. A452-A458.

69. Adrian, R.J., *Scattering Particle Characteristics and Their Effect on Pulsed Laser Measurements of Fluid-flow - Speckle Velocimetry VS Particle Image Velocimetry. Applied Optics*, 1984. **23**(11): p. 1690-1691.
70. Chen, R.C. and Fan L.S., *Particle Image Velocimetry for Characterizing the Flow Structure in 3-Dimensional Gas-liquid-solid Fluidzed-beds*. Chemical Engineering Science, 1992. **47**(13-14): p. 3615-3622.
71. Cheng, C.Y., Atkinson, J.F., VanBenschoten, J.E., Bursik, M.I. and DePinto, J.V., *Image-based system for particle counting and sizing.* Journal of Environmental Engineering-Asce, 2000. **126**(3): p. 258-266.
72. Brady, M.R., Raben, S.G., and Vlachos, P.P., *Methods for Digital Particle Image Sizing (DPIS): Comparisons and improvements.* Flow Measurement and Instrumentation, 2009. **20**(6): p. 207-219.
73. Fytas, G. and Patkowski, A., *Dynamic light scattering from polymers in solution and in bulk*, in *Dynamic Light Scattering: The Method and Some application*, W. Brown, Editor 1993, Oxford University Press: New York. p. 440-470.
74. Lin, X.M., Wang, G.M., Sorensen, C.M. and Klabunde, K.J., et al., *Thermal blooming effect on particle sizing with photon correlation spectroscopy.* Applied Optics, 1999. **38**(9): p. 1884-1886.
75. Hallett, F.R., *Particle-size Analysis by Dynamic Light-scattering*. Food Research International, 1994. **27**(2): p. 195-198.
76. Gugliotta, L.M., Vega, J.R., and Meira, G.R., *Latex Particle Size Distribution by Dynamic Light Scattering: Computer Evaluation of Two Alternative Calculation Paths.* Journal of Colloid and Interface Science, 2000. **228**(1): p. 14-17.
77. Koppel, D.E., *Analysis of Macromolecular Polydispersity in Intensity Correlation Spectroscopy - Methid of Cumulants*. Journal of Chemical Physics, 1972. **57**(11): p. 4814-&.
78. Zakharov, P., Bhat. S., Schurtenberger, P. and Scheffold, F., *Multiple-scattering suppression in dynamic light scattering based on a digital camera detection scheme.* Applied Optics, 2006. **45**(8): p. 1756-1764.
79. Phillies, G.D.J., *Experimental Demonstration of Multiple-scattering Suppression in Quasielastic-light-scattering Spectroscopy by Homodyne Coincidence Techniques*. Physical Review A, 1981. **24**(4): p. 1939-1943.
80. Pecora, R., *Dynamic Light Scattering: Applications of Photon Correlation Spectroscopy*1985: Springer. 436.

81. Overbeck, E., Sinn, C., Palberg. T. and Schatzel, K., *Probing dynamics of dense suspensions: Three-dimensional cross-correlation technique.* Colloids and Surfaces a-Physicochemical and Engineering Aspects, 1997. **122**(1-3): p. 83-87.
82. Drewel, M., Ahrens, J., and Podschus, U., *Decorrelation of Multiple-scattering for An Arbitrary Scattering Angle*. Journal of the Optical Society of America a-Optics Image Science and Vision, 1990. **7**(2): p. 206-210.
83. Schatzel, K., Drewel, M., and Ahrens, J., *Suppression of Multiple-scattering in Photon-correlation Spectroscopy.* Journal of Physics-Condensed Matter, 1990. **2**: p. SA393-SA398.
84. Pusey, P.N., *Suppression of multiple scattering by photon cross-correlation techniques.* Current Opinion in Colloid & Interface Science, 1999. **4**(3): p. 177-185.
85. Maret, G. and Wolf, P.E., *Multiple Light-scattering From Disordered Media - The Effect of Brownian-motion of Scatters*. Zeitschrift Fur Physik B-Condensed Matter, 1987. **65**(4): p. 409-413.
86. Weitz, D.A., Pine, D.J., Pusey, P.N. and Tough, R.J.A., *Nondiffusive Brownian-motion Studied by Diffusing-wave Spectroscopy.* Physical Review Letters, 1989. **63**(16): p. 1747-1750.
87. Weitz, D.A. and Pine, D.J., *Diffusing-wave spectroscopy*, in *Dynamic Light Scattering: The Method and Some Application*, W. Brown, Editor 1993, Oxford University Press: New York. p. 652-720.
88. Pine, D.J., Weitz, D.A., Chaikin. P.M. and Herbolzheimer, E., *Diffusing-wave Spectroscopy*. Physical Review Letters, 1988. **60**(12): p. 1134-1137.
89. Stephen, M.J., *Temporal fluctuations in wave propagation in random media.* Physical Review B, 1988. **37**(1): p. 1-5.
90. Pine, D.J., Weitz, D.A., Zhu, J.X. and Herbolzheimer, E., *Diffusing-wave Spectroscopy - Dynamic Light-scattering in The Multiple-scattering Limit.* Journal De Physique, 1990. **51**(18): p. 2101-2127.
91. Wiederseiner, S., Andreini, N., Epely-Chauvin, G. and Ancey, C., *Refractive-index and density matching in concentrated particle suspensions: a review.* Experiments in Fluids, 2011. **50**(5): p. 1183-1206.
92. Keuren, E.R.V., Wiese, H., and Horn, D., *Diffusing-wave spectroscopy in concentrated latex dispersions: An investigation using single-mode fibers.* Colloids and Surfaces A: Physicochemical and Engineering Aspects, 1993. **77**(1): p. 29-37.

93. Rojas-Ochoa, L.F., Romer, S., Scheffold, F. and Schurtenberger, P., *Diffusing wave spectroscopy and small-angle neutron scattering from concentrated colloidal suspensions.* Physical Review E, 2002. **65**(5).

94. Nishimura, G., Katayama, K., Kinjo, M. and Tamura, M, *Diffusing-wave absorption spectroscopy in homogeneous turbid media.* Optics Communications, 1996. **128**(1-3): p. 99-107.

95. Kaplan, P.D., Kao, M.H., Yodh, A.G. and Pine, D.J., *Geometric Constraints for The Design of Diffusing-wave Spectroscopy Experiments*. Applied Optics, 1993. **32**(21): p. 3828-3836.

96. Hamamatsu. *Photomultiplier (PMT) Modules H8711* 2010 [cited 2012 04/09/2012]; Available from: http://sales.hamamatsu.com/en/products/electron-tube-division/detectors/photomultiplier-modules/part-h8711.php#.

97. Cipelletti, L. and Weitz, D.A., *Ultralow-angle dynamic light scattering with a charge coupled device camera based multispeckle, multitau correlator.* Review of Scientific Instruments, 1999. **70**(8): p. 3214-3221.

98. Wong, A.P.Y. and Wiltzius, P., *Dynamic Light-scattering With A CCD Camera.* Review of Scientific Instruments, 1993. **64**(9): p. 2547-2549.

99. Photron. *Photron camera product* 2012 [cited 2012 04/09/2012]; Available from: http://www.photron.com/index.php?cmd=products&type=legacy.

100. Kirsch, S., Frenz, V., Schartl, W., Bartsch, E. and Sillescu, H, *Multispeckle autocorrelation spectroscopy and its application to the investigation of ultraslow dynamical processes.* Journal of Chemical Physics, 1996. **104**(4): p. 1758-1761.

101. Harden, J.L. and Viasnoff, V., *Recent advances in DWS-based micro-rheology.* Current Opinion in Colloid & Interface Science, 2001. **6**(5-6): p. 438-445.

102. Yang, H., Zheng, G., and Li, M., *A Discussion of Noise in Dynamic Light Scattering for Particle Sizing.* Particle Sizing. Part. Part. Syst. Charact., 2008. **25**: p. 406-413.

103. Viasnoff, V., Lequeux, F., and Pine, D.J., *Multispeckle diffusing-wave spectroscopy: A tool to study slow relaxation and time-dependent dynamics.* Review of Scientific Instruments, 2002. **73**(6): p. 2336-2344.

104. Xu, J., Dong, X., Zhang, L.F., Jiang, Y.G. and Zhou, L.W., *Diffusing wave spectroscopy method based on high-speed charge coupled device for nonergodic systems of electrorheological fluids.* Review of Scientific Instruments, 2002. **73**(10): p. 3575-3578.

105. Gisler, T., Ruger, H., Egelhaaf, S.U., Tschumi., J., Schurtenberger, P. and Ricka, J., *Mode-selective Dynamic Light-scattering - Theory Versus Experimental Realization.* Applied Optics, 1995. **34**(18): p. 3546-3553.
106. Pine, D.J., Weitz, D.A., Maret, G., Wolf., P.E., Herbolzheimer, E. and Chaikin, P.M., *Dynamical correlations of multiply scattered light*, in *Scattering and Localization of Classical Waves in Random Media*, P. Sheng, Editor 1990, World Scientific: Singapore.
107. Batchelor, G.K., *Brownian Diffusion of Particles with Hydrodynamic Interaction.* Journal of Fluid Mechanics, 1976. **74**(MAR9): p. 1-29.
108. Gopal, A.D. and Durian, D.J., *Shear-induced "melting" of an aqueous foam.* Journal of Colloid and Interface Science, 1999. **213**(1): p. 169-178.
109. Podczeck, F., Rahman, S.R., and Newton, J.M., *Evaluation of a standardised procedure to assess the shape of pellets using image analysis.* International Journal of Pharmaceutics, 1999. **192**(2): p. 123-138.
110. Almeida-Prieto, S., Blanco-Mendez, J., and Otero-Espinar, F.J., *Microscopic image analysis techniques for the morphological characterization of pharmaceutical particles: Influence of process variables.* Journal of Pharmaceutical Sciences, 2006. **95**(2): p. 348-357.
111. Skipetrov, S.E., *Effect of absorption on temporal correlation of light scattered from a turbid medium.* Optics Communications, 1998. **152**(4-6): p. 229-232.
112. Mackintosh, F.C., Zhu, J.X., and Pine, D.J. and Weitz, D.A., *Polarization Memory of Multiply Scattered-light*. Physical Review B, 1989. **40**(13): p. 9342-9345.
113. Kaplan, P.D., Yodh, A.G., and Townsend, D.F., *Noninvasive Study of Gel Formation In Polymer-Stabilized Dense Colloids Using Multiply Scattered-light.* Journal of Colloid and Interface Science, 1993. **155**(2): p. 319-324.
114. Horne, D.S. and Davidson, C.M., *Application of Diffusing-wave Spectroscopy to Particle Sizing in Concentrated Dispersions*. Colloids and Surfaces a-Physicochemical and Engineering Aspects, 1993. **77**(1): p. 1-8.
115. Harada, Y. and Asakura, T., *Effects of The Laser-Radiation Pressure In Photon-correlation Spectroscopy*. Optics Communications, 1994. **107**(1-2): p. 161-169.
116. Chu, B., *Laser light scattering: Basic principles and practice*. 2nd Edition ed1991, Boston: Academic Press

117. Giraud, I., Dantras, E., Brun, A., Dihang, H., Brunel, L., Bernes, A., Menunier, G. and Lacabanne, C., *Film formation analysis by diffusive wave spectroscopy.* Progress in Organic Coatings, 2009. **64**(4): p. 515-519.

118. Liu, J., Verespej. E., Corredig, M. and Alexander, M, *Investigation of interactions between two different polysaccharides with sodium caseinate-stabilized emulsions using complementary spectroscopic techniques: Diffusing wave and ultrasonic spectroscopy.* Food Hydrocolloids, 2008. **22**(1): p. 47-55.

119. Rega, C., Llyod, C.J., Attwood, D., Clarke, D. and Geraghty, P., *Temporal autocorrelation function for a diffusing-wave spectroscopy experiment with a point source and backscattering detection.* Applied Optics, 2001. **40**(24): p. 4204-4209.

120. Kondrat'ev, A.V., *Observation of multiple scattering of laser radiation from a light-induced jet of microparticles in suspension.* Quantum Electronics, 2004. **34**(6): p. 545-546.

121. Oelschlaeger, C., Schopferer. A., Scheffold, F. and Willenbacher, N., *Linear-to-Branched Micelles Transition: A Rheometry and Diffusing Wave Spectroscopy (DWS) Study.* Langmuir, 2009. **25**(2): p. 716-723.

122. Lloyd, C.J., Perkins, E., Atkinson, T. and Carr, R.J.G., *Diffusing Wave Spectroscopy,* in *Proceedings of Quantification and Localization Using Diffuse Photons in a Highly Scattering Medium*, Chance, B., Delpy, D.T., Ferrari, M., VanGemert, M.J., Muller, G.J., Tuchin, V.V. and Katzir, A., Editors. 1994, Spie-Int Soc Optical Engineering: Bellingham. p. 279-287.

123. Pusey, P.N. and R.J.A. Tough, *Particle Interactions*, in *Dynamic Light Scattering:Applications of Photon Correlation Spectroscopy*, R. Pecora, Editor 1985, Plenum: New York. p. 85-171.

124. Wiese, H. and Horn, D., *Single-mode Fibers in Fiberoptic Quasi-elastic Light-scattering - A Study of the Dynamics of Concentrated Latex Dispersions.* Journal of Chemical Physics, 1991. **94**(10): p. 6429-6443.

125. Qiu, X., Wu, X.L., Xue, J.Z., Pine, D.J., Weitz, D.A. and Chaikin, P.M., *Hydrodynamic Interactions In Concentrated Suspensions.* Physical Review Letters, 1990. **65**(4): p. 516-519.

126. Beenakker, C.W.J. and Mazur, P., *Self-diffusion of Spheres In A Concentrated Suspension.* Physica A, 1983. **120**(3): p. 388-410.

127. Beenakker, C.W.J. and Mazur, P., *Diffusion of Spheres In A concentrated Suspensions. 2*. Physica A, 1984. **126**(3): p. 349-370.

128. Snook, I., Vanmegen, W., and Tough, R.J.A., *Diffusion In Concentrated Hard-sphere Dispersions - Effective 2 Particle Mobility Tensors.* Journal of Chemical Physics, 1983. **78**(9): p. 5825-5836.
129. Xue, J.Z., Wu, X.L., Pine, D.J. and Chaikin, P.M., *Hydrodynamic Interactions in Hard-sphere Suspensions.* Physical Review A, 1992. **45**(2): p. 989-993.
130. Felderhof, B.U., *Diffusion of Interacting Brownian Particles*. Journal of Physics a-Mathematical and General, 1978. **11**(5): p. 929-937.
131. Beenakker, C.W.J. and Mazur, P., *Diffusion of Spheres in Suspension - 3-Body Hydrodynamic Interation Effects.* Physics Letters A, 1982. **91**(6): p. 290-291.
132. Clercx, H.J.H. and Schram, P., *Brownian Particles in Shear-flow and Harmonic Potentials - A Study of Long-time Tails.* Physical Review A, 1992. **46**(4): p. 1942-1950.
133. Serra, T., J. Colomer, and Casamitjana, X., *Aggregation and breakup of particles in a shear flow.* Journal of Colloid and Interface Science, 1997. **187**(2): p. 466-473.
134. Xu, S.H., Sun, Z.W., Li.X. and Jin, T.W., *Coupling effect of Brownian motion and laminar shear flow on colloid coagulation: a Brownian dynamics simulation study.* Chinese Physics B, 2012. **21**(5).
135. Hinch, E.J., *Apllication of Langevin Equation to Fluid Suspensions.* Journal of Fluid Mechanics, 1975. **72**(DEC9): p. 499-511.
136. Jeffery, G.B., *The motion of ellipsoidal particles in a viscous fluid.* Proceedings of the Royal Society of London Series a-Containing Papers of a Mathematical and Physical Character, 1922. **102**(715): p. 161-179.
137. Tehrani, M.A., *An experimental study of particle migration in pipe flow of viscoelastic fluids.* Journal of Rheology, 1996. **40**(6): p. 1057-1077.
138. Won, D. and Kim, C., *Alignment and aggregation of spherical particles in viscoelastic fluid under shear flow.* Journal of Non-Newtonian Fluid Mechanics, 2004. **117**(2-3): p. 141-146.
139. Serra, T. and Casamitjana, X., *Effect of the shear and volume fraction on the aggregation and breakup at particles.* Aiche Journal, 1998. **44**(8): p. 1724-1730.
140. Ruis, H.G.M., Venema, P., and van der Linden, E., *Diffusing wave spectroscopy used to study the influence of shear on aggregation.* Langmuir, 2008. **24**(14): p. 7117-7123.
141. Bicout, D. and Maret, G., Mutiple Light-scattering in Taylor-couette Flow. Physica A, 1994. **210**(1-2): p. 87-112.

142. Landau, L.D. and Lifshitz, E.M., *Fluid Mechanics*. Vol. 6. 1985, Oxford: Pergamon. 532.

143. Akkermans, E., Wolf, P.E., Maynard, R. and Maret, G., *Theoretical Study of THE Coherent Backscattering of Light by Disordered Media.* Journal De Physique, 1988. **49**(1): p. 77-98.

144. Cox, A.J., DeWeerd, A.J., and Linden, J., *An experiment to measure Mie and Rayleigh total scattering cross sections.* American Journal of Physics, 2002. **70**(6): p. 620-625.

145. Bin Omar, A.F. and Bin MatJafri, M.Z., *Turbidimeter Design and Analysis: A Review on Optical Fiber Sensors for the Measurement of Water Turbidity.* Sensors, 2009. **9**(10): p. 8311-8335.

146. Gondal, M.A., Hameed, A., and Suwaiyan, A., *Photo-catalytic conversion of methane into methanol using visible laser.* Applied Catalysis A: General, 2003. **243**(1): p. 165-174.